

Investigation Of Opto-Electronic Phenomena In Nanostructured ZnO With Electric Double Layer Gate

Thesis submitted for the degree of
Doctor of Philosophy (Science)

in

Physics (Experimental)

by

Rishi Ram Ghimire

Department of Physics
University of Calcutta
September 2016

To my Parents.....

Acknowledgments

I am very thankful to have got the opportunity to undertake PhD research that has been challenging, enlightening and worthwhile. It was a prodigious opportunity to meet, collaborate and exchange knowledge with many people.

First of all I would like to express my deep gratitude to my coordinating supervisor professor Arup K. Raychaudhuri who accepted me as a PhD student and for his professional supervision and guidance. He has always given me the great support, encouragement and direction to be a good experimental physicist. I have benefited and inspired from his wide knowledge and logical way of thinking in any type of problems. Without his constant encouragement and support, I would not have been able to complete this thesis.

I would like to express my profound admiration equally to "The World Academy of Science" (TWAS) and S. N. Bose National Centre for Basic Sciences who accepted me as a PhD scholar and offered a scholarship during my PhD tenure.

I am heartily thankful to my collaborators Mr. Shahnewaz Mondal, Dr. Rajib Nath, Dr. Rajesh Kr. Neogy and Mr. Ravindra S. Bisht for sharing experimental skills and scientific discussions. Mr. Bisht and Dr. Nath minutely helped me to complete chapter-4 and 6 of this thesis.

I want to express my gratitude to Dr. Barnali Ghosh (Saha) for allowing me to use the photoconductivity measurement setup. She is kind and her loving character always encouraged me to finish the work. I wish to thank Dr. Kaustav Das, Dr. Pabitra Mondal and Dr. Sudeshna Samanta for their valuable advices. I am also grateful to Dr. Ankita Ghatak, Dr. Rabya Basori and Dr. Jasashree Ray for their assistance and discussions.

My special thanks go to Mr. Samik Roymaulik and Mrs. Subarna Dutta who helped me in experimental as well as other official activities.

In our big research family, there are so many seniors (Manotosh, Putul, Sabyasachi) and juniors (Saili, Bibhuti, Subhamita, Chandan, Avisek) scholars, who helped me according to their abilities and strengths. I heartful acknowledge to them.

I also Acknowledge Prof. Shankar Prasad Shrestha, Prof. Narayan Adhikari, Associate Professor Gopi C. Kaphle (Tribhuvan university, Kathmandu) and Mr. Victor U. J. Nwankwo (Nigeria) for their encouragement, valuable suggestions and good company in several times.

My gratitude will remain incomplete if I do not mention our former deputy registrar Mr. Sunish k. Deb who helped me to handle all the official process including the PhD registration in University of Calcutta. similarly, I offer my sincere wishes and warmest thanks to all the technical staffs (Shakti Nath Das, Surajit Mukherjee, Jay Bandopadhyay, Urmi Chakrabarty and Amit Chanda) of S. N. Bose Centre for their cooperation and efforts for sample preparations and characterizations.

Finally, I reserve my deepest gratitude to my family for their constant love and support.

Rishi Ram Ghimire
S.N. Bose National Centre for Basic Sciences
Kolkata, India
September, 2016

List of Publications

1. **Rishi Ram Ghimire**, Shahnewaz Mondal and A. K. Raychaudhuri *Synergistic ultraviolet photoresponse of a nanostructured ZnO film with gate bias and ultraviolet illumination*, **J. Appl. Phys.** **117**, 105705 (2015).*
2. **Rishi Ram Ghimire**, Rajib Nath, Rajesh K. Neogy and A. K. Raychaudhuri, *A high performance broadband photo-detector based on ZnO nanowire film attached with ligand free Plasmonic Au nanoparticles*, **Submitted in Applied Material and Interface**. *
3. **Rishi Ram Ghimire** and A. K. Raychaudhuri, *High performance low threshold flexible thin film transistor (Flex-TFT) with electric double layer gate insulator and textured nanostructured ZnO film channel*, **to be submitted**. *
4. Ravindra Singh Bisht, **Rishi Ram Ghimire** and A. K. Raychaudhuri *Control of Grain Boundary Depletion Layer and Capacitance in ZnO Thin Film by a Gate with Electric Double Layer Dielectric*, **J. Phy. Chem. C** **119**, 27813-27820 (2015). *
5. Shahnewaz Mondal, **Rishi Ram Ghimire** and A. K. Raychaudhuri, *Mobility enhancement in electric double layer gated n-ZnO ultraviolet photodetector by synergy of gate and illumination: A photo Hall study*, **Appl. Phys. Lett.** **106**, 041102 (2015).
6. Shahnewaz Mondal, **Rishi Ram Ghimire** and A. K. Raychaudhuri, *Enhancing photoresponse by synergy of gate and illumination in electric double layer field effect transistors fabricated on n-ZnO*, **Appl. Phys. Lett.**, **103**, 231105 (2013).

List of Abbreviations

EDL:	Electric Double Layer	FE:	Field Effect
PLD:	Pulsed Laser Deposition	UV:	Ultraviolet
GB:	Grain Boundary	μ_{FE} :	Field Effect mobility
PMMA:	Polymethyl Methacrylate	μ_H :	Hall mobility
FET:	Field Effect Transistor	C_i :	Specific Capacitance
TFT:	Thin Film Transistor	R :	Responsivity
IL:	Ionic Liquid	G :	Current Gain
PEO:	Polyethylene Oxide	w :	Grain Boundary Depletion width
EDLT:	Electric Double Layer Transistor	E_g :	Band Gap
EDL-C:	Electric Double Layer Capacitor	α :	Absorption Coefficient
Flex-TFT:	Flexible Thin Film Transistor	Δn_s :	surface charge density
V_H :	Hall voltage	nm:	nanometer
V :	Applied Bias	I :	Current
V:	Volt	s:	Sec
A:	Amper	ρ :	Resistivity
I_{ph} :	Photocurrent	R:	Sample resistance
Ω :	Ohm	λ_D :	Debye Length
R_s :	sheet Resistance	ϕ_{GB} :	Grain Boundary Potential
T :	Temperature	T:	Tesla
I_g :	Gate Current	V_{ds} :	Source-Drain Voltage
I_d :	Drain Current	V_g :	Gate Voltage

Contents

Table of Contents	vii
List of Figures	xi
List of Tables	xvii
1 Introduction	1
1.1 ZnO nanostructure	2
1.2 Motivation	5
1.3 Basic properties of ZnO	7
1.3.1 Crystal structure	7
1.3.2 Optical properties	8
1.3.3 Electrical properties	12
1.4 Overview of electric double layer (EDL) as gate dielectric	12
1.5 Overview on control mechanisms of defect states in ZnO nanostructures	16
2 Sample preparation, characterization and measurement techniques	25
2.1 Introduction	26
2.2 Preparation of nanostructured ZnO	27
2.2.1 Chemical process	27
2.2.1.1 Sol-gel spin coating	27
2.2.1.2 Hydrothermal method	30
2.2.2 Physical process	32
2.2.2.1 Pulsed laser deposition	32
2.2.2.2 Decoration of Plasmonic Au nanoparticles on ZnO nanowire surface using laser ablation in liquid medium	35
2.3 Characterization	36
2.3.1 Structural characterization	36
2.3.1.1 X-ray diffraction	36
2.3.1.2 Scanning electron microscopy	37
2.3.1.3 Atomic force microscope	38
2.3.1.4 Energy dispersive X-ray analysis	40
2.3.2 Optical characterization	41
2.3.2.1 Thickness measurement by ellipsometry	42

2.3.2.2	UV-Visible spectroscopy	44
2.3.2.3	Photoluminescence measurement	46
2.4	Device fabrication and measurements	48
2.4.1	Ohmic contact	49
2.4.2	Electronic and optoelectronic measurements	50
2.4.3	Current voltage (I-V) measurement and four point resistivity measurement	50
2.4.4	Thin film transistor characteristics and photoconductivity measurements	52
2.4.5	Gate bias dependent photoluminescence measurement	53
2.4.6	Hall effect measurement	53
3	Large enhancement of ultraviolet photoresponse in nanostructured ZnO film using electric double layer gate dielectric	55
3.1	Introduction	57
3.2	Gate bias dependence of UV Photoresponse and the observed synergy	59
3.3	Effect of grain size on optical gain	63
3.4	Enhancement of field effect mobility under gate and illumination	65
3.5	Transient response of gate current and drain-source current for a step change in gate bias	66
3.6	Discussion	68
3.7	Conclusion	71
4	Control of grain boundary depletion layer using electric double layer gate dielectric	73
4.1	Introduction	74
4.2	Experimental details	76
4.2.1	Films and their characteristics	76
4.3	Fabrication of EDL-TFT and impedance measurement	78
4.4	Basic TFT characteristics	80
4.5	Frequency dependent impedance $Z(\omega)$ with varying gate bias	82
4.6	Model analysis to extract the GB parameters	87
4.7	Conclusion	91
5	High performance flexible thin film transistor (Flex-TFT) based on highly textured ZnO film using electric double layer gate dielectric	93
5.1	Introduction	95
5.2	Fabrication of flexible thin film transistor	97
5.3	Sheet resistance, carrier density and Hall mobility measurement	99
5.4	Performance of flexible thin film transistor (Flex-TFT)	101
5.5	Bending results	108
5.6	Conclusion	109
6	A high performance ZnO nanowire film based broadband photo-detector fabricated with ligand free plasmonic Au nanoparticles synthesized by pulsed laser ablation	111
6.1	Introduction	113
6.2	Decoration of ZnO nanowire by plasmonic Au nanoparticles and fabrication of photodetector	115
6.2.1	Structural characterization of the Au-ZnO NW films	116

6.2.2	UV-Visible absorption of the Au-ZnO NW films	116
6.3	Fabrication of the photo-detector on Au decorated ZnO nanowire film and photocurrent measurement	120
6.4	Broad band photo-response of the Au-ZnO NW film.	120
6.4.1	Change in Photoresponse kinetics	123
6.5	Discussions	125
6.5.1	Relation of photo-current and absorption	125
6.5.2	Origin of enhanced photoresponse	126
6.5.3	Change in kinetics of photo-current relaxation	130
6.6	Conclusion	130
7	Conclusion and future outlook	133
7.1	Conclusion	133
7.2	Future outlook	135
A	Appendix	137
A.1	Transient photocurrent of nanostructured ZnO channel under different gate bias and illumination of different wavelength.	137
	Bibliography	152

List of Figures

1.1	SEM images of ZnO nanostructures (a) nanoparticles, (b) nanostructured film, (b) vertically grown ZnO nanorod and (c) ZnO nanowires.	3
1.2	Energy band diagram of nanostructured ZnO where defect states are lying within the band gap region. The solid red line arrow shows the band to band transition where as the dotted line arrows show the defect state transitions.	3
1.3	Hexagonal wurtzite structure of ZnO	7
1.4	Light interaction evidences on nanostructured ZnO, (a) band to band transition, (b) and (c) intrinsic defect transition, (d) and (e) capture and recombination,(f) trapping and detrapping. Modified from [33].	8
1.5	UV- Visible spectra of nanostuctured ZnO film.	9
1.6	Photo luminescence spectra of nanostructured ZnO film. P_1 represents the excitonic emission peak where as P_2 represents the defect emission peak.	10
1.7	Schematic band diagram of some deep level emissions (DLE) in ZnO nanostructure.	10
1.8	Charging and discharging of EDL capacitor. Adopted from [34]	13
1.9	Simplified illustration of the potential development in the area and in the further course of a Helmholtz double layer. Modified from [35]	13
1.10	Configuration of electric double layer transistor based on ZnO channel.	14
2.1	Schematic diagram of spin coating technique.	29
2.2	Image of Autoclave with Teflon beaker.	31

2.3	Schematic diagram for PLD setup. Wang et. al. ref. [81].	32
2.4	PLD setup in our lab. Courtesy: Ref. [82].	33
2.5	XRD pattern of ZnO target.	34
2.6	SEM image of target pellet of ZnO.	34
2.7	Experimental setup for plasmonic nanoparticle decoration on nanowire surface using laser ablation.	35
2.8	XRD pattern of nanostructured ZnO film grown using sol-gel spin coating technique on quartz substrate at different annealing temperature (350 ⁰ C to 550 ⁰ C).	37
2.9	Williamson Hall analysis of nanostructured ZnO films annealed at (a) 350 ⁰ C (b) 450 ⁰ C and (c) 550 ⁰ C).	38
2.10	SEM image of nanostructured ZnO film. Inset shows the cross-sectional view of the film.	39
2.11	Schematic diagram of the AFM measurement procedure. Courtesy: Ref. [85].	39
2.12	AFM images of nanostructured ZnO film grown in different annealing temperature. Color code representing the height variation on the surface.	40
2.13	EDAX data of nanostructured ZnO film	41
2.14	Schematic diagram of spectroscopic ellipsometry. Courtesy: Ref. [86]	42
2.15	Ellipsometry data of ZnO thin film grown on (a) SiO ₂ /Si (b) polyamide Kapton tape and (c) Al ₂ O ₃	43
2.16	Schematic diagram of UV-Visible spectroscopy [87].	44
2.17	Tauc plot from UV-Visible analysis of ZnO thin film to determine the optical band gap.	45
2.18	Schematic of Fluorometer. Courtesy: Ref. [88]	46
2.19	PL spectra of ZnO nanowire film.	47
2.20	Schematic diagram of field effect device in side gate configuration and ohmic contact. .	48
2.21	Current voltage characteristic in ohmic contact.	49
2.22	Schematic diagram of band structure of metal and ZnO (a) before contact made (b) after contact made.	49
2.23	Van der Pauw resistance measurement configurations.	51

2.24	Measurement set of for transistor characteristics and photoconductivity measurements.	51
2.25	Schematic of gate dependent PL measurement.	52
2.26	Hall effect measurement. Courtesy: Ref. [89]	53
2.27	Cryogen free 10 T magnet. Courtesy: Ref. [82]	54
3.1	(a) Schematic of the field effect device based on nanostructured ZnO channel (b) cross sectional SEM image of ZnO nanostructured film	58
3.2	(a) Dependence of the drain current on the applied gate bias (I_d vs. V_g) in dark and under UV illumination of power (P) of $16 \mu\text{W}/\text{cm}^2$. The I_d is shown in the log scale to accentuate the low dark current. The inset shows the dependence of the ratio (S) on the applied gate bias (V_g). (b) I_d vs. V_g in dark and under UV illumination of varying power (P). The inset shows the dependence of I_d on P for fixed gate bias.	59
3.3	Responsivity (R) as a function of both V_{ds} and V_g . Colour code has shown in right side of the figure.	61
3.4	(a) The current gain (G) as a function of gate bias V_g measured with different illumination power (P). (b) V_{peak} and the maximum value of current gain G (Illumination to dark) plotted for different values of P.	62
3.5	AFM image of nanostructured ZnO films (a) average grain size 25 nm and (b) average grain size 100 nm.	63
3.6	(a) Transfer characteristics of nanostructured with different grain sizes ($\sim 25, 45, 100$ nm) (b) dependence of optical Gain G with gate bias for nanostructured films.	64
3.7	Dependence of field effect mobility (μ_{FE}) on illumination Power (P).	64
3.8	Dependence of (a) Threshold voltage (V_{th}) and (b) Induced surface charge density (Δn_s) on illumination Power (P). The inset in (b) shows that the dependence of the field effect mobility μ_{FE} on the induced surface charge density (Δn_s).	65

3.9	(a) Transient response of gate current $I_g(t)$ and the drain current $I_d(t)$ for a step change of gate bias by 8 V in dark (at $V_{ds} = 5$ V); (b) charge stored in the gate capacitor (Q_g) during the charging, obtained by integrating the I_g shown in (a); (c) the rise of drain current I_d with stored charge $Q_g(t)$ in the gate capacitor.	67
3.10	(a) Dependence of the PL spectra (taken with excitation 340nm) in blue-green region on the gate bias V_g ; (b) intensity at 580nm as a function of gate bias. Negative gate bias enhances the intensity while positive bias decreases it.	69
3.11	Band diagram near GB to explain the effects and band filling.	70
4.1	X-ray diffraction of three PLD grown nanostructured ZnO films used in the work. Film grown on Si/SiO ₂ (Sample A) is nanocrystalline with random grain orientation. Films grown on R-Sapphire (Sample B) and on Kapton [®] (Sample C) are strongly textured in (002) direction.	77
4.2	AFM micrographs of the films grown on different substrates (a) Si/SiO ₂ , (b) R-Sapphire (1102) and (c) Kapton [®]	77
4.3	Schematic of the impedance measurement circuit used.	79
4.4	I - V characteristics of the films measured with the Cr/Au contact pads showing their Ohmic nature.	80
4.5	Transfer characteristics of the gated TFT. The inset shows the characteristics of the sample B (grown on R-Sapphire) in linear scale.	81
4.6	(a) Real (Z') and (b) imaginary (Z'') parts of impedance of sample A for different gate bias.	82
4.7	(a) Real (Z') and (b) imaginary (Z'') parts of impedance of sample B for different gate bias.	83
4.8	(a) Real (Z') and (b) imaginary (Z'') parts of impedance of sample C for different gate bias.	83

4.9	(a) Nyquist plots for the three films taken with different gate bias (a) sample A, (b) sample B and (c) sample C.	84
4.10	(a) Schematic of GB in accumulation region and (b) depletion Region.(Note: The Figure shown is adapted from Reference [108] and modified.)	86
4.11	The network of grains and grain boundaries with model used for fitting.	87
4.12	The obtained parameter R_{GB} as a function of V_g	88
4.13	The obtained parameter (a) C_{GB} as a function of V_g and (b) C_G as a function of V_g	90
5.1	(a) AFM image and (b) XRD pattern of nanostructured ZnO film.	98
5.2	PL spectra of nanostructured ZnO film.	99
5.3	Schematic diagram of Flex-TFT in Hall bar geometry where l , w and t represent the channel length, width and thickness respectively.	100
5.4	Dependence of Hall mobility and sheet resistance on carrier concentration. Inset shows the Hall voltage vs. applied magnetic field.	100
5.5	Transfer characteristic of ZnO Flex-TFT.	102
5.6	Output characteristic of ZnO Flex-TFT.	103
5.7	Transient response in step bias of gate voltage.	104
5.8	Dependence of TFT performance parameters (ON/OFF, V_{th} , SS) with μ_{FE}	105
5.9	Transfer characteristic of Flex-TFT in convex bending of different radius.	108
6.1	SEM images of (a) bare - ZnO nanowire film and (b)-(d) Au-NP decorated NWs with 4,000 (c) 8,000 and (d) 16,000 laser pulses. Increasing number of laser shots lead to increase of Au-NP coverage.	117
6.2	XRD pattern of (a) bare - ZnO NW film; (b) Au-ZnO-8K and (c) Au-ZnO-16K NWs films. The XRD peaks corresponding to Au-NP can be clearly seen.	118
6.3	HRTEM image of the the Au nanoparticles on ZnO NW surfaces.	118
6.4	UV-Visible spectra of bare ZnO NWs film and Au-ZnO NWs films made with different Au coverage (varying number of laser shots). Note the log scale for the absorbance axis.	119

6.5	Schematic of Au-ZnO nanowire film photo-detector.	120
6.6	(a) I-V characteristics of Au-ZnO-16K NW film under dark and under illumination at $\lambda = 350$ nm and $\lambda = 500$ nm; (b) comparison of dark currents in undecorated ZnO NW film and Au-ZnO-16K NW film.	121
6.7	Spectral dependence of the responsivity R in a bare ZnO NW film and in Au-ZnO-16K NW film in UV and visible region. Data taken with a bias of 1 V and with illumination power density $300 \mu\text{W}/\text{cm}^2$	121
6.8	Current gain (G) of bare ZnO NW film and Au-ZnONW film (for Au-ZnO-4K,8K & 16K) (a) $\lambda = 350$ nm and (b) $\lambda = 525$ nm.	123
6.9	Decay of the normalized photocurrent of in bare-ZnO NW film and Au-ZnO NW films taken with (a) UV (350 nm) and (b) visible illumination (525 nm).	124
6.10	Dependence of the optical gain G on the absorption coefficient in the bare-ZnO NW film and that in Au-ZnO-16K NW film. λ_{th} is defined as the wavelength where the G starts to rise.	126
6.11	Schematic of the band diagram of ZnO NW film and Au NP (a) isolated ZnO and Au-NP, (b) ZnO & Au-NP in contact, (c) Indirect transfer of carrier from photoexcited band of Au ($sp/$ SPR) band to CB of ZnO and (d) direct creation of carrier (electron) in conduction band of ZnO.	127
6.12	Reduction of visible emission from Au-NP decorated ZnO. Data taken with excitation of 450nm.	129
A.1	Transient photocurrent of nanostructured ZnO channel without applying gate bias under the illumination of different wavelengths.	138
A.2	Transient photocurrent of field effect device based on nanostructured ZnO channel under illumination of different wavelengths (a) enhancement mode (b) depletion mode.	138
A.3	Normalized transient photocurrent of field effect device based on nanostructured ZnO channel under different gate bias.	139

List of Tables

2.1	Deposition parameter used in sol-gel spin coating technique.	30
2.2	Grain size study using XRD pattern.	38
2.3	Surface and grain size study using AFM imaging	41
2.4	Thickness estimated from ellipsometry measurement	43
4.1	Morphology and thickness of the ZnO films grown on different substrate.	78
4.2	Parameters ξ' and ξ'' at 100 Hz and 10 KHZ.	84
5.1	Characteristic of ZnO Flex-TFT:field-effect mobility (μ_{FE}), subthreshold swing (SS), threshold voltage (V_{th}), and ON/OFF ratio.	106
5.2	Change in performance parameters with bending radius.	109
6.1	Time constants for the decay of photocurrent.	125

Chapter 1

Introduction

In this chapter, we will introduce nanostructured ZnO. We will discuss the physical properties of ZnO and the underlying physics that make it interesting. We will also introduce a electric double layer gate dielectric, which we will use to study the electronic and optoelectronic properties of nanostructured ZnO. The literature survey will be presented to highlight the button line of this thesis.

1.1 ZnO nanostructure

Wide band gap (WBG) semiconductors show superior material properties such as size tuneability and fast current transport. These properties of WBG semiconductors can be utilized to reduce the weight, volume and lifecycle cost in a wide range of applications specially in the field of power electronics. WBG semiconductors absorb and emit light in ultraviolet and visible color range. It can work with high switching speed at high voltage and high temperature.

Various nanostructures can be synthesized from different WBG semiconductors such as SiC, InP, GaAs, CdS, GaN and ZnO for different applications. Among these materials, zinc oxide (ZnO) is one of the promising material for future electronic and optoelectronic applications due to its high exciton binding energy (60 meV), which is higher than the value of GaN. Therefore, significant number of carriers are present as excitons in ZnO at room temperature. The study of ZnO nanostructures and their applications in the field of scientific research and technology have been increased enormously due to development of the growth technology for the high quality of single crystal and epitaxial films. Being a wide band gap semiconductor, the devices based on ZnO can tolerate much higher temperature, higher electric field and high power operation even in small dimensions during its operation [1–4]. These properties can be utilized for energy generation as well as number of conversions. The novel nanostructures of ZnO have tunable sizes and surface morphologies such as nanoparticles, nanostructured films, nanorods and nanowires (Figure 1.1) [4–7] which can open the window for next generation of the electronic appliances (detectors, sensors, thin film transistors, etc.). Among the WBG semiconductors, doping of ZnO by aluminium (Al) and Gallium (Ga) is also considered as an alternative material to replace the Indium Tin Oxide (ITO) due to its low cost, non toxic, large availability and comparable optical and electrical properties to ITO [8–12].

Interest in nanostructured ZnO is increasing steadily in material science and nanotechnology because of its chemistry for synthesis and wet chemical etching which help to reduce the dimensions. With the development of various synthesis techniques of nanostructured material, ZnO nanostructures (thin films, nanowires, nanorods, nanoparticles etc.) can be grown by chemical as well as physical methods

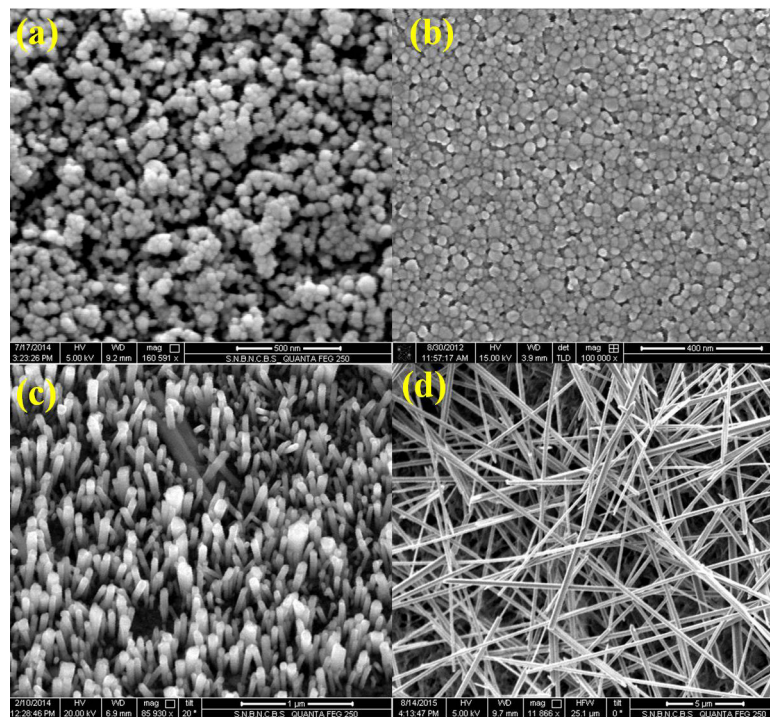


Figure 1.1 SEM images of ZnO nanostructures (a) nanoparticles, (b) nanostructured film, (b) vertically grown ZnO nanorod and (c) ZnO nanowires.

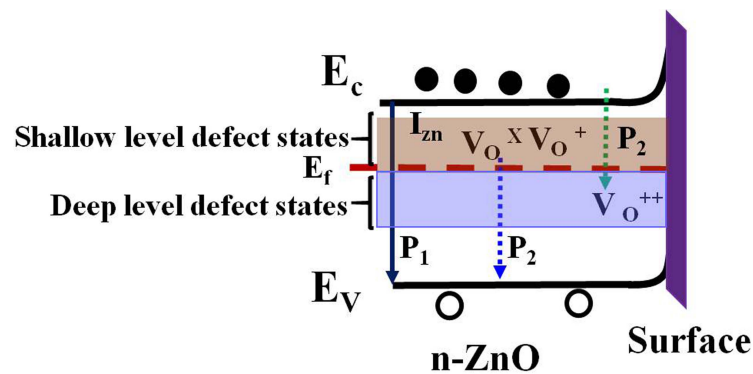


Figure 1.2 Energy band diagram of nanostructured ZnO where defect states are lying within the band gap region. The solid red line arrow shows the band to band transition where as the dotted line arrows show the defect state transitions.

using cheap substrates such as glass, quartz and flexible polymer. In order to utilize the nanostructured ZnO in electronic and optoelectronic applications, it usually requires oriented and defect free, crystal morphology which can be obtained by controlling the growth conditions. The physical process like

pulsed laser deposition (PLD) technique is useful to get good crystalline quality with highly oriented nanostructures of ZnO even at low temperature on flexible substrate.

Besides above explained significant physical parameters and applications, nanostructured ZnO has serious drawbacks because of large number of grain boundaries (GBs) and native point defect states such as Zn interstitials (I_{Zn}), neutral and charged oxygen vacancies (V_O^X , V_O^+ , V_O^{++}) which are lying within the band gap region (Figure 1.2) [7, 13–19]. Due to this native point defects, ZnO is inherently n-type semiconductor but it is very sensitive to environment and easy to form the defects by absorbing water vapour or air molecules. These defect states at the surface play crucial role for the carrier transport phenomena and control different physical properties (light absorption, emission, photoconduction, carrier relaxation dynamics etc.) of nanostructured ZnO. The GB regions in nanostructured ZnO consist of large number of defects which form potential barriers (or depletion layers) at the grain-grain interface [20,21]. GB potentials strongly suppress the drift of majority charge carriers and provide sufficient number of electrically and optically active charge recombination centres. Surface of ZnO nanostructure is depleted (Figure 1.2) by capturing the free electrons from conduction band by adsorb oxygen molecules which reduces the conductivity of nanostructured ZnO.

In this thesis work, we deal three types of nanostructured ZnO (polycrystalline nanostructured films, highly textured nanostructured films and oriented nanowire films) whose crystal quality, sizes and morphologies depend upon the growth conditions and substrates. We apply chemical method to grow the polycrystalline nanostructured ZnO film on quartz substrate to study photo response near ultraviolet region and the role of neutral and charged oxygen vacancies in photoresponse as well as charge carrier transport phenomena. The mixed orientation of the nanostructured ZnO films favours the high UV photoresponse than the oriented one [22]. The oriented nanostructured films which are grown via physical process like pulsed laser deposition (PLD) technique on flexible substrate used to study the flexible transistor performance and the role of oriented GBs on carrier transport phenomena. The highly oriented ZnO nanowire films are used to fabricated the broad band photo detector by attaching the plasmonic Au nanoparticles on it and study the relaxation dynamics of photogenerated charge carriers.

1.2 Motivation

With the evolution of ZnO nanostructures, there are attempts to sort out its major draw backs associated with surface and bulk related defect states which create the constraints for charge carrier dynamics. In polycrystalline ZnO thin film, the formation of the double Schottky barriers in GB region is considered as main obstacle for device performance. The defect states which are distributed in GB region can capture the electrons and holes from the bulk of the samples which lead to enhance the surface recombination rate and reduce the carrier's life time. The major challenges for UV sensor and detector applications are the slow response and high persistence due to the defect distributions within the band gap. There are so many reports for controlling and reducing the defect density in nanostructured ZnO such as doping, functionalization, surface treatment by hydrogen and oxygen plasma and annealing. In this thesis work, we have applied a novel technique to control the defect states using electric double layer (EDL) gate dielectric in field effect transistor configuration. This method can control the defect states in reversible way without disturbing the crystal structure of ZnO. Different physical parameters such as gate bias, light illumination and surface decoration by plasmonic gold nanoparticles (Au-NPs) can be utilized to understand the charge carrier transport phenomena more clearly and effectively through the defect states in nanostructured ZnO. The basic physical idea that has been utilized is that change of one or more parameters stated above leads to filling/defiling of the defect generated energy levels. These in turn control the electronic and optoelectronic properties of nanostructured ZnO. The polymeric electrolyte which forms an EDL at the ZnO/electrolyte interface is used as a gate dielectric can induce extremely large electric field due to its high value of specific capacitance ($C_i \geq 1 \mu\text{F}/\text{cm}^2$) than the metal oxide gate dielectric [23–28]. As a result, ultra high charge carriers ($\Delta n_s \geq 10^{14}/\text{cm}^2$) are accumulated at the surface at even modest gate bias condition which enables tuning of the Fermi level of ZnO. The large number of charge carriers induced by EDL gate bias can be utilized for controlling the occupation of defect states lying within the band gap as well as the GB barrier formed by depletion layer. There are a few reports where the authors used to study the performance of the charge carriers induce by EDL gate in field effect devices based on ZnO epitaxial or single crystal

substrate. We have investigated the effect of EDL gate bias to control the defect distribution and GB potential in nanostructured ZnO film using polymer electrolyte for the first time.

The EDL gate dielectric can be used to fabricate thin film transistor based on ZnO nanostructured film grown on flexible substrate at low processing temperature. The high quality of metal oxide films presently using as a gate dielectric generally require a high deposition temperature $\geq 400^{\circ}$ C, which is undesirable for flexible electronic. These devices, based on low cost plastic substrate, have the advantages such as low profile, small size and mechanical flexibility. The major goal for the realization of EDL gated flexible field effect transistor (Flex-FET) is to improve the performance of the flexible electronics such as enhancing mobility, increasing ON/OFF ratio, reducing subthreshold swing (SS) by the effect of ultrahigh charge carriers induce by field effect. There is particularly need a high capacitance dielectric medium that can bring down the operating voltage, which is specially desirable for flexible circuit that will be powered by thin-film batteries or lithium ion batteries.

Functionalization or decoration of the plasmonic nanoparticles on nanostructured ZnO surface is a novel technique that modulates the physical process such as light absorption, defect emissions, and photoconduction. Therefore, the optical properties of nanostructured ZnO can be drastically changed when they are in contact with plasmonic Au nanoparticles (Au-NPs). The ZnO based photo detectors have a limitation that it works only in UV region which is the fundamental band gap of ZnO. The attachment of plasmonic Au-NPs on nanostructured ZnO resolves this problem and the ZnO based UV photo detectors work significantly in broad band photo detection practically in visible. One major drawback in ZnO based UV detector is slow response that is controlled by charge recombination path through defect states. It is necessary to improve the slow response of the detector based on metal oxide semiconductors before they can be made useful. The relaxation of the photogenerated charge carriers can be controlled by EDL gate bias as well as surface decoration by plasmonic Au nanoparticles.

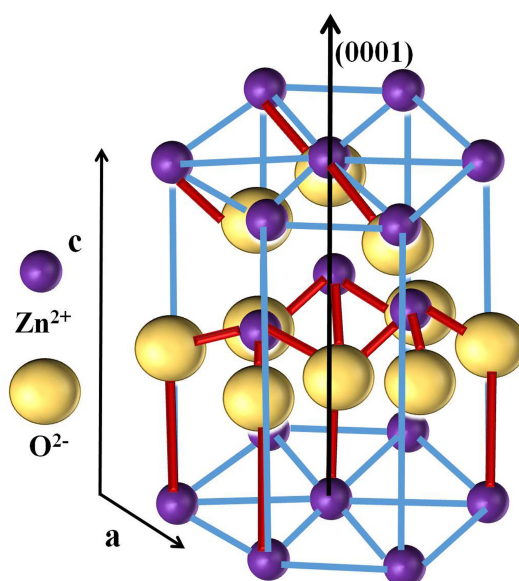


Figure 1.3 Hexagonal wurtzite structure of ZnO

1.3 Basic properties of ZnO

1.3.1 Crystal structure

ZnO crystallizes into the hexagonal wurtzite (Figure 1.3) structure with number of alternating planes. These planes are tetrahedrally bonded between O_2^{-2} and Zn^{-2} atoms which are stacked along c axis. The Zn terminated or O terminated planes (basal planes) along c axis have highly polar behaviour. The polar nature of the ZnO, arises due to net dipole moment along c axis. The tetrahedral coordination in ZnO gives the non central symmetry structure, which favours piezoelectricity and pyroelectricity [5]. Large electronegativity of oxygen atoms favours the ionic behaviour between these two planes. The Zn polar surface may absorb the hydroxyl (OH^-) ions from the atmosphere and forms the hydroxide layers. The density of surface states are higher in Zn terminated (0001) faces than the O terminated ($000\bar{1}$) face. The wurtzite ZnO consists with lattice constants of $a = 3.249 \text{ \AA}$ and $c = 5.205 \text{ \AA}$. Due to difference of surface energy exists between two basal planes (Planes perpendicular to the c axis. one consists with Zn terminated plane (0001) and other oxygen terminated plane ($000\bar{1}$)), these planes are in favour to the crystal growth. In newly formed ZnO molecules, the polar surface favours to

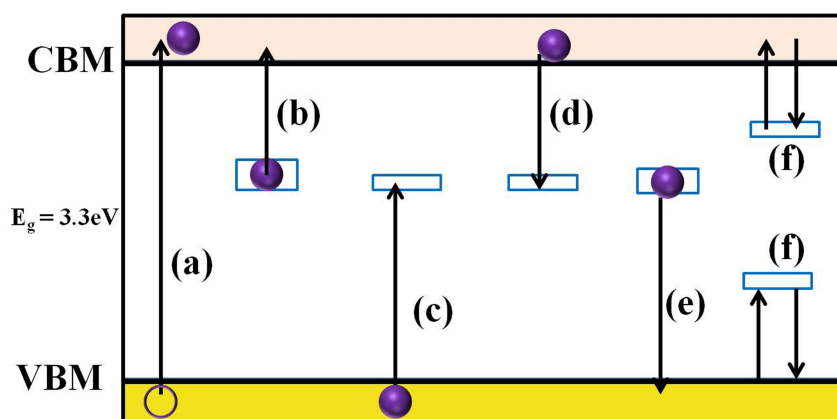


Figure 1.4 Light interaction evidences on nanostructured ZnO, (a) band to band transition, (b) and (c) intrinsic defect transition, (d) and (e) capture and recombination, (f) trapping and detrapping. Modified from [33].

stick to the incoming precursor molecules. After deposition of one layer, the Zn^+ terminated surface change into O^{-2} terminated surface or vice versa. Such growth process is repeated over a time which enhance the growth along $\pm(0001)$ plane i.e. along C-axis rather than the other commonly observed non polar planes $(11\bar{2}0)$ and $(10\bar{1}0)$. The non polar planes contains equal number of Zinc and Oxygen atoms. Thus the polar behaviour of nanostructured ZnO is responsible for the various properties like piezoelectricity, crystal growth and defect generation. [4, 5, 29–31].

1.3.2 Optical properties

The study of the optical properties of ZnO has a long history that stated in 1960 [32] and recently it has become more interesting compared to other wide band gap semiconductors because of its direct wide band gap with large exciton binding energy at room temperature. It is transparent in visible region and good UV absorber and emitter. The optical properties of the ZnO depends on both the intrinsic and extrinsic defects. Interaction of light with ZnO follows various physical process such as optical absorption, transmission, reflection, photoluminescence and cathodoluminescence.

The light absorption in ZnO by interband transition creates electrons in conduction band and holes in valence band. These electron hole pairs in same space point, bind with coulomb interaction as excitons and act as energy carriers like photons. The required condition for the exciton formation is the group

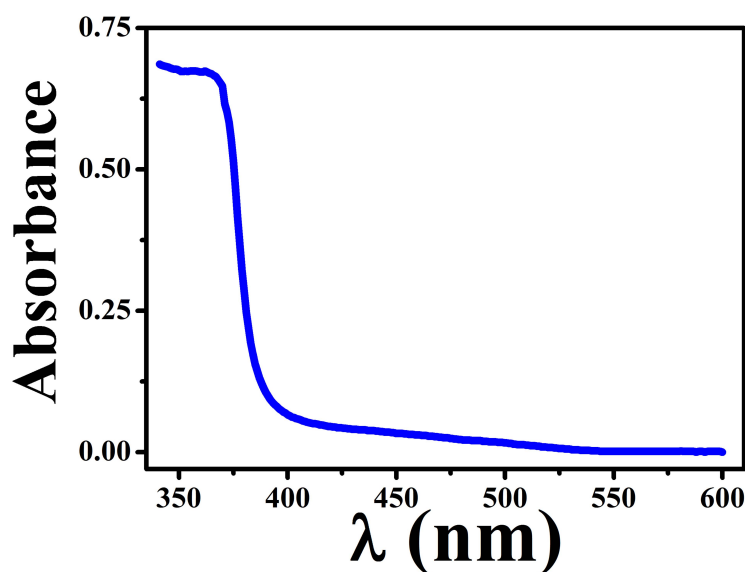


Figure 1.5 UV- Visible spectra of nanostructured ZnO film.

velocities of electron and hole should be same. Optical processes in various nanostructures of ZnO are connected with the intrinsic and extrinsic defects. The optical absorption is associated with the transition of electrons from valence band to the conduction band ((a) in Figure 1.4) and also it includes to the raising of electron from defect levels to conduction band ((b) in Figure 1.4) or from valence band to defect levels ((c) in Figure 1.4). During absorption process, electrons and holes trapping and detrapping from conduction band and valence band by defect centres represent by (f) in Figure 1.5. Defect states create the discrete electronic states within the band gap region which play the vital role for optical absorption and emission in this material. In other words, defect states lying within the band gap control the optical absorption and emission in nanostructured ZnO.

The UV visible spectra (Figure 1.5) of nanostructured ZnO film shows the strong band gap absorption around 380 nm ($E_g = 3.26$ eV). The absorption of the film strongly depends on the grain sizes and defects states that can be utilized to study the photoresponse behaviour of the nanostructured ZnO films.

Defect levels in ZnO can be characterized by optical and electrical methods. In optical methods photoluminescence and cathodoluminescence spectroscopy is used without metal contacts. These methods give information about charge carriers transitions such as band to band, localized states to band and

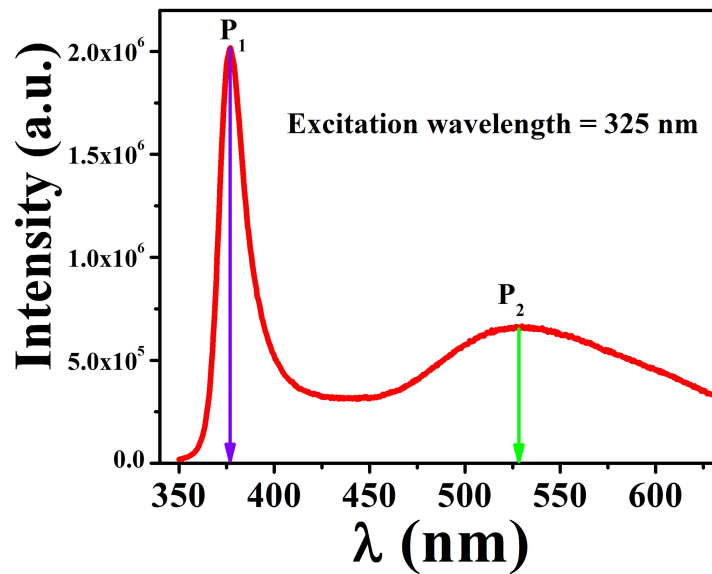


Figure 1.6 Photo luminescence spectra of nanostructured ZnO film. P_1 represents the excitonic emission peak whereas P_2 represents the defect emission peak.

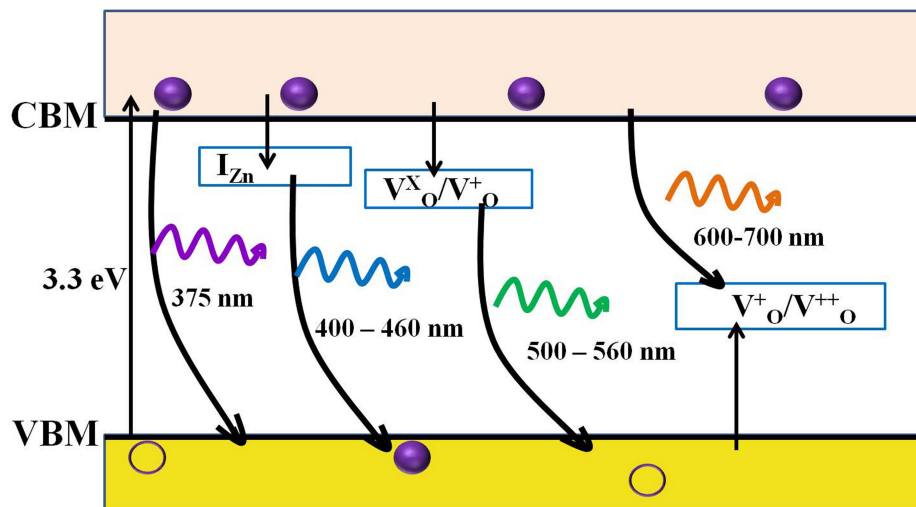


Figure 1.7 Schematic band diagram of some deep level emissions (DLE) in ZnO nanostructure.

through the various defect states. PL measurement is a non destructive and suitable tool to determine the crystal quality and the presence of the defects as well as exciton fine structures. The nanostructured ZnO exhibits wide variety of PL spectra which cover almost the whole visible region to the near UV region from 2 eV to 3.4 eV. The spectra of nanostructured ZnO lie near UV region consist of excitonic

emission that may be bound or free excitons. If the excitons have the large radius i.e. electrons and holes are separated over many lattice constants, the exciton wave functions are delocalized and they can move freely inside the crystal such excitons are called free excitons. If the crystal have large number of defect states which also represent the efficient trap centres, then the free excitons propagating through the crystal get localized (loosing their kinetic energy) at the defect states thereafter bound excitons are created.

The room temperature PL spectra of the oriented ZnO nanowire films is shown in Figure 1.6. The intensities and positions of the emission spectra depend on the defects distribution in nanostructured ZnO. Generally the polycrystalline nanostructures having large number of grains can give rise to the weak band gap and strong visible emission spectra. On the other hand the highly oriented or less defective single crystal of ZnO gives the strong band gap and weak visible emissions. The origin of defect emissions in visible region is attributed to shallow and deep level defects in nanostructured ZnO. There are three basic visible emissions such as blue-green, yellow and orange-red emissions [4, 7, 16–18]. These emissions are depends upon the types of defects formed rather than the surface morphology of the nanostructured ZnO. The peak position of defect emission may change with temperature and the excitation wavelength [18]. These defect states in ZnO are introduced at the growth time and can be controlled by growth conditions like deposition temperature, oxygen pressure and annealing temperature.

ZnO consists of shallow donor and acceptor energy levels below and above the conduction band and valence band respectively which are responsible for near band edge emission in addition to the fundamental gap. The most familiar intrinsic defects in ZnO are neutral and charged oxygen vacancies (V_O , V_O^- , V_O^{2-}), oxygen interstitial (O_i), zinc vacancies (V_{Zn}), zinc interstitial (Zn_i), oxygen anti-site (O_{Zn}) and zinc anti-site (Zn_O) which are responsible for visible emission throughout the visible range from 425 nm to 700 nm (Figure 1.7). In ZnO most common intrinsic defects are oxygen and zinc vacancies which are created by missing the host atom in the regular crystal structure. Oxygen vacancies are assumed the origins of green emissions.

The electrical and optical properties of nanostructured films can be controlled by controlling the nature

and quantity of defect states. The control mechanisms of these defect states are described in later section.

1.3.3 Electrical properties

It is important to know the electrical properties of ZnO for applications in nanoelectronics. All form of ZnO nanostructures are inherently n-type due to the presence of native donor defect states such as oxygen vacancies or zinc interstitials. The electron mobility of ZnO is not constant and it depends on the growth methods which is approximately $0.1 \text{ cm}^2\text{V}^{-1}\text{s}^{-1}$ - $100 \text{ cm}^2\text{V}^{-1}\text{s}^{-1}$ at room temperature. As a wide band gap semiconductor, ZnO nanostructures are associated with ability to sustain large electric fields (high break down voltage), high temperature and high-power operation. Carrier concentration of undoped ZnO lies within the range of 10^{16} - 10^{19} cm^{-3} . The mobility of the ZnO is high enough with comparison to the amorphous silicon and organic semiconductors.

1.4 Overview of electric double layer (EDL) as gate dielectric

Charge control by using electric double layer (EDL) gate dielectric has recently emerged as a strong tool to control the Fermi energy (E_F) in solid. The EDL acts as a nano gap capacitor with a huge capacitance and can accumulate and deplete charge carriers over a wide range. Some interesting physical phenomena such as superconductivity, metal insulator transition and thermoelectric behaviour have been modulated by using EDL gate dielectric in transistor configuration [26].

An electrolyte (liquid or solid) with mobile ions (cations and anions) is filled in between two electrodes (Figure 1.8) can be used as an EDL capacitor. Double layers are formed between the electrodes and electrolyte which consist of the space charge at electrodes and an ion space charge in the electrolyte under external electric field. Cations and anions are moved to the surface of EDL during its charging process. The EDL capacitor (EDL-C) is discharged by removing the external voltage. The operation of EDL-C is based on ion absorption and desorption to the EDL during its charging and discharging

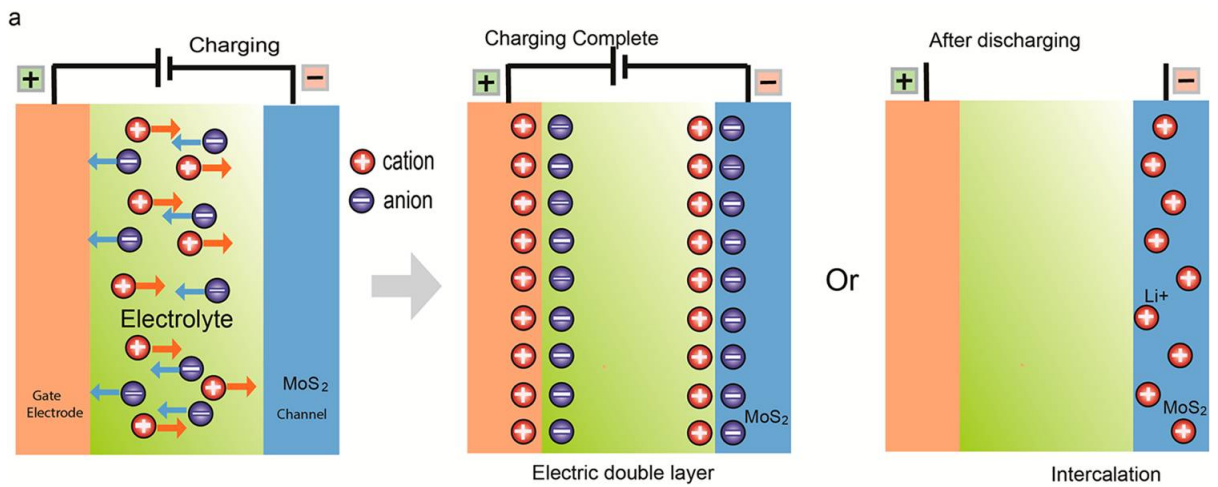


Figure 1.8 Charging and discharging of EDL capacitor. Adopted from [34]

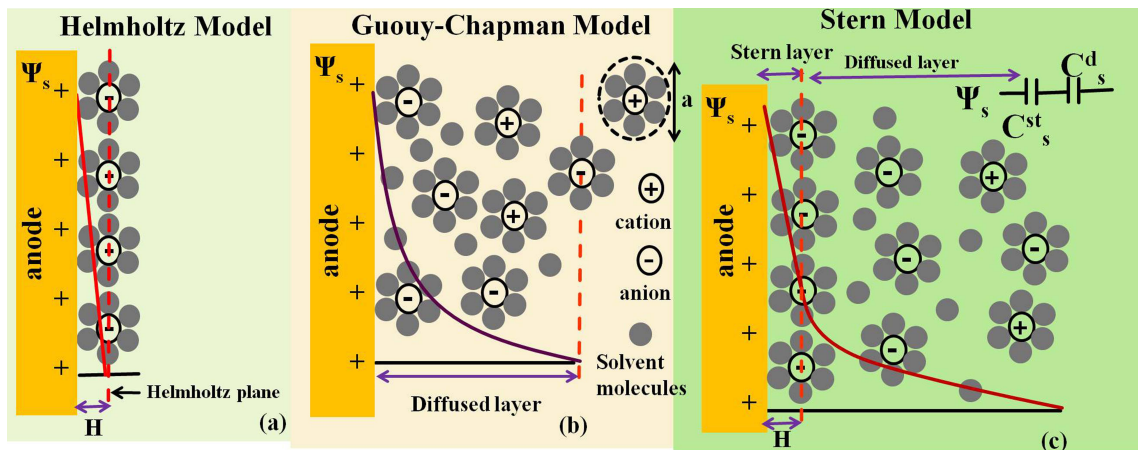


Figure 1.9 Simplified illustration of the potential development in the area and in the further course of a Helmholtz double layer. Modified from [35]

process.

Three fundamental models have been proposed to explain the EDL theory. The early model proposed by von Helmholtz (Figure 1.9 (a)) in 19th century where the EDL is formed by absorbing the opposite ions from electrolyte at the surface of charged electrodes. The potential profile is linear with distance within the EDL. This model is analogous to the conventional dielectric capacitors with two planar electrodes separated by a distance H . Later on Gouy and Chapman introduced the diffusion of ions in electrolyte (Figure 1.9 (b)). The charge distribution of ions as a function of distance from the

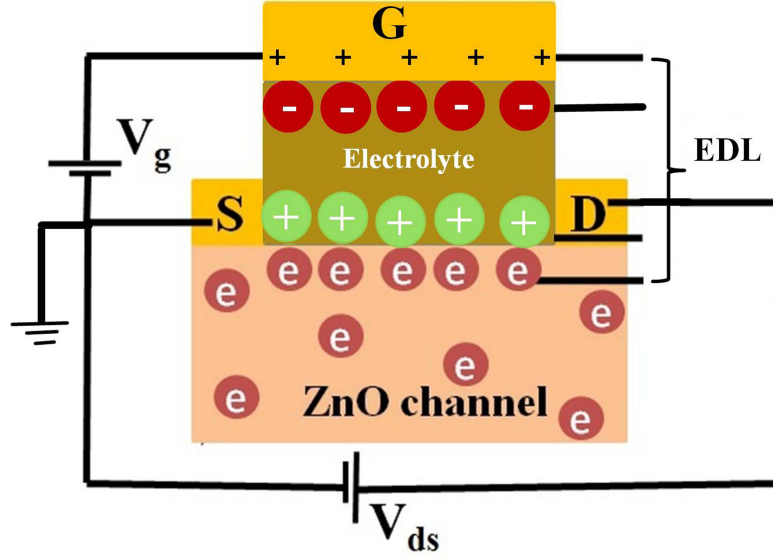


Figure 1.10 Configuration of electric double layer transistor based on ZnO channel.

metal surface follows the Maxwell-Boltzmann statistics and the electric potential decreases exponentially away from the surface of the fluid. Figure 1.9 (c) explains the Stern model by the combination of Helmholtz and Chapman model. This model defines Stern layer (or Helmholtz layer) on the basis of the Helmholtz plane. Stern layer and the diffuse layer are in series and the distance of the diffuse layer is increasing with increasing the concentration of the ions. The total electric double layer capacitance consists with the stern layer capacitance (C_S^H or C_S^st) and diffuse layer capacitance (C_S^D) in series. The capacitance per unit surface area or specific capacitance of the Helmholtz double layer denoted by C_S^H is given by [35]

$$C_S^H = \frac{\epsilon_0 \epsilon_r}{H} \quad (1.1)$$

where ϵ_0 and ϵ_r are the free space permittivity and the relative permittivity of the electrolyte solution, respectively.

The diffused layer capacitance is given by

$$C_S^D = \frac{\epsilon_0 \epsilon_r}{\lambda_D} \left(1 + \frac{\lambda_D}{R_0}\right) \quad (1.2)$$

Here the λ_D is the Debye length for symmetric electrolytes which is defined as $\lambda_D = (\epsilon_0 \epsilon_r K_B T / 2e^2 z^2 N_A c_\infty)^{1/2}$ where, K_B = Boltzman constant N_A = Avogadro's number c_∞ is molar concentration of ion species. Equation 1.2 reduces to $C_S^D = \frac{\epsilon_0 \epsilon_r}{\lambda_D}$ as $\frac{\lambda_D}{R_0} \ll 1$. The value of capacitance can be about a few $\mu F/cm^2$ due to the small value of H and λ_D .

The distance between the ion layer in electrolyte and the charge layer in electrodes is about a nanometre range which is equivalent to the size of ions. This nano gap thickness builds up a huge capacitance at the interface and it can modulate the semiconducting channels electrostatically by accumulating and depleting the charge carriers ($\geq 10^{14}/cm^2$) at the interface under a low gate bias [26]. EDL gated transistors mostly use the ionic liquids and polymer electrolytes to enhance the electrical performances of the devices. The conventional metal oxide gate dielectrics have low charge accumulation capacity ($\approx 10^{12}/cm^2$) due to its low value of capacitance. Though it can modulate the conductivity of the semiconductor channel but insufficient to induce the drastic change in electronic and structural properties such as metal insulator transition, superconductivity and ferroelectricity. Therefore, EDL gate dielectric, a new tool is realized that can solve these problems under low operating gate voltage. On the other hand the oxide based semiconductors have high value of intrinsic charge carrier density which is often in excess of $10^{19}/cm^3$. The conventional oxide gate dielectric unable to modulate such a high value of charge carriers more effectively which further justify the necessity of the electric double layer gate dielectric to study the transport properties of charge carriers in oxide semiconductors.

Figure 1.10 show the configuration of electric double layer transistor (EDLT) based on ZnO nanostructure channel. The electrolyte is sandwich in between the gate electrode and ZnO with source drain electrodes. Thus the EDL-C is transferred to EDLT by replacing one of the electrode by ZnO channel. In this configuration, EDLs are formed at gate /electrolyte and semiconductor/electrolyte interface when a gate bias is applied.

Panzer and Frisbie [27] fabricated a polymer electrolyte gated organic field effect transistor. They used polyethylene oxide (PEO) film containing a dissolved Li salt to modulate the hole conductivity of polymer semiconductor. In this report, EDL formed by the polymer electrolyte induced $\simeq 2 \times 10^{14}$ holes/ cm^2 with application of -3 V to the gate electrode. This high carrier density produced very high

source drain current with hole mobility $\geq 3 \text{ cm}^2/\text{Vs}$. Similarly, Shimotani et. al. [28] reported a metal insulator transition in ZnO single crystalline thin film using EDL as gate dielectric. They showed the carrier density of $4.2 \times 10^{13} \text{ cm}^{-2}$ by Hall measurement and the room temperature sheet conductance was $\sim 1 \text{ mS}$ which was sufficient to maintain the metallic state down to 10 K. The gate controlled persistence of the photoconduction is observed in single crystal of ZnO [36] using EDL gate dielectric. The photocurrent get enhanced with the application of moderate gate bias and a substantial part of the enhanced photocurrent is retained for a long time when the illumination is off in under the bias condition unchanged. Beside ZnO, the polymer electrolyte can be used to study the charge transport phenomena in other materials such as, organic semiconductors [25] carbon nanotubes etc. [37] Similarly, the electric field controlled charge carrier density induce the super conductivity in SrTiO_3 single crystal channel using polyethylene oxide (PEO) and lithium perchlorate (LiClO_4) as gate dielectric [38]. There are so many other reports such as Lee et. al. [24], Shibata et. al [39], Fujimotoa et. al. [40], Nath and Raychaudhuri [41, 42] and Zhou and Ramathan [43] reported the EDL field effect transistor to study the transistor performance, charge transport phenomena in correlated electron system in oxide and perovskite materials. We have used EDL gate dielectric to modify the electronic phenomena of carriers in nanostructured ZnO films grown on different substrates such as quartz, SiO_2/Si , Sapphire and flexible Kapton substrate using chemical and physical methods. In Flex-FETs polymer electrolyte is suitable dielectric material due to its flexibility, transparency, low-cost and low temperature processing beside high value of specific capacitance.

1.5 Overview on control mechanisms of defect states in ZnO nanostructures

In this thesis work, we have investigated electrical and optoelectronic phenomena in nanostructured ZnO using two different tools such as EDL gate bias and surface decoration by plasmonic Au-NPs. Nanostructured ZnO have large number of grain boundaries with large number of defect distribution

which determine the overall performances of ZnO based devices. EDL field effect transistor (EDL-FET) is utilized to modify carrier transport phenomena through the GB region. Our main focus is to investigate the effect of EDL gate dielectric on surface and deep level defect states which play a vital role for different physical properties such as photo absorption, emission, photoconduction and carrier relaxation. Several authors have reported different ideas for controlling the surface and deep level defects, these are annealing, doping, functionalization, passivation by surfactant etc. The literature survey of this thesis work point out some important and fundamental ideas for controlling the defect states in nanostructured ZnO which are explained below.

Xu et. al. in 2004 [44] prepared ZnO:F film by thermal oxidation of ZnF film grown on Si substrate by e beam evaporation technique using Zinc fluoride ($ZnF_2, 5N$). They reported that F atoms whose ionic radius is quite similar to that oxygen, occupied the lattice sites of the oxygen vacancies with minimum lattice distortion. The incorporate F atoms passivated the surface defect states and decreased the probability of the formation of defect emission centres which reduced the intensity of visible emissions in PL spectra.

Electric field controlled photoluminescence of ZnO is observed in two terminal device based on metal (Au), insulator (SiO_2), semiconductor (ZnO) (MIS) structure [45]. For positive bias on MIS device, concentration of electrons increased significantly at the surface (insulator-semiconductor interface) and enhanced the near band emission. The carrier recombination time for ZnO is extremely short. Therefore, there was no significant change in hole concentration at interface during positive bias. The radiative recombination rate is proportional to the product of concentration of electrons and holes. As the accumulation of the electrons increased at the surface during positive bias, the deep level centres contributing the visible emissions were reduced than the without bias condition. Therefore, the intensity of the visible emission was decreased with increasing the positive bias [45].

In 2007 Djuricic et. al. [17] reported the effect of annealing and the role of surfactant on the defect emissions in different ZnO nanostructures. They observed the defect emissions such as yellow and orange-red emissions strongly depended on the annealing temperature where as the green emission was not significantly affected by annealing. They also observed the effect of surfactant (3-

aminopropyltrimethoxysilane) on the surface of ZnO nanostructure which prevented the adsorption of hydroxyl ion from the atmosphere and there was no significance change in defect emission with time of air exposure. The most common defect emission in PL spectra of different nanostructured ZnO are blue-green emission, yellow emission and orange-red emission. These emission spectra can be influenced with the excitation wavelength therefore their peak positions and intensity are changed according to the excitation wavelength [18]. In the same year, Oh group [46] studied the electrical properties of ZnO:Al films. They reported the resistivity of as grown film was increased from 4.8×10^{-3} to $1.1 \times 10^{-2} \Omega\text{cm}$ after 20 days and it becomes $2.4 \times 10^{-2} \Omega\text{cm}$ after 40 days. The increase in resistivity of the film was due to the enhancement of defect density in GB region with time of air exposure, which reduced the carrier mobility significantly. To solve this problem, they annealed the film in hydrogen ambient and they observed no significant change in the resistivity of the films with time of air exposure. This report supports that the defects at grain boundaries can be removed by surface passivation after annealing the film at hydrogen ambient.

Ghosh and Raychaudhuri in 2008 [47] reported control of visible photoluminescence in ZnO nanostructures by changing the ionic environment of the suspension medium. In this experiment, ZnO nanoparticles and nanorods dispersed in ethanol having different LiClO_4 concentrations. As the concentration of electrolyte increased, the intensity of visible Photoluminescence decreased and almost completely quenched in maximum electrolyte concentration used. They reported that the change in visible emission occurred due to the change in the surface charge of the nanostructured ZnO and also correlated to the zeta potential of medium. By changing the concentration of the ionic medium, the surface charge on ZnO nanostructure affects the band bending and also controls the defect centres associated with visible emission. In 2010 same authors reported the reversible control of the photoluminescence in nanostructured ZnO where ZnO was sandwiched in between the ITO and solid polymer electrolyte [48]. The reversible control of the defect emission in PL spectra of ZnO arised because of changing the occupation of oxygen vacancies near the surface of ZnO nanostructure and polymer electrolyte interface by the application of bias.

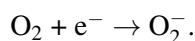
Cai et. al. 2009 [49] studied the effect of hydrogen plasma treatment on ZnO films grown by radio

frequency magnetron sputtering. They reported the carrier concentration as well as the mobility of the film increased after hydrogen plasma treatment. The incorporation of the H atom after plasma treatment introduced shallow donor states as $V_o - H$ complex and interstitial hydrogen to increase the carrier concentration. It also passivated the most of defect states that lead to increase of the mobility and decrease of the intensity of defect emission. Similarly, Papamakoris et. al. [50] modified the surface of ZnO by hydrogen plasma treatment and used as a bottom cathode contact for polymer solar cell. Hydrogen plasma treatment passivated the defect or dangling bond on the surface of ZnO which reduced the carrier recombination rate and prolonged the carrier lifetime and improved the device performances. They observed the significant suppression of the visible photo luminescence spectra of hydrogen plasma treated ZnO film.

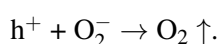
Yuan et. al. [23] in 2009 studied the effect of EDL gate dielectric on ZnO single crystal substrate using ionic liquid (IL). They showed the high performance of EDL gate transistor with high value of transconductance. They measured the high value of EDL capacitance $\sim 34 \mu\text{F}$ by Hall effect measurement. This high value of capacitance utilized to induce the ultrahigh charge carrier density (n_s) $\geq 4.5 \times 10^{14}/\text{cm}^{-2}$ under low gate bias $\leq 3 \text{ V}$ at room temperature. They reported that the value of n_s accumulated at room temperature decreased with decreasing the temperature due to the voltage drop in EDL during cooling. But, they applied higher gate voltage (V_g) and got the value of $n_s \sim 5.5 \times 10^{-14} \text{ cm}^{-2}$ at 1.8 K. They claimed that the experiment opened the new window for further research in electron correlation phenomena such as field induced superconductivity.

Reyes et. al. [51] fabricated a UV photo detector based on oxygen plasma treated ZnO thin film as a channel material and SiO_2 a gate dielectric. Photo detector showed high ON/OFF current ratio of $\sim 10^{10}$ with UV to visible rejection ratio of $\sim 10^4$ at -10 V gate bias. In this report, they explained the slow recovery of the photocurrent is mainly due to the oxygen absorption, desorption & defect related recombination process as follows:

I. In dark condition oxygen molecules adsorb at the surface states (Oxygen vacancies site) create negatively charged ion by capturing free electrons which reduce the conductivity of the film. The reaction can be described as:



II. On UV illumination, photodesorption of O_2 take place where negatively charged oxygen ion captured the photo generated holes that migrate towards the surface of ZnO and the reaction can be described as:



Therefore, large number of oxygen vacancies at the surface of the channel reduced the rate of carrier recombination after illumination is off which increase the persistence of the photoconductivity. In this experiment PPC was suppressed using oxygen plasma treatment on ZnO films.

In 2012, Thiemann group [52] reported electrolyte gating of ZnO FET using IL. They investigated different ILs and supposed to increase the electrochemical window. They reported that changing the chemical structure of the IL can tune the threshold voltage and field effect mobility for electron transport in ZnO FETs. They also improved the long term stability of electrolyte gated ZnO FETs by certain ILs and can be increased further by passivation of ZnO surface.

Pattanasattayavong et. al. [53] reported dye-sensitized ZnO phototransistor with extremely high photoresponsivity. They used chemically grown ZnO film functionalized with organic dye as a channel material and SiO_2 as gate dielectric. They observed extremely high photosensitivity to green light (10^6) & maximum responsivity $\sim 10^4$ A/W. They explained that the large value of responsivity arose due to the charge transfer from optically sensitive organic dye to ZnO and enhanced the mobility. The charge generated by illumination utilized to reduce the grain boundary scattering by shielding effect.

Chang et. al. [54] reported the high performance of metal oxide thin film transistor which was fabricated by LiF doped ZnO thin film grown from aqueous solution. The drain current of TFT was increased with introducing the LiF up to 10 mol%. However further increasing the dopant concentration drain current was decreased. According to their doping mechanism, the Li in ZnO matrix prefer interstitial sites due to it's low electron affinity which can produce the electrons ($\text{Li} \rightarrow \text{Li}^+ + \text{e}^-$) and improves the carrier concentration. Mean time F occupies the substitutional oxygen sites ($\text{F} \rightarrow \text{F}_\text{O} + \text{e}^-$) which is more favourable compared to fluorine interstitial sites. In this experiment, F incorporation in oxygen sites diminished the oxygen vacancies and reduced the carrier scattering centres. Therefore,

the codoping of Li and F ion increased the mobility and decreased the optical absorption.

Xu et. al. [55] improved the mobility and reliability on ZnO based thin film transistor by hydrogenation. Hydrogen atoms acted as a defect passivator as well as shallow n-type dopant. However excess doping of H atom deteriorated the devices and became very conductance. They have reported that doping metal atoms such as Mg in hydrogenated ZnO can effectively decrease the formation energy of interstitial H and increase the formation energy of O- vacancies. This experiment showed that the dilute doping in hydrogenated ZnO film enhanced the mobility from 10 to 32 cm²/Vs due to the decreased electron effective mass by surface band bending.

Abliz et. al. [56] designed bilayers structure (ZnO-ZnO:H) to improve the performance of TFT based on ZnO thin film without doping. The electrical performance of hydrogenated single layer of ZnO is not reliable and degraded with over treatment with hydrogen. To overcome this drawback, they designed the novel structure of ZnO:H (~ 3 nm)/ZnO(~ 20 nm) bilayer TFTs. The bilayer TFTs exhibited high electrical performances and a good reliability including μ_{FE} of 42.6 cm² /V s, I_{on}/I_{off} of 1×10^8 , SS value of 0.13 V/dec. and V_{th} value of 1.8 V. They have claimed that the good performance of the TFTs are attributed to the ultrathin ZnO:H layer. The surface of the ZnO:H became smooth by the etching effect of hydrogen treatment and had the low trap density at ZnO-ZnO:H interface and also the carrier concentration increased with hydrogenation.

Choi et. al. [57] used a photo pattern ion gel from EDL gate dielectric with high capacitance to improve the transistor performance for both n-type (ZnO) and P type (P₃HT) channel. They claimed that their transistor displayed high carrier mobility (electron mobility of ~ 0.7 cm²/V.s. and hole mobility of ~ 1.4 cm²/V.s & ON/OFF current ratio ~ 10⁵ at 2 V bias. In this experiment, they demonstrated that the ion gel based on triblock copolymer with azide group can be cross-linked by UV irradiation using shadow mask without changing the microstructure of the ion gel. The pattern ion gel allowed to metal deposition on top of it without formation of gate to channel short. this report suggested that photopatterning is a promising idea to incorporate high capacitance EDL gate dielectric into FETs for printed electronics.

In 2012 Jeon et. al. [58] used three terminal device architecture to control the persistent photoconductivity

(PPC) in oxide semiconductor using SiO₂ as gate dielectric. They explained that the gate bias control the position of the Fermi level in channel. The voltage pulses induced the the electron accumulation and accelerated their recombination with charged oxygen vacancies which were the main cause of PPC. There are many reports such as Yakuphanoglu [59], Lee et. al. [60], Xiong et. al. [61], Bae et. al. [62], Hou et. al. [63], Lee et. al. [64], Kimoon Lee et. al. [65] and Chen et. al., [66] where the authors reported the photo response and the transistor performances based on ZnO nanostructured film using different gate dielectrics (SiO₂, polyvinylphenol, aluminium titanium oxide etc.). In these reports authors did non discuss the role of defect states for carrier transport phenomena.

Defect modification mechanisms reported by various group as explained above are not well control and a single step method. Among them, defect control by annealing is not suitable for low temperature flexible substrate. similarly, defect control by doping a foreign element can be changed the crystal structure and over doping reduced the mobility of the carriers, in this way this is also not a appropriate way to control the defect states in nanostructured ZnO.

In this thesis, we have applied a novel technique to control the surface and deep level defect states by filling and defiling the charge trap states using EDL gate bias in reversible way without disturbing the crystal structure. The nanostructured ZnO also consists of large number of GB regions which are depleted regions. We have used the field induce charge carriers to modulate the depletion width of GB regions using EDL gate bias.

Using EDL as a gate dielectric is a viable option for fabrication of flexible thin film transistor at low temperature. Brief overview of EDL gate dielectric on flexible thin film transistor (TFT) will discuss in chapter 5. In this thesis, we have used EDL gate dielectric to study the performance parameters of flexible TFT.

Surface plasmons excited at interface between metal nanostructure and semiconductor has attracted great interest due to its wide applications in enhancement of the weak physical process and applications such as light absorption, Raman scattering, sensors, detectors etc. We have used plasmonic Gold nano particles (Au-NPs) to enhance and extend (UV to visible) the photoresponse and controlled the relaxation of photogenerated charge carriers through the defect levels. In this thesis, we have synthe-

sized and attached the Au-NPs on ZnO surface using ligand free pulsed laser ablation method. A brief overview about role of Plasmonic Au-NPs on ZnO nanowire surface after attachment is discussed in chapter-VI of this thesis.

This thesis is made following chapters:

Chapter 1: Introduction; **Chapter 2:** Sample preparation, characterization and measurement techniques; **Chapter 3:** Large enhancement of ultraviolet photo response in nanostructured ZnO film using electric double layer gate dielectric; **Chapter 4:** Control of grain boundary depletion layer using EDL gate dielectric; **Chapter 5:** High performance thin film transistor based on highly textured ZnO film using EDL gate dielectric; **Chapter 6:** A high performance ZnO nanowire film based broad band photo detector fabricated with ligand free plasmonic Au nanoparticles synthesized by pulsed laser ablation and **Chapter 7:** Conclusion and future outlook.

Chapter 2

Sample preparation, characterization and measurement techniques

Sample preparation and its characterizations are very sensitive and important ingredients for understanding the physical properties of materials. In this chapter, we discuss a brief overview of sample preparations, characterizations and measurement techniques for nanostructured ZnO used in this thesis. The growth techniques for different forms of nanostructured ZnO are done using both chemical and physical methods. The samples are characterised by XRD, SEM, EDAX, TEM, HRTEM, AFM and Ellipsometry. The electronic and opto-electronic measurements are performed using four probe station attached to a light source. The Hall measurement is carried out using cryogen free super conducting 10 T magnet at room temperature.

2.1 Introduction

Synthesis and characterizations of the nanostructured materials are necessary steps for experimental work in the field of condensed matter physics and material science. The quality and features of the nanostructured materials are greatly influenced by the growth methods. The growth parameters help to "engineer" the desired properties of the nanostructured materials. In this thesis work, we have investigated the role of defect states on electronic transport phenomena of charge carriers in nanostructured ZnO. Defect states in ZnO are created during its growth and can be controlled by changing the growth parameters such as temperature, pressure and molar concentration. We have used different types of nanostructured ZnO thin films for our investigations which are deposited on quartz, SiO₂/Si, sapphire and flexible polymer substrates. In order to achieve the reproducibility of the samples, the film deposition process must be done in a controlled manner. The growth parameters that should be controlled are molar ratio of reactants, pH of the solution and deposition temperature for chemical growth and pressure, time and annealing conditions for physical vapour growth. Our investigations such as photoresponse, carrier mobility, carrier concentration, carrier generation and recombination in nanostructured ZnO are carried out on polycrystalline and highly textured nanostructured ZnO that we have grown by chemical deposition and physical vapour deposition route. We have also described the new process for the decoration of plasmonic nanoparticles on the ZnO nanowire surface by pulsed laser ablation method. The characterization techniques, method of device fabrication and electronic and optoelectronic measurement techniques are also discussed in this chapter.

We have performed different characterizations on the samples to check the stoichiometry, growth direction, surface roughness etc. Ellipsometry has been used to measure the thickness of the film. The X-ray diffraction (XRD) analysis is done to check crystalline quality of the films. Energy dispersive analysis of x-ray (EDAX) is employed to determine the elemental composition of the material. The surface morphology and distribution of the grain size are investigated using scanning electron microscopy (SEM) and atomic force microscopy (AFM). Similarly, UV-Visible spectroscopy is utilized to find the optical band gap and photoluminescence (PL) spectroscopy is used to know the excitonic and defect

emission levels.

For our study, we have done electrical and optoelectronic measurements. In electrical measurements, we have performed room temperature IV-measurements, resistivity measurements, transistor characteristics (Transfer and output characteristic) etc. Hall effect measurement was done using cryogen free super conducting 10 T magnet with room temperature bore. We have automated data acquisition system using Keithley 2400 sourceMeter by interfacing it with a computer writing a C⁺⁺ code and LabVIEW software.

2.2 Preparation of nanostructured ZnO

Nanostructures of ZnO can be deposited or synthesized on different substrates such as glass, quartz, silicon. It can be also deposited on low temperature flexible polymer substrates. There are many nanostructure deposition techniques which are based on either purely physical or chemical process. In this thesis work we have employed both chemical and physical process for synthesis of nanostructured ZnO.

2.2.1 Chemical process

Chemical process is one of the important routes to grow nanostructured material in the field of nanotechnology. In this process material can be grown at low temperature with high throughput. There are many chemical methods for synthesis of the nanostructured ZnO such as sol-gel, hydrothermal, spray pyrolysis etc. [67–75]. In this thesis work, we have used the sol-gel spin coating and hydrothermal techniques to grow the nanostructured ZnO on quartz substrates.

2.2.1.1 Sol-gel spin coating

The sol-gel is the oldest technique for the film deposition. Nowadays, film deposition by this technique is used largely for diverse applications such as optical coatings, passivation layers, sensors, semicon-

ducting and superconducting films, and ferroelectrics. We have used the sol-gel spin coating technique (Figure 2.1) to grow the polycrystalline nanostructured ZnO film on quartz substrate. Zinc acetate dihydrate and propanol are used as a precursor and the solvent [76,77]. Diethanolamine (DEA) is used as sol stabilizing agent. It also reduces the surface tension and spreads the precursor uniformly throughout the substrate to make the film with uniform thickness. Spin coating process consists with some basic steps: [78]

(i) Precursor dispense on the substrate: In this step a few drops of fluid (precursor solution) are deposited onto the surface of the substrate. Two common methods for precursor dispensing are static and dynamic dispensing. In static method, precursor drops are cast on the substrate before spinning where as in dynamic method precursor is deposited while the substrate is spinning at low speed about 500 RPM. The advantage of dynamic method is that it reduces the voids in the films. The volume of the precursor deposited on the substrate depends on the viscosity of the fluid and the area of the substrate.

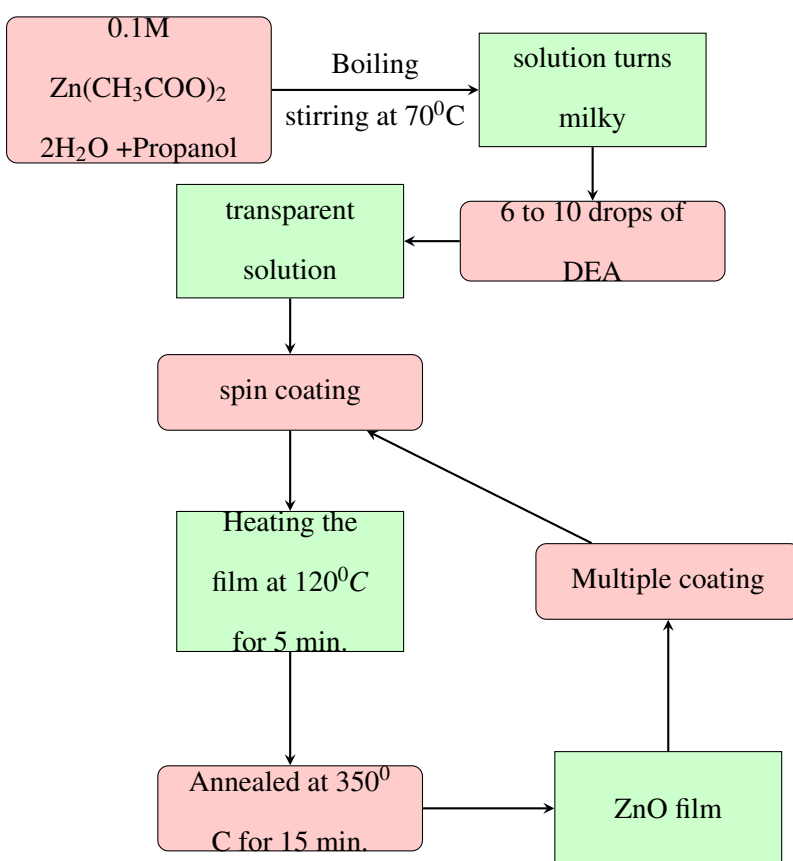
(ii) High speed spinning step: After dispensing the precursor on the substrate, the high speed spinning is required for thinning the fluid to make it a film of desired thickness. Most of the precursor solution is spread throughout the substrate due to centripetal acceleration. Typically the spinning speeds range from 1,500 - 6,000 RPM. This step takes 30 sec. to several minutes that depends upon the properties of the fluid and the substrates. The higher the spinning speed and longer time produce thinner films. Generally the combination of spin speed and time selected for this step defines the final thickness of the films.

(iii) Drying step: Sometimes drying step is also necessary to eliminate the excess solvent from the deposited film. After the high spin speed step, a moderate spin speed of about 25 % of high speed can be applied for drying the film without substantially thinning it. This process is fruitful for drying thick film since the long drying time may be required for such films.

After film deposition, it is required to bake the film to eliminate the water content and repeated the same deposition process several times to increase the film thickness. The flow chart shows the complete steps for the film growth by spin coating technique. Table 2.1 gives the process parameters used to deposit the thin film using sol gel spin coating technique.



Figure 2.1 Schematic diagram of spin coating technique.



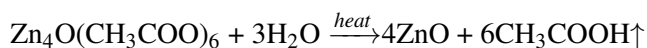
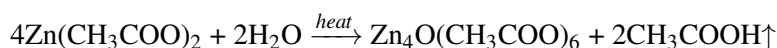
Flow chart of ZnO film preparation by sol-gel process.

In this thesis, polycrystalline nanostructured ZnO thin films are grown on fused quartz substrate by spin coating technique via acetate route. Zinc acetate dihydrate ($\text{Zn}(\text{CH}_3\text{COO})_2 \cdot 2\text{H}_2\text{O}$) and propanol are used as a precursor and solvent. Diethanolamine (DEA) is used as sol stabilizing agent. It also reduces the surface tension and spreads the precursor uniformly throughout the substrate to make film with uniform thickness. The basic steps for film growth is illustrated in flowcharts. The ZnO film is

Table 2.1 Deposition parameter used in sol-gel spin coating technique.

Deposition parameters	Values
Precursor concentration (M)	0.1
Spin speed (rpm)	3000
Time of coating (sec.)	45
Annealing temperature ($^{\circ}\text{C}$)	350 - 550

formed by the following chemical reaction



2.2.1.2 Hydrothermal method

Hydrothermal method is one of the oldest technology for crystal growth. Nowadays this method is covers several interdisciplinary branches of science for advance material processing. The term hydrothermal usually refers to a heterogeneous reaction in the presence of aqueous solution under high pressure and temperature. The nanostructured growth is performed in an apparatus consisting of a steel vessel called an Autoclave with Teflon beaker (Figure 2.2). The Autoclave must be capable of sustaining highly corrosive solvent at high temperature and pressure for a longer reaction time because in most of inorganic material synthesis, highly corrosive salts have been used.

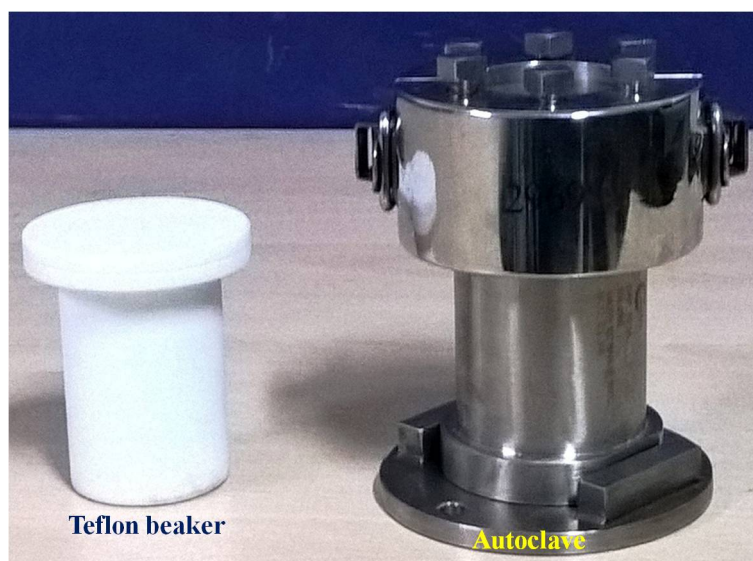
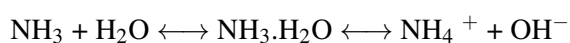
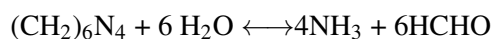


Figure 2.2 Image of Autoclave with Teflon beaker.

In this thesis work, the ZnO nanowire films are grown on seeded substrates using hydrothermal method. A thin layer of ZnO seed particles is grown on quartz substrate using sol-gel spin coating technique. The growth solution of ZnO nanowire is prepared by dissolving 0.01 M zinc nitrate hexahydrate and 0.01 M hexamethylenetetramine (HMTA) in deionized water. About 70% volume of Teflon beaker is filled with growth solution. The seeded substrates are kept inside the growth solution and sealed the Teflon beaker within the autoclave. Finally the autoclave was left to stand for 6 hrs. at 90⁰ C in the oven. After growth resultant samples are removed from the vessel and rinsed several times with deionized water to remove the residual reactant and dried it in the air at 125⁰ C. The ZnO nanowires are synthesized based on the following equation in hydrothermal process [79, 80].



In this reaction HMT is hydrolysed to form formaldehyde and ammonia which finally formed ammonium hydroxide and offer OH⁻ to give Zn(OH)₂. The growth of ZnO occurs by dehydration of these hydroxyl species at the surface of ZnO seed layer.

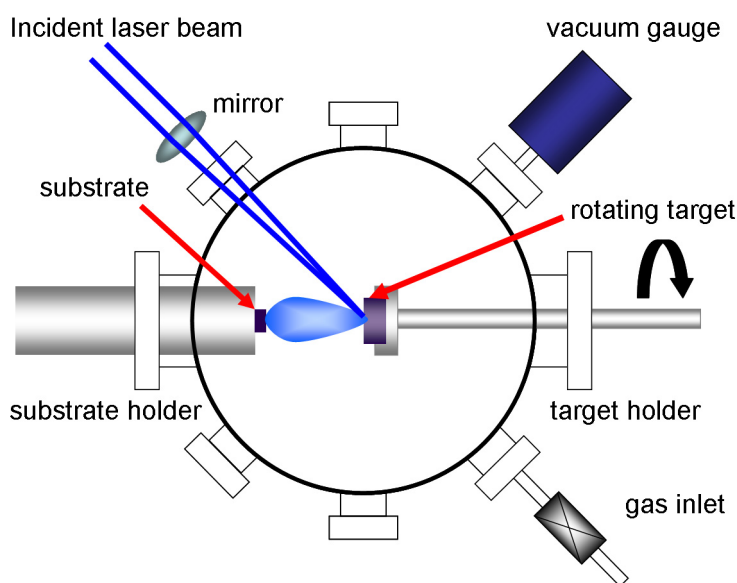


Figure 2.3 Schematic diagram for PLD setup. Wang et. al. ref. [81].

2.2.2 Physical process

This method covers a number of deposition techniques such as thermal evaporation, e- beam evaporation, pulsed laser deposition and sputtering. In this technique, material is released from a source and transferred to the substrate. This method provides material with better crystalline quality than the one obtained from a chemical process. We have used pulsed laser deposition technique to grow nanostructured ZnO films. We have used SiO₂/Si, Sapphire, flexible polymer (Kapton tape) as substrates to grow the films. The orientation and surface morphologies of the films depend upon the substrates used.

2.2.2.1 Pulsed laser deposition

PLD is one of the favourable method of ZnO thin film deposition on various substrates such as glass, quartz, Si, and sapphire. The excimer laser which is a combination of a noble gas (argon, krypton, xenon) and reactive gas (fluorine, chlorine) is used to deposit ZnO thin films in PLD method. The schematic of the PLD setup is shown in Figure 2.3. In this technique, high energetic laser pulses are used to melt, evaporate, excite and ionise the material from a single target of a complex material. These evaporated or ionized species from the target material form a gas plasma with a characteristic shape

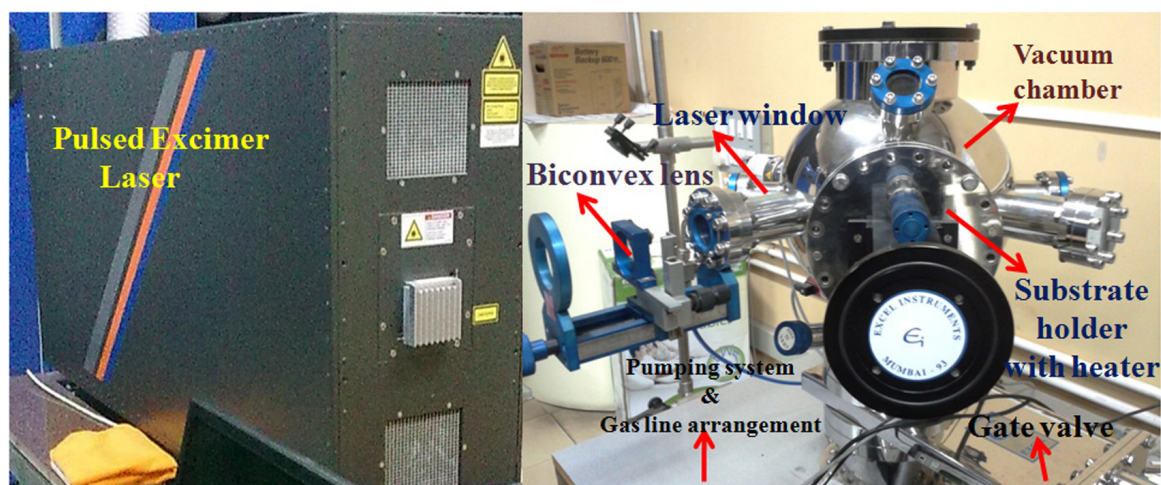


Figure 2.4 PLD setup in our lab. Courtesy: Ref. [82].

and colour known as plasma "plume". The plasma plume expands and reaches the substrate which is placed in front of the target material at a suitable distance and deposit the material as a thin film. This process is carried out in high vacuum or in the presence of background gas such as oxygen or a mixture of argon and oxygen gases. The deposition rate can control the crystalline quality, surface morphology and composition of the deposited film. In addition to deposition rate the film quality also depends on the pulse energy, ambient gas pressure, the repetition rate and target to substrate distance. The film growth by PLD method occurs in three stages.

1. The interaction between the laser pulses and the target which leads to melting the target material. This melted surface of the target gets vaporized and gives a highly forward directed plasma plume.
2. The forward directed plasma plume interacts with the ambient gas (both physically and chemically).
3. Finally the ablated material condense onto a given substrate where the thin film is nucleated and growth takes place.

In our lab we have used KrF of wavelength $\lambda = 248$ nm for the deposition of ZnO film. The PLD set up in our lab is shown in Figure 2.4. We have deposited the nanostructured ZnO film under $\sim 10^{-5}$ mb base pressure and different oxygen pressure 10^{-2} to 10^{-3} mb. The laser fluence and pulses are optimized for the deposition of ZnO films. We have used the laser fluence $1-1.5$ J/cm² and 3,000-6,000 shots. In this work, we have made ZnO target using commercially available ZnO powder. The powder is

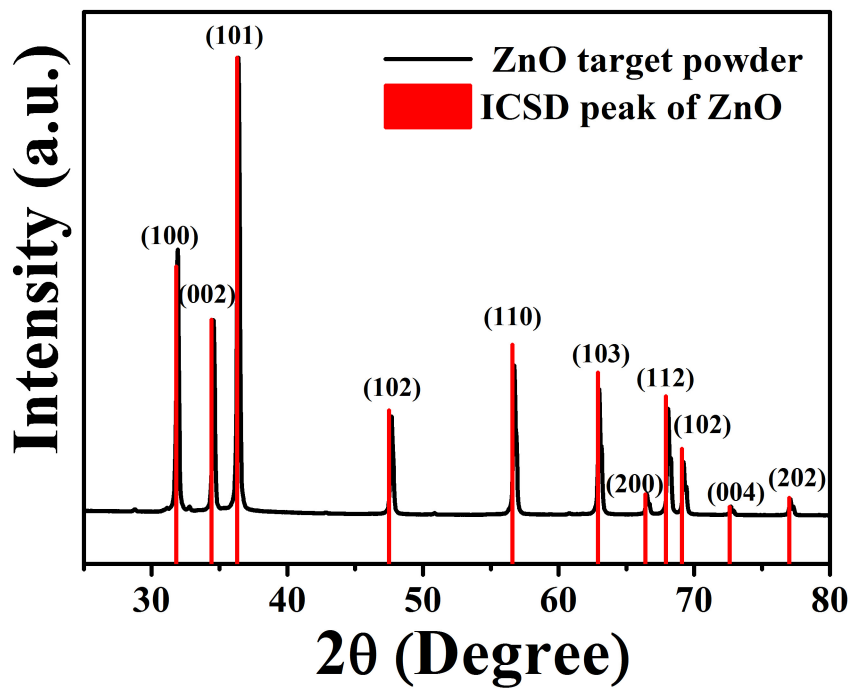


Figure 2.5 XRD pattern of ZnO target.

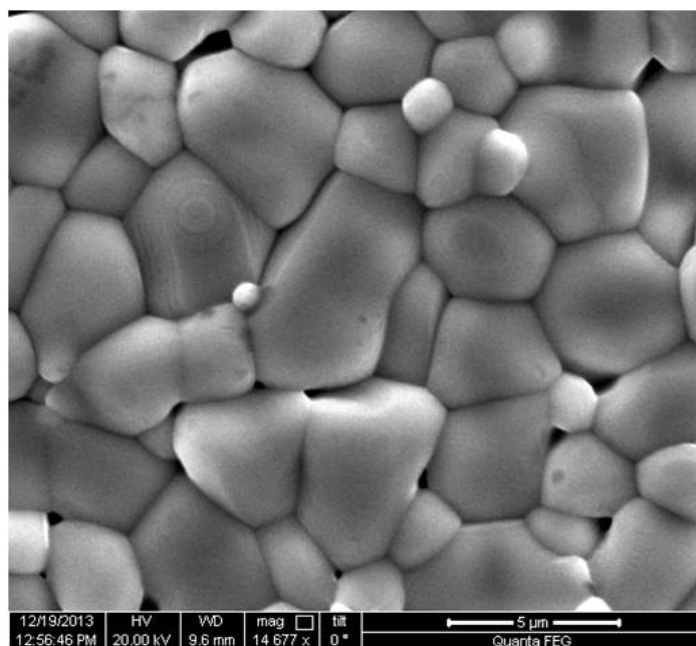


Figure 2.6 SEM image of target pellet of ZnO.

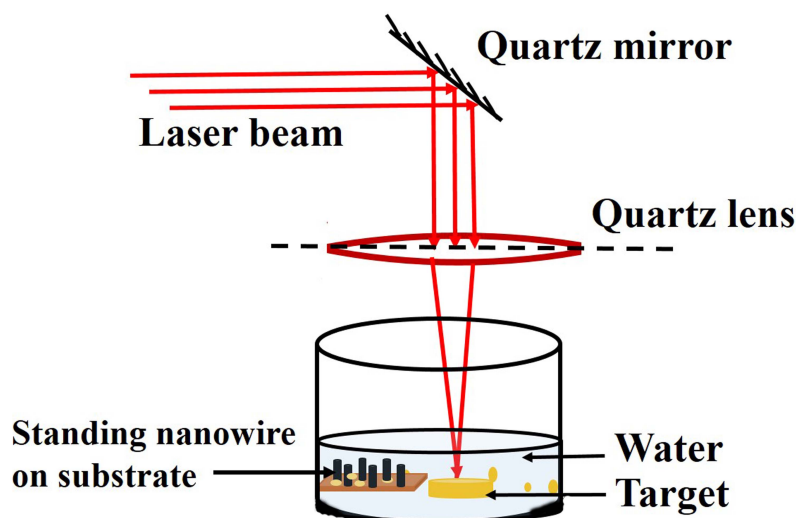


Figure 2.7 Experimental setup for plasmonic nanoparticle decoration on nanowire surface using laser ablation.

grinded and pelletized using a pelletizer under high pressure (about 100 MPa). As grown pellet is not compact therefore we heated the pellet in a furnace at temperature 1300°C under constant oxygen flow to get compact and large grain size. To conform the structure of ZnO we have characterized the pellet using XRD. Figure 2.5 shows the XRD pattern matches well with the ICSD peaks of ZnO. The surface morphology of the target pellet is studied using SEM imaging (Figure 2.6) which consists of large and compact grain size.

2.2.2.2 Decoration of Plasmonic Au nanoparticles on ZnO nanowire surface using laser ablation in liquid medium

In this thesis work, we have applied the novel technique to decorate the ZnO nanowire surface by plasmonic Au NPs using a laser ablation method in liquid medium. This is a process that needs no vacuum and the experimental setup for this experiment is shown in Figure 2.7. The Au target and the nanowire film on the substrate are placed inside the water. Laser beam from KrF excimer Laser ($\lambda \approx 248\text{nm}$) reflected from a 45° degree inclined mirror are focused on the metal target by a quartz lens. The ablated nanoparticles remain suspended in the water medium or get coated on the substrate. The surface of the

nanowire acts as a nucleation centre and helps the nanoparticle to grow throughout the surface of the nanowire [83]. For enhancing the performance of the ZnO, the ligand free method is an extremely desirable feature because presence of any ligand that binds Au nanoparticles to ZnO also acts as a barrier to charge transport. The concentration of the Au NPs attached on the nanowire surface can be controlled by varying the number of laser pulses which we will discuss in chapter 6. This method leads to uniform coverage of ZnO-NW's by Au NPs.

2.3 Characterization

After synthesis the nanostructured materials we have to analyse the material characteristics such as crystal structure, surface morphology and optical properties.

2.3.1 Structural characterization

The structural characterization is used to investigate the crystal quality, growth direction, thickness measurement, surface morphology etc., of the nanostructured ZnO. We have used the following techniques for structural and morphological characterization.

(1) X- ray diffraction, (2) Scanning electron microscopy (3) Atomic force microscopy

2.3.1.1 X-ray diffraction

X-ray diffraction is relevant method in determination of crystallinity of the materials. In our experiments XRD spectra were recorded using PANalytical X-PERT PRO diffractometer. The wavelength of the X-rays used is 1.54 Å corresponding to the Cu-K α source. Figure 2.8 shows the XRD patterns of nanostructured ZnO films grown on quartz substrates using sol-gel spin coating technique at different annealing temperatures (350⁰ C, 450⁰ C and 550⁰ C). Conversion of the one of the important parameters of the XRD can be calculated is the full width of half maximum (FWHM) which gives the information about the material's quality. A high value of FWHM describes a diffraction peak that is

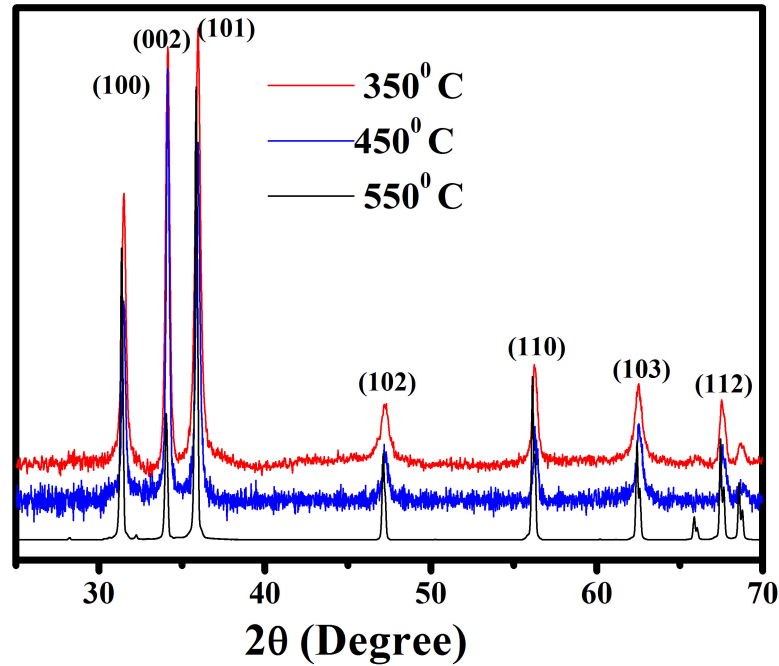


Figure 2.8 XRD pattern of nanostructured ZnO film grown using sol-gel spin coating technique on quartz substrate at different annealing temperature (350⁰ C to 550⁰ C).

wide and broad, which indicates small crystallite size in nanostructured materials. We have used the the Williamson Hall analysis to calculate the grain size (D) as follows: [84].

$$\frac{\beta \cos \theta}{\lambda} = \frac{1}{D} + 2\varepsilon \frac{\sin \theta}{\lambda} \quad (2.1)$$

Where λ is the X- ray wavelength, β is the full width of half maximum (in radian). ε is the strain. The intercepts of the Williamson Hall plots (Figure 2.9 (a)-(c)) at different temperatures give the grain size of the the nanostructured films. The table 2.2 show the variation of grain size with increasing the annealing temperature.

2.3.1.2 Scanning electron microscopy

A topographical image and cross section of the ZnO surface are taken with a scanning electron microscope (SEM). We have used SEM for imaging the grain size and surface morphology (concentration of grains, voids and compactness) of the nanostructured ZnO film (Figure 2.10). The cross-sectional

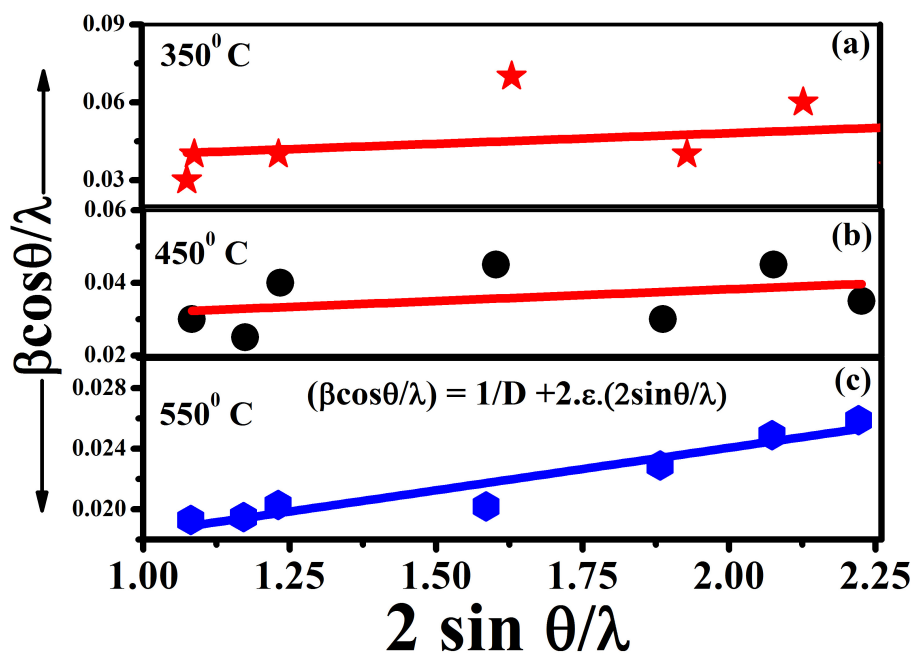


Figure 2.9 Williamson Hall analysis of nanostructured ZnO films annealed at (a) 350°C (b) 450°C and (c) 550°C).

Table 2.2 Grain size study using XRD pattern.

Annealing temperature (°C)	average grain size (nm)
350	~30
450	~40
550	~90

SEM imaging is also utilized to determine the thickness of the films (inset in Figure 2.10).

2.3.1.3 Atomic force microscope

AFM is used to detect the surface topography of a sample from sub micron to atomic scale. Unlike optical microscope and SEM, the imaging of AFM is done by dragging a sharp tip, which is made of Si or SiN mounted on a cantilever. As the tip approaches the surface of the sample, the force between

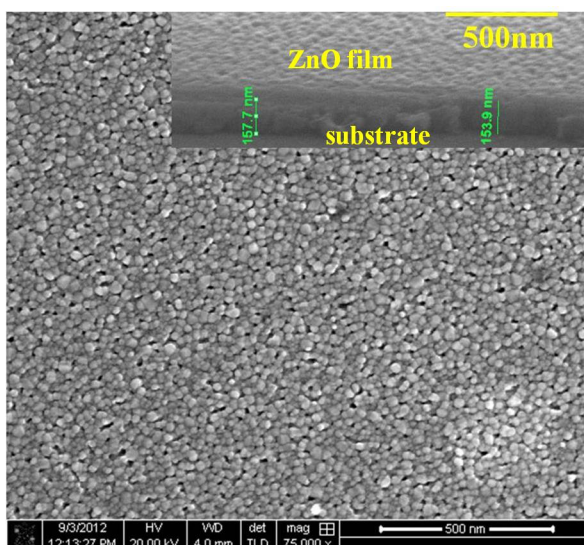


Figure 2.10 SEM image of nanostructured ZnO film. Inset shows the cross-sectional view of the film.

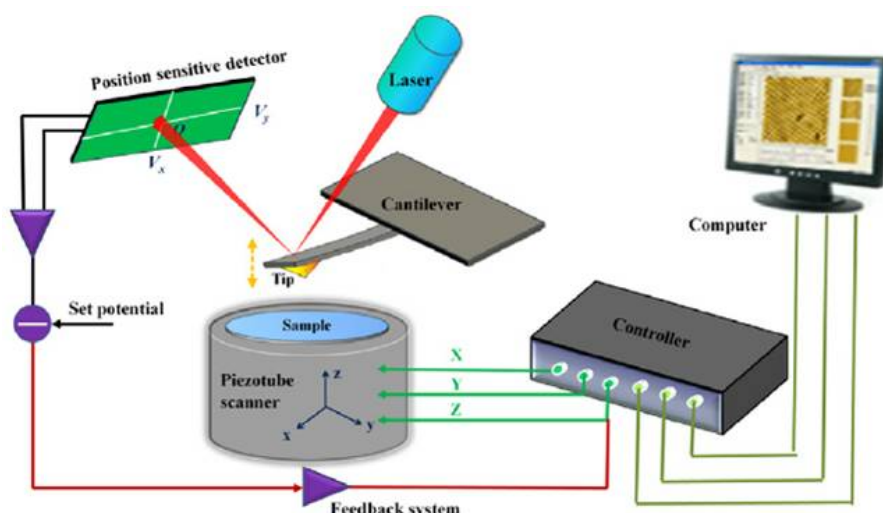


Figure 2.11 Schematic diagram of the AFM measurement procedure. Courtesy: Ref. [85].

the tip and the sample lead to deflection of cantilever according to Hooks law. The deflection of the cantilever is measured using the laser spot reflected from the top of the cantilever. The AFM can be operated in three modes: Contact, non- contact and tapping mode. In the contact mode operation, the force between the tip and the surface is kept constant during scanning by maintaining a constant deflection. However, in non-contact mode, the tip oscillates at the resonance frequency and the amplitude of

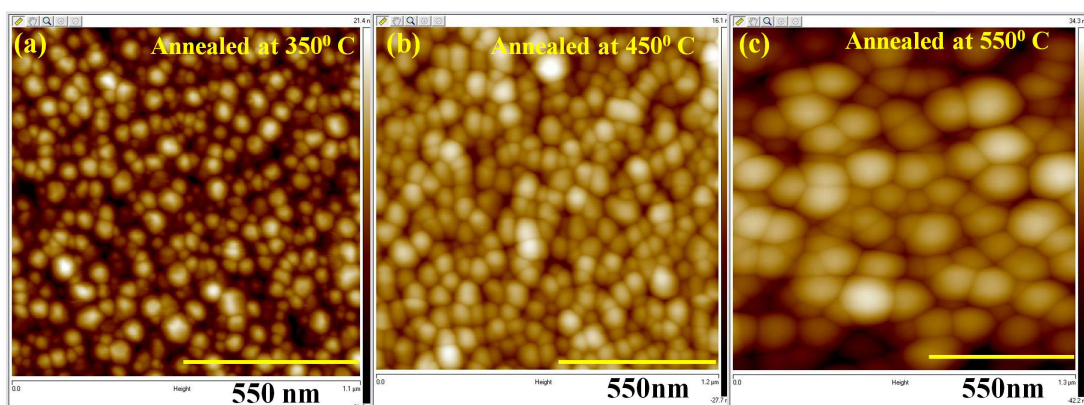


Figure 2.12 AFM images of nanostructured ZnO film grown in different annealing temperature. Color code representing the height variation on the surface.

the oscillation is kept constant. In tapping mode, frictional force is eliminated by contacting the surface and oscillating with sufficient amplitude to prevent the tip from being trapped by adhesive meniscus forces from the contaminant layer. Figure 2.11 represents the schematic diagram of AFM measurement procedure.

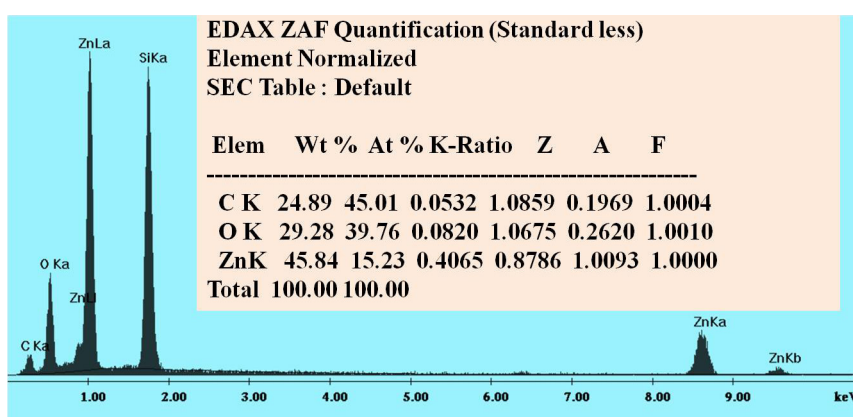
We have used the contact mode and lateral mode operation for imaging the nanostructured ZnO films grown in different substrates. We have extracted the particle size distribution, average roughness and also confirmed the compactness of the grains from AFM images of the samples. Figure 2.12 shows the AFM image of nanostructured films in different annealing temperature. At low annealing temperature, the average grain size as well as the surface roughness is smaller whereas with increasing the annealing temperature the average grain size as well as surface roughness increase. Table 2.3 shows the detail information of nanostructured ZnO films. The average grain size calculated from xrd pattern and AFM imaging are consistent with each other.

2.3.1.4 Energy dispersive X-ray analysis

Energy-dispersive X-ray analysis (EDAX) is an analytic technique used for determining the elemental composition of the material. In this process electron beam is incident on the sample surface which

Table 2.3 Surface and grain size study using AFM imaging

Annealing temperature ($^{\circ}\text{C}$)	Average grain size(nm)	Surface roughness(nm)
350	~25	~ 8
450	~45	~5
550	~100	~3

**Figure 2.13** EDAX data of nanostructured ZnO film

excite and ejecting electron from in the inner shell that creating electron holes. An electron from outer high energy shell fills the hole and the energy difference between higher energy shell and lower energy shell produces the characteristics X- ray of that material. The number and energy of these characteristic x-ray can be measured by energy dispersive spectrometer, which gives the percentage elemental composition of the material.

In this thesis work, EDAX is done to determine the elemental composition of the nanostructured ZnO. Figure 2.13 shows the EDAX data that show the composition elements zinc and oxygen without any other impurities.

2.3.2 Optical characterization

Optical characterization is non-contact and non-invasive method to analyse the optical properties of nanostructured materials. We have utilized ellipsometry to determine the film thickness and UV-visible

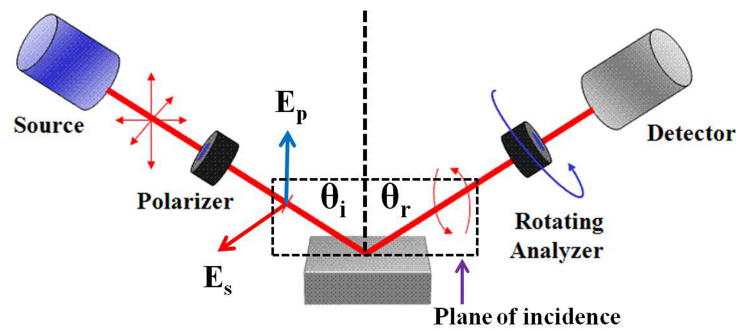


Figure 2.14 Schematic diagram of spectroscopic ellipsometry. Courtesy: Ref. [86]

spectroscopy to determine the optical band gap of nanostructured ZnO. The photoluminescence spectroscopy was utilized to investigate the excitonic emission and defect emission in ZnO.

2.3.2.1 Thickness measurement by ellipsometry

Ellipsometry is a non destructive optical analysis technique to measure the thickness and optical constants (refractive index, extinction coefficient) of the material in the form of thin film. The schematic diagram of ellipsometry is shown in Figure 2.14. This method does not directly measure the film thickness and optical constants. Figure 2.15 shows the generated and experimental spectroscopic ellipsometry data of nanostructured ZnO films grown on quartz substrate using sol-gel spin coating technique. Ellipsometry based on the fact that the light undergoes some change in polarization when it is reflected from the surface of the sample. The change in polarization of light gives the characteristic of the surface structure of the material. The change in polarization is represented by ψ and Δ in degree which are differential changes in amplitude and phase respectively. These parameters are utilized to determine the film thickness and refractive index of the material. This is done by numerically inverting the thin film interference equation shown below

$$\frac{R_p}{R_s} = \tan \psi e^{i\Delta} = \frac{\frac{r_{p01} + r_{p12} e^{-i2\beta}}{1 + r_{p01} r_{p12} e^{-i2\beta}}}{\frac{r_{s01} + r_{s12} e^{-i2\beta}}{1 + r_{s01} r_{s12} e^{-i2\beta}}} \quad (2.2)$$

where R_p and R_s are the Fresnel reflection coefficients for p (in which electric field vector is in the plane of incidence) and s (in which electric field vector is perpendicular to the plane of incidence). The

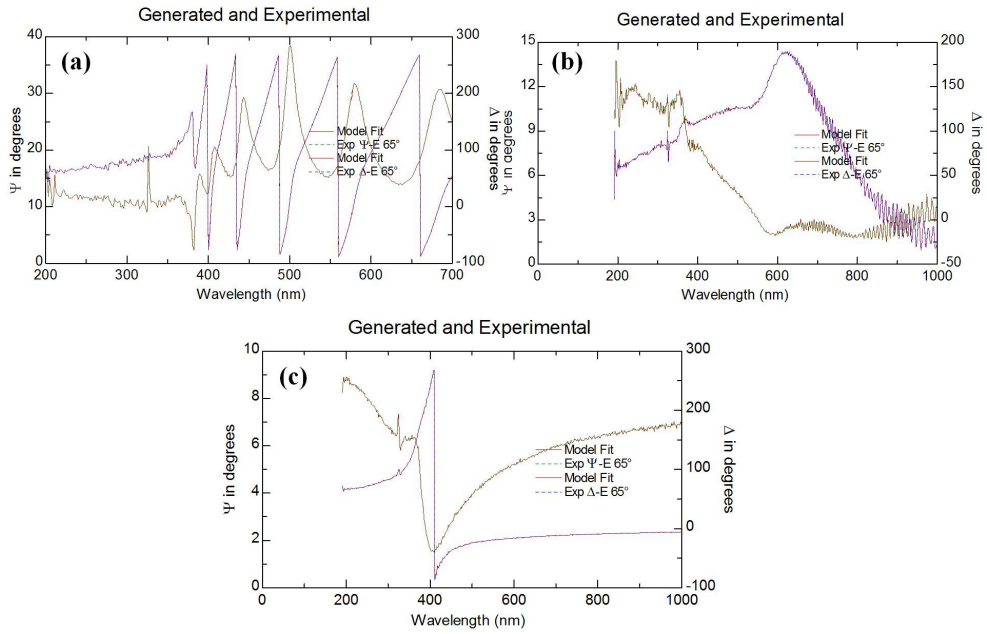


Figure 2.15 Ellipsometry data of ZnO thin film grown on (a) SiO₂/Si (b) polyamide Kapton tape and (c) Al₂O₃.

reflection coefficients $r_{p,s}$ at each interference and the film phase factor β are calculated using refractive index and angle of incidence. Figure 2.15 shows the generated and experimental ellipsometry data for ZnO film grown on different substrates (SiO₂/Si, polyamide Kapton tape and Al₂O₃). Table 2.4 illustrates the thickness of ZnO films.

Table 2.4 Thickness estimated from ellipsometry measurement

Sample	Thickness (nm)
ZnO on SiO ₂ /Si	~140
ZnO on polyamide Kapton tape	~100
ZnO on Al ₂ O ₃	~40

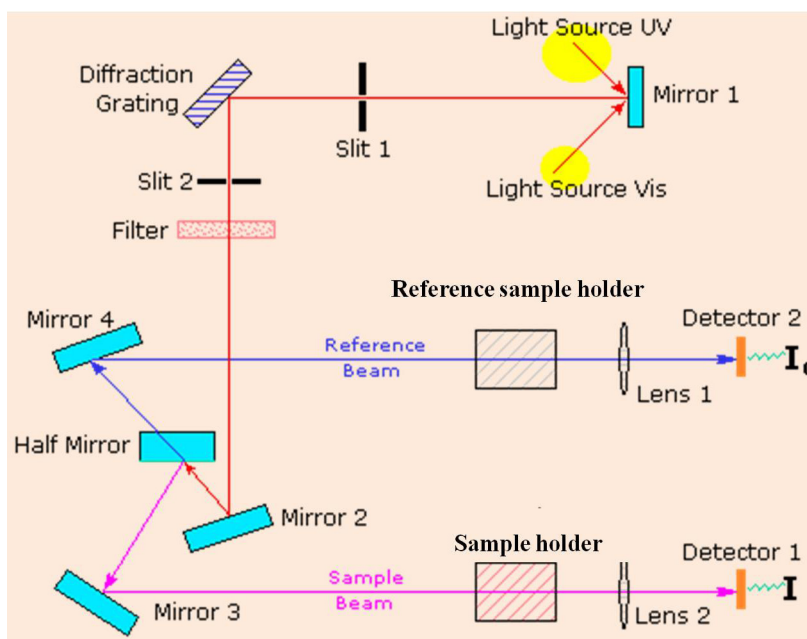


Figure 2.16 Schematic diagram of UV-Visible spectroscopy [87].

2.3.2.2 UV-Visible spectroscopy

UV-Visible spectroscopy is one of the oldest and useful technique to determine the absorption of light through the liquid or solid sample. The principle of UV-visible spectroscopy is based on electronic transition from a lower energy state to a higher energy state. In a wide band gap semiconductor like ZnO the primary source of absorption occurs at band gap.

Figure 2.16 shows the typical diagram for UV-Visible measurement. A beam of light (red coloured) from UV-Visible source splits into different wavelength by diffraction grating. Then each monochromatic beam splits into two equal intensity beam by half mirrored device. One of the beams which goes to sample named as sample beam (coloured magenta) with an intensity of I and other beam which goes to reference sample named as reference beam (coloured blue) with intensity I_0 are incident on the the sample and a reference sample. The intensities of these light passes through the sample and reference sample are measured by electronic detectors and compared. The scan range of UV- Visible spectroscopy is usually 200 - 800 nm. The absorbance of the sample is plotted as

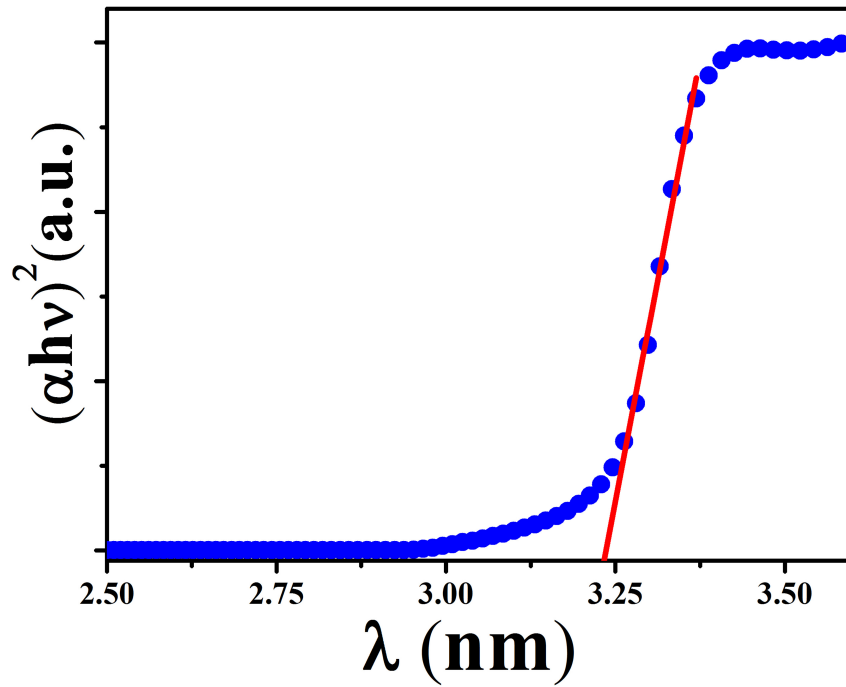


Figure 2.17 Tauc plot from UV-Visible analysis of ZnO thin film to determine the optical band gap.

$$A = \log\left(\frac{I}{I_0}\right) \quad (2.3)$$

If there is no absorption, $A = 0$. The wavelength corresponding to the maximum absorbance is characteristic wavelength and named as λ_{max} which lies on band gap edge in semiconductor samples.

The absorption coefficient α is calculated using Beer's law,

$$I = I_0 e^{-\alpha d} \quad (2.4)$$

$$\ln\left(\frac{I_0}{I}\right) = \alpha d \quad (2.5)$$

$$\alpha = 2.303A/d \quad (2.6)$$

Where d is film thickness. In this thesis, the optical band gap of nanostructured ZnO is calculated using Tauc plot of absorption data plotted with respect to energy. The optical absorption strength depends on the difference between photon energy and optical band gap as follows

$$\alpha h\nu = k(h\nu - E_g)^n \quad (2.7)$$

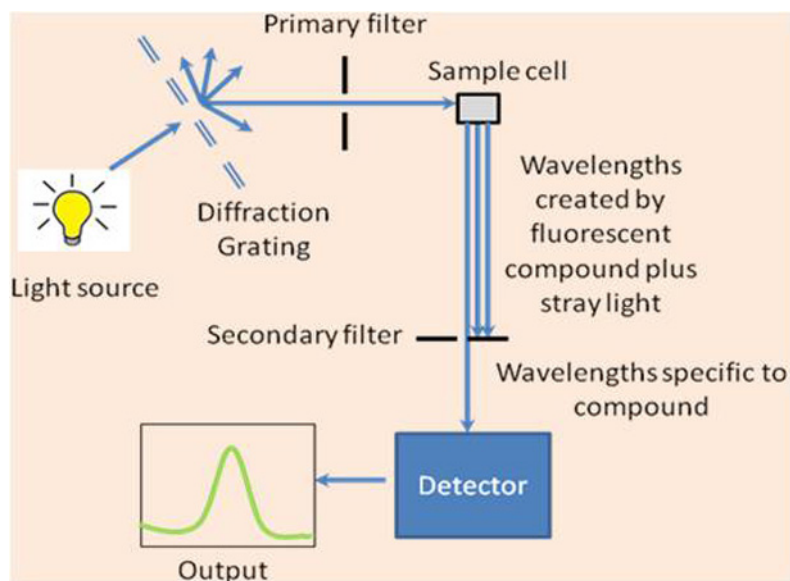


Figure 2.18 Schematic of Fluorometer. Courtesy: Ref. [88]

where h = Planck constant, ν photon's frequency, α is the absorption coefficient, E_g is band gap and k = is a proportionality constant. The value of n is $1/2$ for direct band gap semiconductor.

Figure 2.17 shows the Tauc plot of nanostructured ZnO film. At low photon energy, the absorption is almost zero i.e. transparent region. The value of the intercept due to the extrapolation of this linear region gives the band gap $E_g = 3.23$ eV (Figure 2.17) from the nanostructured ZnO film.

2.3.2.3 Photoluminescence measurement

Photoluminescence measurement is a contactless, non destructive method to probe the electronic structure of the material. In this experiment a beam of light corresponding to the band gap energy, or more than this is allowed to interact with the sample which absorbs and excites the electrons from the valence band to the conduction band leaving behind equal numbers of holes in the valence band. These excited electrons no longer stay in conduction, eventually they recombine with photo generated holes. The electron-hole recombination gives the emission. The intensity and spectral content of this emission gives the material properties such as band gap level and impurities or defect levels. This technique

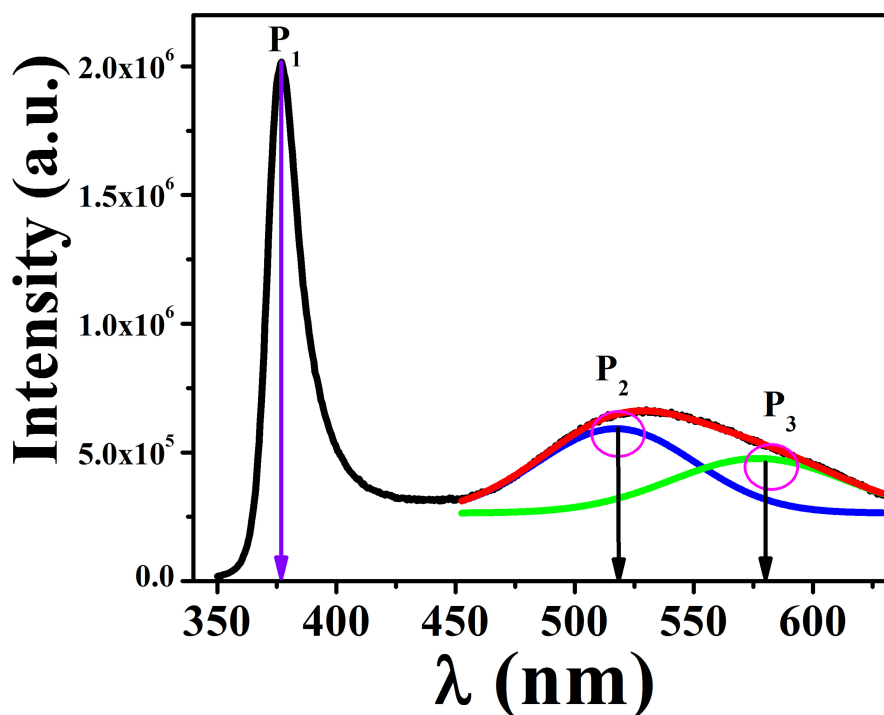


Figure 2.19 PL spectra of ZnO nanowire film.

has the highest potential to identify the extremely low concentration of intentionally or unintentionally created defect states which strongly affect material quality.

The working schematic of the PL measurement is shown in Figure 2.18. The excitation wavelength is provided by the light source (xenon lamp in our lab) over the ultraviolet and visible range. The diffraction grating split the incident light into its components. The monochromator adjusted here choose the wavelengths to pass through. Following the primary filter, specific wavelengths of light are irradiated onto the sample. Secondary filter is placed at 90° angle to the original path of incident light to avoid reaching the excited radiation to the detector.

Figure 2.19 shows the PL spectra of nanowire film. PL spectrum of ZnO nanoparticles and nanowires have been extensively studied in our laboratory. The spectra reveal three different peaks P_1 , P_2 and P_3 corresponding to different wavelengths. Peaks P_1 lies in UV region around 380 nm corresponding to the exciton emission which is the fundamental near band edge emission. The other peaks P_2 and P_3 lying in the visible region at 520 nm and 580 nm arises from the defect levels in ZnO nanowire films

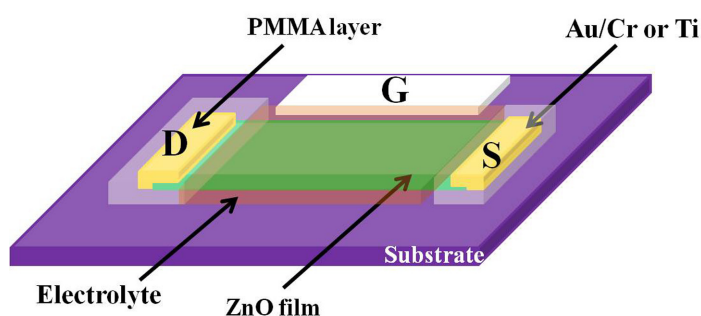


Figure 2.20 Schematic diagram of field effect device in side gate configuration and ohmic contact.

related to oxygen vacancy.

2.4 Device fabrication and measurements

In this thesis work we have fabricated the devices based on ZnO nanostructured films. These are two terminals and three terminal field effect devices depending upon the nature of the measurements. For field effect device the source, drain and gate electrodes are made by the thermal evaporation of the Au/Cr using the hard mask. The polymer electrolyte which is used as a gate insulator is prepared by mixing the polyethylene oxide (PEO) and Lithium per chlorate (LiClO_4) in 10:1 ration. The mixture of a PEO and LiClO_4 is dissolved in methanol by constant stirring and evaporation till the solution becomes a gel. This gel is employed on the exposed area of the channel as a top and side gate gate. The source and drain are covered with a thick layer of polymethyl methacrylate (PMMA) to prevent the gate dielectric for touching the source drain contacts. For Hall measurement, the device is configured in Hall bar geometry which is shown in chapter 5. Figure 2.20 shows the schematic diagram of side gate configuration of field effect device.

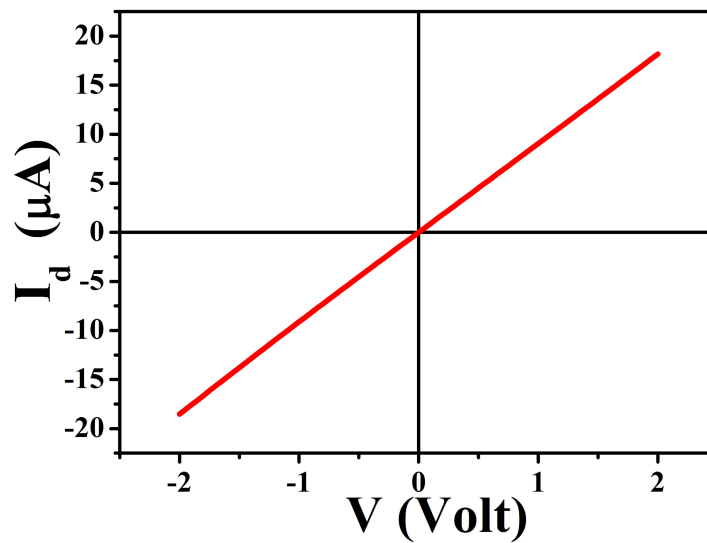


Figure 2.21 Current voltage characteristic in ohmic contact.

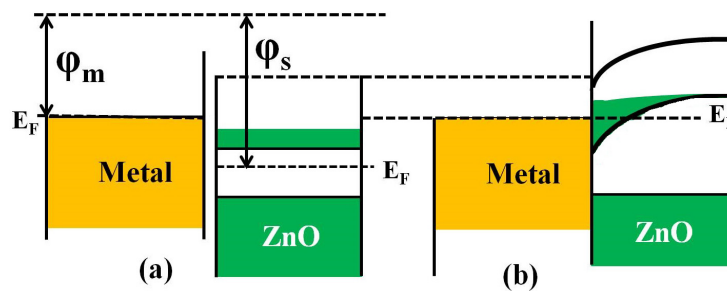


Figure 2.22 Schematic diagram of band structure of metal and ZnO (a) before contact made (b) after contact made.

2.4.1 Ohmic contact

In our case the contact made by thermal evaporation of Au/Cr on the ZnO nanostructured film shows the ohmic behaviour (Figure 2.21). A metal semiconductor junction becomes an ohmic contact if the barrier height is zero at the interface. In this case carriers are free to move in and out of the semiconducting channel with negligible resistance across the contact. The band diagram for the ohmic contact formed in nanostructured ZnO is shown in Figure 2.22. The diffusion of the electrons after making the Au/Cr contacts allows the band bending of ZnO downward and no barrier is formed to restrict the flow of electron in either direction. The current increases linearly with voltage and is symmetric about the

origin according to the Ohm's law.

2.4.2 Electronic and optoelectronic measurements

Electronic and optoelectronic measurement are useful technique for both fundamental and application level investigations of metals, semiconductors and insulators. Electronic measurements give the information about carrier transport phenomena in nanostructured materials. The resistivity, carrier mobility, carrier concentration, etc., can be determined using electronic measurement technique. The optoelectronic measurement technique consists of the interaction of light with material which gives the information about the transport properties of photo generated charge carriers and carrier recombination process. In this thesis work we have done the following measurements.

- (1) Current voltage (I-V) using Vender paw measurements
- (2) Thin film transistor (3 terminal) measurements
- (3) Photoconductivity measurements with and without gate
- (4) Hall effect measurement with and without gate
- (5) A. C. Impedance measurement with and without gate

Here, we have described some of these and more detail are in relevant section.

2.4.3 Current voltage (I-V) measurement and four point resistivity measurement

The electrical measurements are carried out at room temperature using souce meters. We have done the current, voltage measurement (I-V) to conform the ohmic behaviour of the source drain contacts. In this thesis, the Van Der Pauw method is used to determine the resistivity of the chemically grown nanostructured ZnO film. For this measurement four ohmic contacts using Cr/Au pads are made at the corner of the square shaped sample as shown in Figure 2.23. The contacts are very small and place closed to the boundary of sample as possible. In van der Pauw resistivity measurements, the current is measured on adjacent nodes and the voltage is measured on opposing adjacent nodes (Figure 2.23).

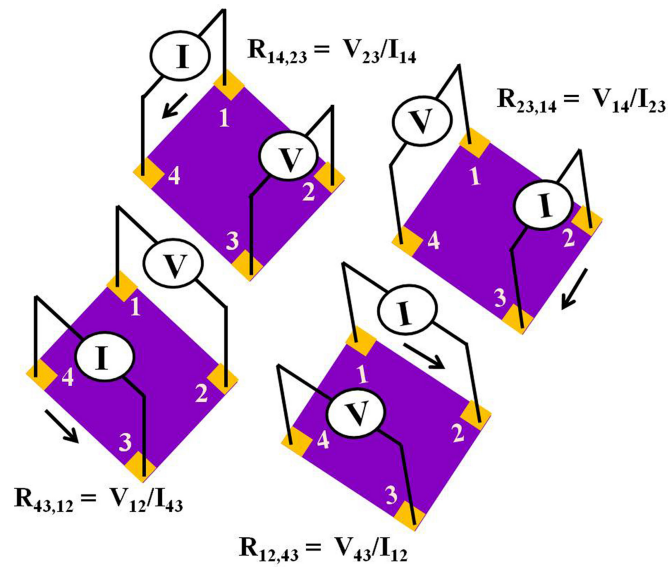


Figure 2.23 Van der Pauw resistance measurement configurations.

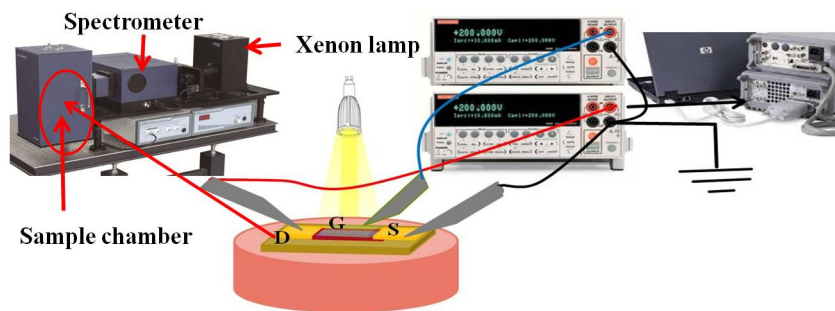


Figure 2.24 Measurement set of for transistor characteristics and photoconductivity measurements.

The sheet resistance of the nanostructured ZnO channel was calculated using the formula listed below:

$$\exp\left(\frac{-\pi R_A}{R_s}\right) + \exp\left(\frac{-\pi R_B}{R_s}\right) = 1 \quad (2.8)$$

Where $R_A = \frac{R_{21,34} + R_{12,43} + R_{43,12} + R_{34,21}}{4}$, $R_B = \frac{R_{32,41} + R_{23,14} + R_{14,23} + R_{41,32}}{4}$ and R_s is the sheet resistance of the nanostructured ZnO film. The resistivity (ρ) of the film was calculated using the relation:

$$\rho = R_s \cdot t \quad (2.9)$$

where t is film thickness.

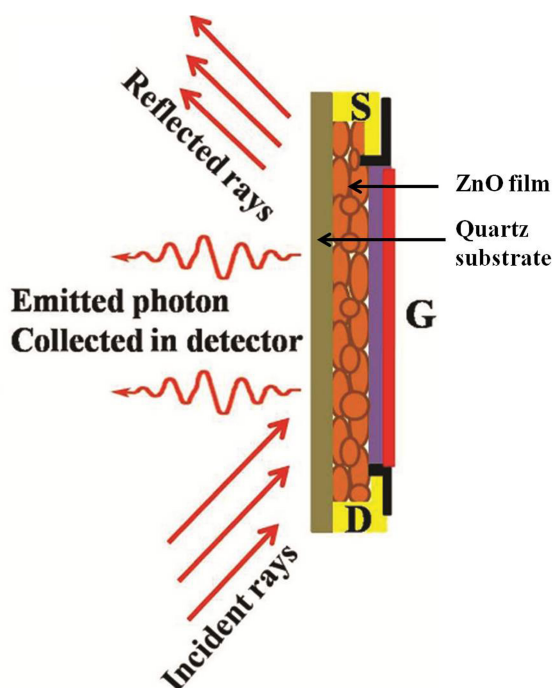


Figure 2.25 Schematic of gate dependent PL measurement.

2.4.4 Thin film transistor characteristics and photoconductivity measurements

The transistor characteristics such as transfer characteristic, output characteristic and transient gate response are measured using Keithley 2400 sourceMeter. The measurement setup is shown in Figure 2.24 where the source meter is connected to the computer using general purpose interface bus (GPIB) cable. Data Acquisition process is done using C⁺⁺ code (In some cases LabVIEW program is also used). We have used xenon lamp attached with a spectrometer and monochromator for photo conductivity measurements (Figure 2.24). The transient photocurrent and the spectral response of the photo detector are measured under different power and wavelengths. The power of the light source is measured by a calibrated power meter kept at the same location as the sample. The time of response of the gate current I_g and the drain current I_d as a result of the step change in the gate bias V_g are also measured by digitizing both the currents to establish the gate charging characteristics.

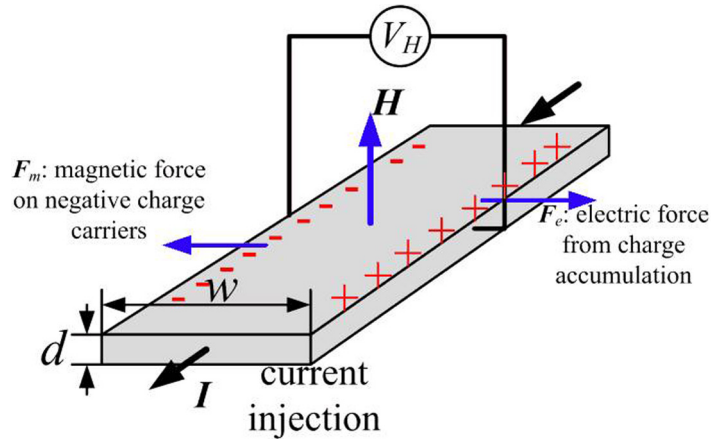


Figure 2.26 Hall effect measurement. Courtesy: Ref. [89]

2.4.5 Gate bias dependent photoluminescence measurement

We have measured the photoluminescence spectra with applied gate bias in the configuration as shown in Figure 2.25. The PL spectra are measured by spectrofluorometer equipped with a xenon arc lamp and double monochromator. The excitation wavelength applied for the PL measurement is 340 nm.

2.4.6 Hall effect measurement

The basic physics behind the Hall effect is the Lorentz force. When the magnetic field B is applied perpendicular to the current flow in the bar-shaped specimen as shown in Figure 2.26, it experiences a Lorentz force which causes the deflection of current. The opposite charge carriers are accumulated at two edges of the specimen creating a Hall field E_H . When the magnetic force F_m is equal to the electric force F_e created by Hall electric field an equilibrium state is achieved. In this case,

$$F_m = F_e \Leftrightarrow qv \times B = \frac{V_H q}{w} \quad (2.10)$$

where V_H is Hall voltage created by the electric field of accumulated charge carriers and w is the width of the specimen. The Hall voltage is V_H is expressed in terms of applied magnetic field and the constant



Figure 2.27 Cryogen free 10 T magnet. Courtesy: Ref. [82]

current I flowing through the specimen as

$$V_H = \frac{IB}{nqd} \quad (2.11)$$

In this thesis work we have determined the Hall mobility, carrier concentration and sheet resistance of the nanostructured ZnO film. We have used the cryogen free 10 T superconducting magnet (Figure 2.27) with room temperature bore.

Chapter 3

Large enhancement of ultraviolet photoresponse in nanostructured ZnO film using electric double layer gate dielectric

Photoresponse behaviour of a nanostructured material is greatly influenced by the defect states which commonly lie within the grain boundary regions. The large enhancement of photoresponse in a nanostructured ZnO film is observed using an electrolyte as a gate dielectric with gate bias and UV illumination. The resultant current enhancement by the combined effect of two effects (field effect and illumination) is much larger than the simple addition of two effects when they act individually. The electrolyte, used as a gate dielectric, forms an electric double layer at the interface between the nanostructured film and the gate dielectric. The field effect mobility of the carrier is enhanced in presence of UV illumination due to a reduction of the grain boundary barrier ϕ_{GB} that forms in the grain boundary region between the nano crystallites because of large surface charge induced by field effect. It is proposed that the field induced carriers passivate the charged defect states in the ZnO particularly at the

depleted GB thereby reducing carrier scattering and enhancing the mobility and thus the photocurrent. The mechanism proposed has been validated by observation of gate controlled Photoluminescence, where the passivation of charged defect states by gate induced carriers lead to suppression of visible Photoluminescence, which arises from charged oxygen vacancy defect states.

3.1 Introduction

In this section, we discuss the advantages of using electric double layer (EDL) gate dielectric on nanostructured ZnO films in photo detection. Our aim is to present a detail description of the enhanced photoresponse of nanostructured ZnO films in a field effect device configuration. In recent years, the researches on such field effect based devices have undergone a change, where conventional oxide based gate dielectrics have been replaced by an electric double layer (EDL) as the dielectrics, which can induce very large surface charges [23, 24, 40, 43]. This is particularly more relevant when nanostructured materials are used as channels in such field effect (FE) devices, where the control of charges at the grain boundary (GB) region (interface between two crystallites) can lead to substantial control of the charge transport in the semiconductor channel. An interesting recent development is the observation of the enhancement of UV photoresponse in epitaxial ZnO film, [90] where the FE device has been used as a photodetector. Field effect devices based on ZnO films with conventional oxide gate dielectrics have been reported before [53, 54, 91–94].

In this thesis work, we show that the use of EDL as a gate dielectric can lead to a large enhancement of photoresponse of a nanostructured ZnO film at low gate bias and low illumination power density. The synergetic photoresponse is brought about by reduction of barriers at grain boundaries and passivation of charged defect states in the nanostructured channel. We showed that this happens because of the carriers induced by the gate can also enhance the mobility substantially by passivating the charged defects. This leads to a large enhancement in device current and its photoresponse. We also tested this proposed hypothesis by simultaneous measurement of photoluminescence (PL) from the ZnO film on application of a gate bias. The gate bias by controlling the occupation of the defect states, also modulates the defect induced visible PL. This phenomenon, though shown in the context of the ZnO film, have a general validity and can also occur on other oxide photodetectors which giving rise to a broad application potential.

In a nanostructured ZnO films, as used in this section, the GB region between two nanocrystallites plays an important role to limit and control the electrical transport in such films [20, 42, 53, 95, 96]. The

GB regions due to predominance of the defect states are depletion regions. The transport through GB is governed by a barrier ϕ_{GB} and the depletion length w . Thus, any agents that control ϕ_{GB} and w can effectively control the transport (and also the photocurrent) in such nanostructured films.

In this section, we show that the effect of the gate gets particularly enhanced in the nanostructured film due to the effect of the induced charge in the GB region. The effect is partially helped by another aspect. The polymeric gate, during its formation from the liquid state to a polymerized state, flows through the pores in the nanostructured film and around the GB region, creating a situation that resembles an "all-around-gate". We also studied the time response of the gate current I_g as well as the drain current I_d to establish the change that occurs in the drain current is related to the electrostatic charging of the gate and it has negligible Faradic effect that can occur due to the presence of ions in the ionic gate.

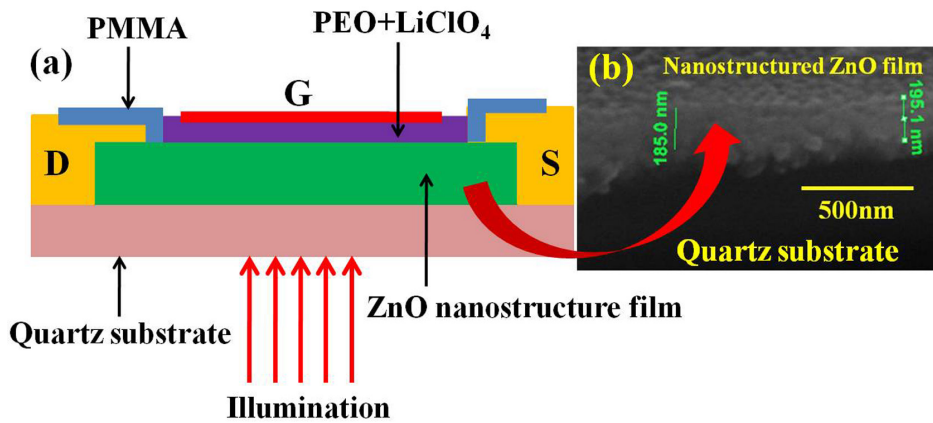


Figure 3.1 (a) Schematic of the field effect device based on nanostructured ZnO channel (b) cross sectional SEM image of ZnO nanostructured film

3.2 Gate bias dependence of UV Photoresponse and the observed synergy

The photo response of the nanostructured ZnO channel is measured using the top gate configuration of the field effect device shown in Figure 3.1 (a). In this experiment, we have used the ZnO nanostructured channel grown on quartz substrate by sol gel spin coating technique which is discussed in chapter 2. The film thickness (Figure 3.1 (b)) and average grain size (Figure 2.12 (b)) of the film were ≈ 200 and ≈ 45 nm respectively. The process of the film growth and device fabrication are already explained in chapter 2.

Figure 3.2 (a) shows typical I_d vs. V_g curves taken in dark and with UV illumination (power = 16

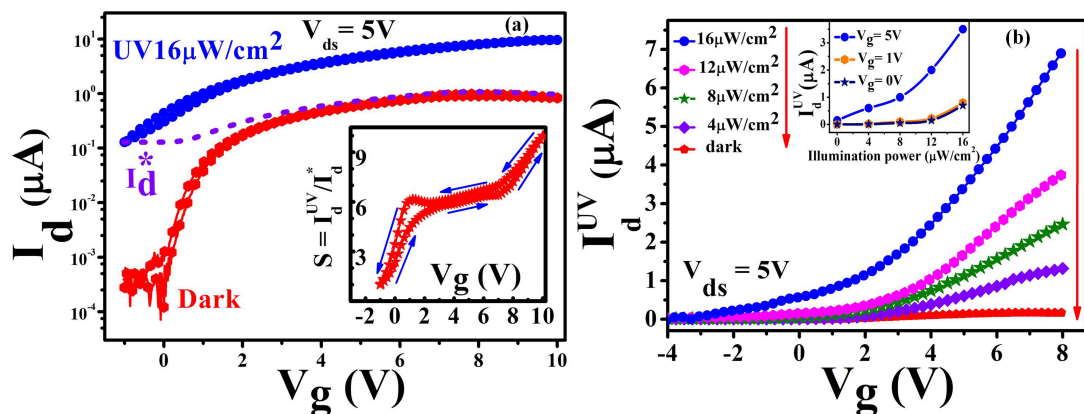


Figure 3.2 (a) Dependence of the drain current on the applied gate bias (I_d vs. V_g) in dark and under UV illumination of power (P) of $16 \mu\text{W}/\text{cm}^2$. The I_d is shown in the log scale to accentuate the low dark current. The inset shows the dependence of the ratio (S) on the applied gate bias (V_g). (b) I_d vs. V_g in dark and under UV illumination of varying power (P). The inset shows the dependence of I_d on P for fixed gate bias.

$\mu\text{W}/\text{cm}^2$). The data were taken with a source-drain bias $V_{ds} = 5$ V. The I_d data have been plotted in logarithmic scale to accentuate the scale of changes and the low value of dark I_d . In dark, I_d shows a rapid rise at the threshold voltage $V_{th} \approx 1$ V. The dark current I_d at zero gate bias ($V_g = 0$) ≈ 0.5 nA. (henceforth we refer to the dark current taken with a gate bias V_g as $I_d^{dark}(V_g)$). The value of $I_d^{dark}(V_g)$ saturates at around $1 \mu\text{A}$ for $V_g \geq 7$ V. With UV illumination ($16 \mu\text{W}/\text{cm}^2$) the bias current at zero gate bias rises to $I_d^{UV}(V_g = 0) \approx 0.45 \mu\text{A}$, an enhancement by a factor of nearly 900 over the dark current.

This enhancement arises mostly from the photoconductive response of ZnO. Figure 3.2 (a) displays clearly the synergy effect that boosts the UV photoresponse several times more than what is expected if the two effects (gate induced FE and illumination) occur independently. The dotted curve in Figure 3.2 (a) shows $I_d^*(V_g) = I_d^{dark}(V_g) + I_d^{UV}(V_g = 0)$, which is the estimated current that would be occurred if the effect of the FE and illumination would act independently. However, the observed current at a gate bias V_g under UV illumination $I_d^{UV}(V_g) \gg I_d^*(V_g)$ shows that a synergy does build up. In the inset of the same figure (Figure 3.2 (a)), we plot the ratio $S(V_g) = \frac{I_d^{UV}(V_g)}{I_d^*(V_g)}$ as a function of the gate bias V_g which shows that the synergy builds up as the gate bias V_g is increased (The ratio $S(V_g)$ shows the enhancement of the actual observed current compared to what is expected from simple addition of two effects if they act separately.). Though, there are reports of gated UV photo-detectors [51, 57–59, 62, 64, 92, 97–99] the existence of a synergy between the two carrier generation mechanisms (illumination and gate induced FE) has not been observed. In Figure 3.2 (b) we show the I_d^{UV} vs V_g curves under different illumination powers. The photoresponse $I_d^{UV}(V_g)$ shows a non-linear dependence on the illumination power P (inset of Figure 3.2 (b)). The illumination also causes a reduction in the threshold voltage V_{th} . Reduction of V_{th} as a function of illumination power density will be discussed later on and it is shown in Figure 3.8 (a). The responsivity of the photodetector is defined as $R \equiv \left(\frac{I_{ph}}{P_A}\right)$, where the photogenerated current $I_{ph} \equiv I_d^{UV} - I_d^{dark}$ and $P_A = P \times A$, A being the active area of the film. (Note: This assumes that all incident power is absorbed by the film. This overestimates P_A and underestimates R .) The measured R depends on the gate bias V_g as well as the drain source voltage V_{ds} , as the photogenerated current depends on both these parameters. In Figure 3.3 we plot R as a function of both V_g and V_{ds} where the value of the responsivity R is in a color code. The color code shows that R increases with increase of both V_{ds} and V_g and can reach a high value of ~ 25 A/W even for moderate values of V_g and V_{ds} .

The gate bias dependence of photoresponse of the ZnO film under illumination can also be evaluated from the current gain ($G(V_g)$) over the dark current defined as $G(V_g) \equiv \frac{I_d^{UV}(V_g)}{I_d^{dark}(V_g)}$. Figure 3.4 (a) shows $G(V_g)$ as a function of V_g measured with different illumination power P . The gate bias dependence of $G(V_g)$ is non-monotonous. It initially increases rapidly with the gate bias and reaches a maximum when V_g has a value close to the V_{th} (under illumination for that given power). This gate bias where

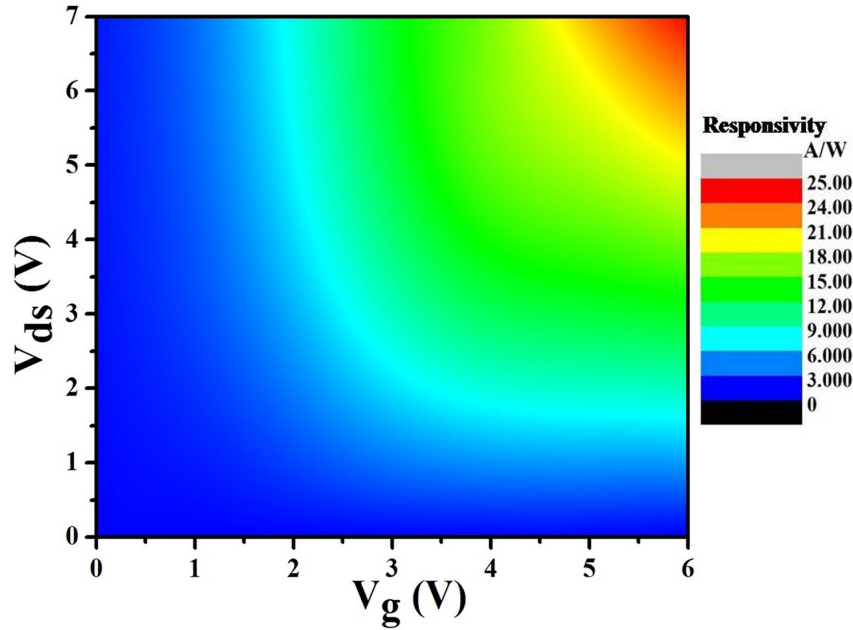


Figure 3.3 Responsivity (R) as a function of both V_{ds} and V_g . Colour code has shown in right side of the figure.

$G(V_g)$ is maximum is marked as V_{peak} . The peak response $G(V_g)$ for the illumination power of $16 \mu\text{W}/\text{cm}^2$ reaches a value as high as 1000 for a very moderate gate bias of ≈ -1.0 V. This shows that under illumination, large majority carriers that are generated suppress the depletion in the n-ZnO. The calculated surface charge Δn_s is $\approx 2 \times 10^{13}/\text{cm}^2$ has been obtained from the shift of the threshold voltage ΔV_{th} under illumination and the specific gate capacitance $C_i \approx 1 \mu\text{F}/\text{cm}^2$ (discussed later on). This value of Δn_s shows that the large charge density is induced in the ZnO film by the gate. Figure 3.4 (b) shows the dependence of V_{peak} and the maximum value of $G(V_g = V_{peak})$ as a function of P. It can be seen that V_{peak} has a linear dependence on P. It is mainly determined by Δn_s where as $G(V_g = V_{peak})$ has a low value for $P \leq 12 \mu\text{W}/\text{cm}^2$ but it increases substantially at higher illumination power i.e. the gain is enhanced strongly beyond a certain illumination power. Here, interestingly a four fold enhancement of optical power leads to 100 fold enhancement of optical gain. It is postulated that a large carrier density induced by EDL gate even with a moderate gate bias passivates charged defects states. The passivation of charged defect states reduces carrier scattering centres and enhanced the mobility that leads to enhanced photo-current and optical gain which is the cause of "synergy" between

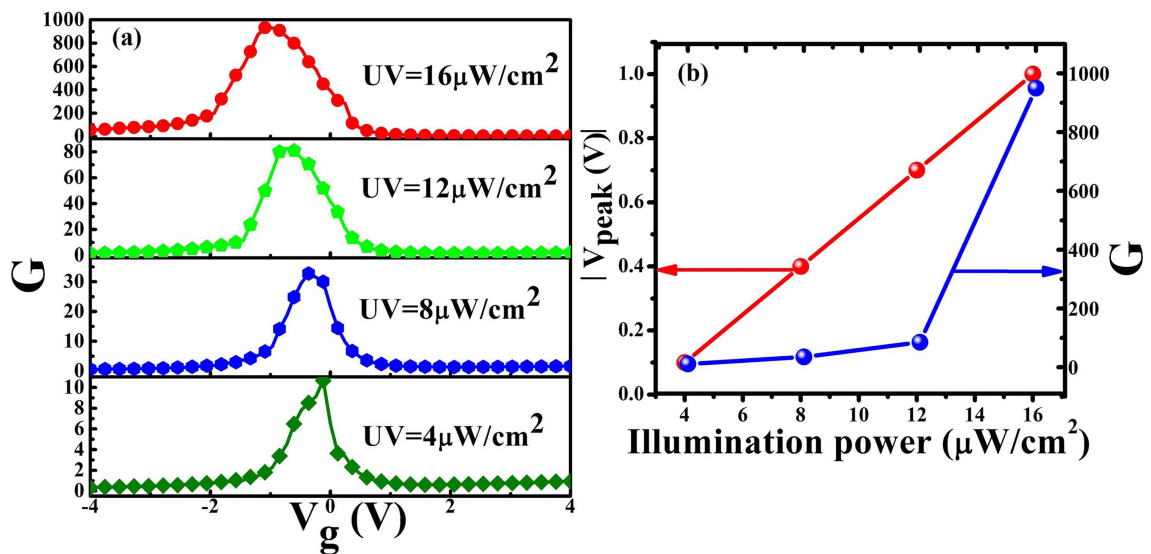


Figure 3.4 (a) The current gain (G) as a function of gate bias V_g measured with different illumination power (P). (b) V_{peak} and the maximum value of current gain G (Illumination to dark) plotted for different values of P .

light and gate induced carrier generation. This proposed hypothesis is explained in later section. As the illumination power increases, the V_{peak} changes from -0.1 to -1 V. (Note: in Figure 3.4 (b) we have plotted $|V_{peak}|$ as a function of P .) The shift in V_{peak} , as stated before is due to progressive suppression of the depletion region in the GBs with increase of P which ultimately increases Δn_s . The rapid rise in $G(V_g)$ occurs at low values of V_g due to rapid enhancement of I_d^{UV} when the dark current I_d^{dark} is still low. However, for higher gate bias and particularly when $V_g \rightarrow V_{th}$, the I_d^{dark} rises rapidly. This brings down the value of the ratio $\frac{I_d^{UV}}{I_d^{dark}}$ although the I_d^{UV} continues to increase as the gate bias increases. To summarize this part, we observe a large enhancement of the UV photo response measured in terms of the current I_d^{UV} , the parameters like the responsivity R and the current gain G in the ZnO film when a bias is applied in the gate with EDL dielectric. The observed enhancement in presence of both field effect induced by EDL as gate dielectric and illumination, points to a synergy between the two carrier generation mechanism. The total response in presence of the gate and illumination is more than the sum of the responses for the individual effects when they act alone. We discuss below (in the discussion section) the likely causes of this observation.

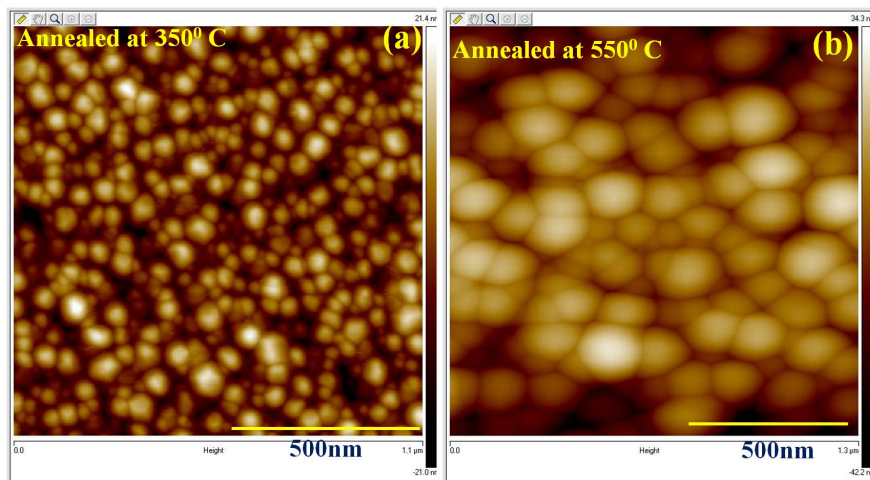


Figure 3.5 AFM image of nanostructured ZnO films (a) average grain size 25 nm and (b) average grain size 100 nm.

3.3 Effect of grain size on optical gain

In order to find the optimum grain size of the nanostructured film for the optical response, we have measured the current gain G for the nanostructured films with the same thickness but with different average grain sizes. We used the method employed in section 3.2. The nanostructured films with different grain sizes have been obtained by annealing the as grown films at different temperatures as discussed in chapter 2. In Figure 3.5 we show the AFM data for films with average grain size ~ 100 nm (a) and ~ 25 nm (b). In Figure 3.6 (a) we show the dark current I_d^{dark} and current under illumination I_d^{UV} for all the three films as a function of gate bias. In Figure 3.6 (b), the current gain G as a function of bias shown for the three films. G shows highest value for the film with average grain size ~ 45 nm. The dark current (I_d^{dark}) decreases as the grain size decreases and the current under illumination (I_d^{UV}) increases as the grain size increases. Since $G = I_d^{UV} / I_d^{dark}$, is grain size dependence. It actually depend on the value of I_d^{UV} and I_d^{dark} . For very small grain size sample, I_d^{dark} is low but I_d^{UV} is also low which makes G low. For very large grain size sample, I_d^{UV} is high so also I_d^{dark} . This also limits G . This implies that for some intermediate grain size I_d^{UV} will not be too large and not too low. This leads to an optimum grain size for which G is maximum. In our experiment, the optimum grain size is ~ 45 nm which gives largest G .

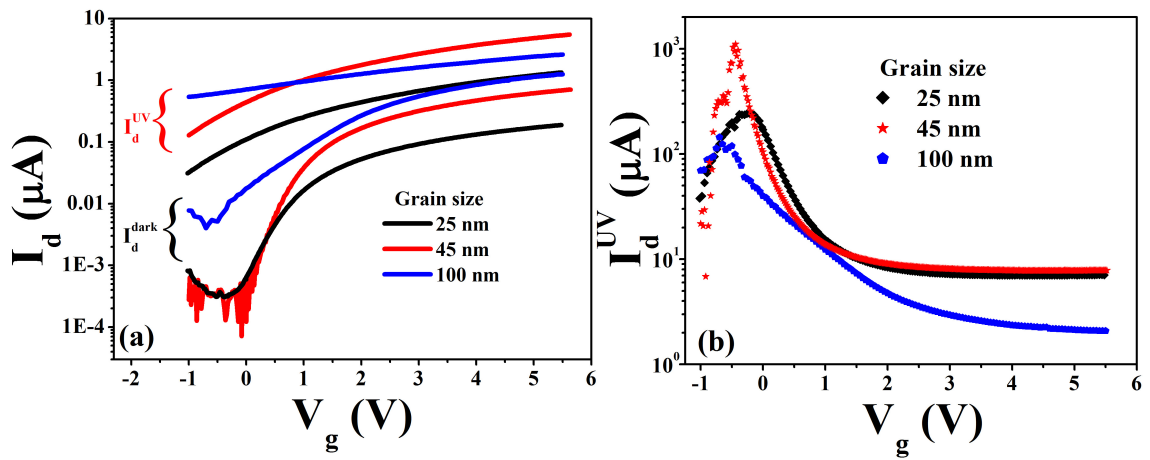


Figure 3.6 (a) Transfer characteristics of nanostructured with different grain sizes ($\sim 25, 45, 100$ nm) (b) dependence of optical Gain G with gate bias for nanostructured films.

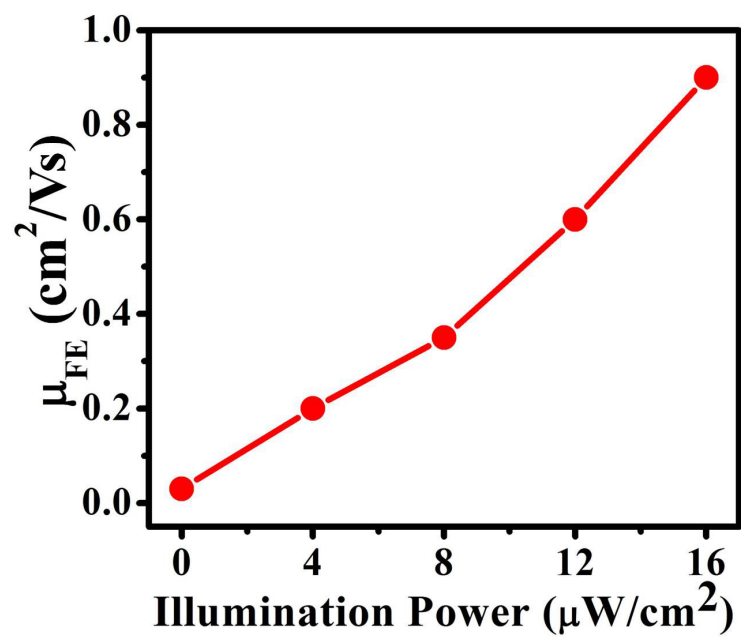


Figure 3.7 Dependence of field effect mobility (μ_{FE}) on illumination Power (P).

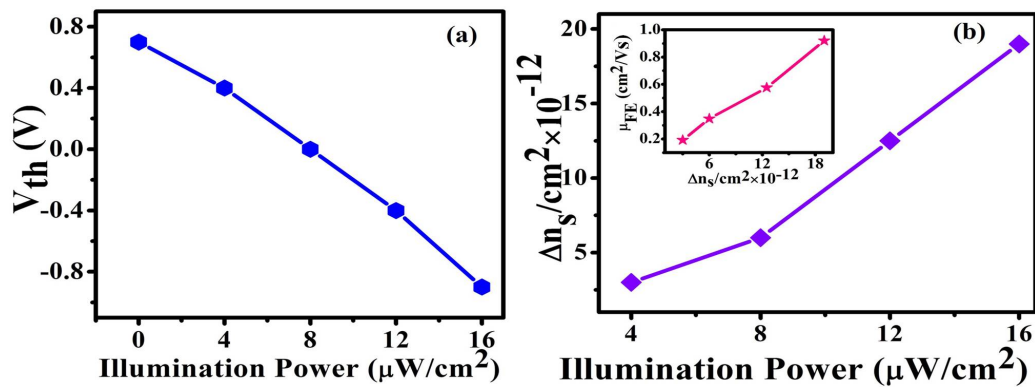


Figure 3.8 Dependence of (a) Threshold voltage (V_{th}) and (b) Induced surface charge density (Δn_s) on illumination Power (P). The inset in (b) shows that the dependence of the field effect mobility μ_{FE} on the induced surface charge density (Δn_s).

3.4 Enhancement of field effect mobility under gate and illumination

The large enhancement of the photo current due to field effect as well as the illumination can occur if the effective mobility of the carriers is enhanced significantly by the presence of the two carrier generation mechanisms. To check this hypothesis, we investigate the mobility of the channel. The I_d vs V_g curves allow us to obtain the field effect mobility μ_{FE} of the carriers in the films from the derivative $g_m (\equiv \frac{\partial I_d}{\partial V_g})$. g_m is related to the field effect mobility μ_{FE} by the relation [100]

$$g_m = \frac{\partial I_d}{\partial V_g} = \mu_{FE} C_i \left(\frac{W}{L} \right) V_{ds} \quad (3.1)$$

Where, C_i is the specific gate capacitance. The measured value of C_i from the transient gate charging and discharging current (discussed later on) we could obtain the value of μ_{FE} in the channel (ZnO) in dark as well as under illumination. It increases from $\approx 2.8 \times 10^{-2} \text{ cm}^2/\text{Vs}$ in dark by more than 30 times to $\approx 0.90 \text{ cm}^2/\text{Vs}$ under UV illumination for the highest optical power used. This in turn enhances the photoresponse observed. The low value of the mobility in the film is due to its nanostructured nature where presence of large numbers of depleted GBs inhibits the charge mobility μ_{FE} due to scattering by charged defects. In Figure 3.7, we show the dependence of the measured μ_{FE} as a function of the optical power. The enhancement of the mobility has an almost linear dependence on the optical power.

In Figure 3.8 (a) we show the shift in the threshold voltage ΔV_{th} as a function of the optical power because of excess surface carrier density Δn_s which in this case is generated by the UV illumination. In Figure 3.8 (b), we show that the change in the surface carrier density Δn_s ($= \frac{C_i \Delta V_{th}}{e}$) is due to illumination. There is a strong correlation between excess surface carrier density Δn_s (induced by the gate as well as the illumination) and the enhancement of μ_{FE} as shown in the inset of Figure 3.8 (b). We will utilize this observation to propose a plausible model of the observed phenomenon in the section 3.5 below.

3.5 Transient response of gate current and drain-source current for a step change in gate bias

When the EDL dielectric is applied on a material like ZnO in addition to the electrostatic effect of carrier induction with an applied gate bias, there may be electrochemical effects where ions may be exchanged with the material by the electrolyte LiClO₄. To check the observed effect is predominantly due to electrostatic charging of the gate capacitor, we measured the charging current (the time dependent transient current) $I_g(t)$ when a step change in the gate bias V_g is applied to the gate dielectric. We have simultaneously also measured the transient drain current $I_d(t)$. In Figure 3.9 (a) we show representative examples of $I_g(t)$ and $I_d(t)$ for a step change in the gate bias V_g from 0 V to +8 V. The transient response allows us to determine the dominant times scales associated with charging of the gate capacitor and the response of the drain source current I_d as the gate capacitor accumulates charge. The initial gate current transient has a maximum $I_{gmax} = \frac{V_g}{R_g}$, where R_g is the equivalent gate resistance through which the gate capacitor with the EDL dielectric charges. The observed $R_g \approx 15 \text{ M}\Omega$. The dominant components of the charging as well as discharging transients have a time constant τ_{1g} 0.5 - 0.7 sec. (A small current component with long time tail and time constant $\tau_{2g} \approx 10 - 15 \text{ sec.}$ also co-exists). At long time ($t \gg \tau_{2g}$) the I_g reaches a very small value, that is $< 10^{-3} I_d$ which gives the leakage current of the gate. The fast time constant τ_{1g} is identified with the time constant for the charging and discharging of the

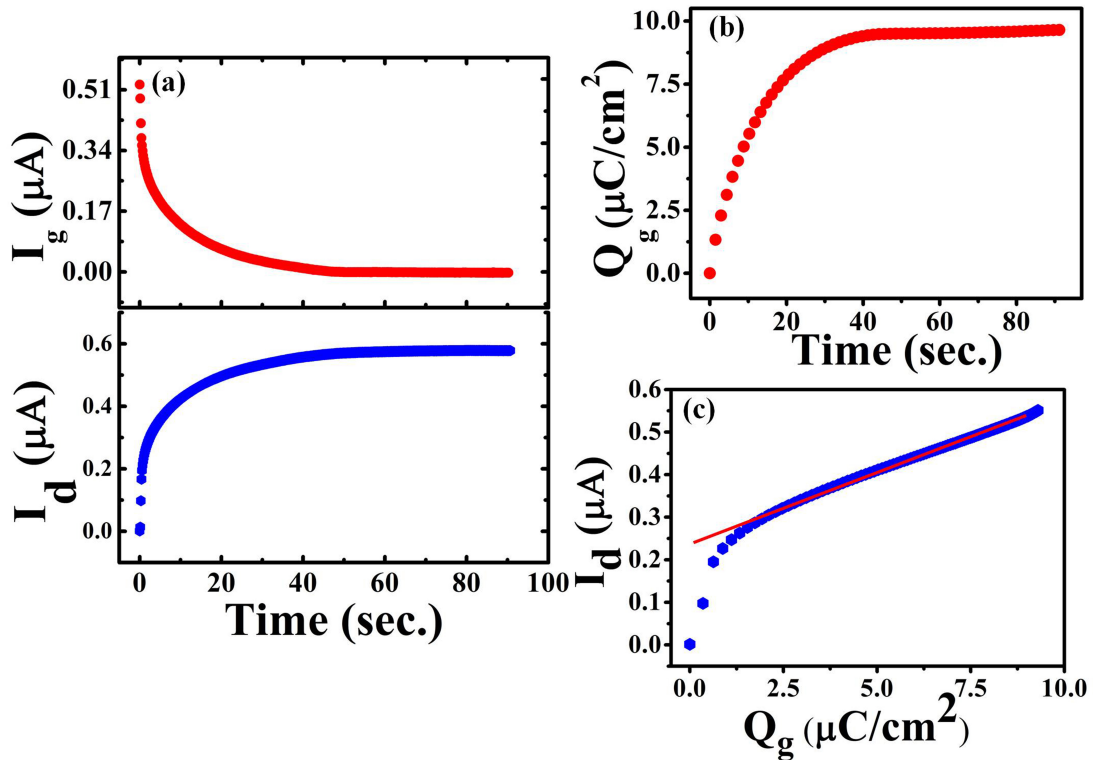


Figure 3.9 (a) Transient response of gate current $I_g(t)$ and the drain current $I_d(t)$ for a step change of gate bias by 8 V in dark (at $V_{ds} = 5$ V); (b) charge stored in the gate capacitor (Q_g) during the charging, obtained by integrating the I_g shown in (a); (c) the rise of drain current I_d with stored charge $Q_g(t)$ in the gate capacitor.

gate capacitor C_g through R_g . From the observed R_g and τ_{1g} we obtain the value of $C_g \approx 1 \mu\text{F}/\text{cm}^2$. Importantly, C_g (hence C_i) remains unchanged under illumination. This signifies that the charge created by the illumination in the channel region does not interfere with the nano-gap capacitor in the EDL gate dielectric. The small slow component (τ_{2g}) can arise from rearrangements in the electrolyte in the gate insulator at relatively larger length scales compared to the scale of the nanogap capacitor. Figure 3.9 (b) shows $Q_g(t) \equiv \int_0^t I_g(t) dt$, which is the charge stored in the gate capacitor, as a function of time obtained by numerical integration of the observed $I_g(t)$. For $t \gg \tau_{2g}$, this gives the charge stored in the gate capacitor for the given V_g . This method thus allows direct measurement of the relevant electrostatic parameters associated with the gate dielectric. $I_d(t)$, (see lower panel Figure 3.9 (a)) also follows similar time dependence as the gate current $I_g(t)$, with a fast (major) component with time constant $\tau_1 \sim 1$ sec,

which is somewhat larger but of similar order as the gate charging time τ_{1g} . This is accompanied also by a small slow component with a time constant $\tau_{2g} \sim 10$ sec. From our transient current and charging data we could directly relate the change in the gate charge $Q_g(t)$ with the time dependent build-up of the drain-source current $I_d(t)$. This is shown in Figure 3.9 (c) where we plot $I_d(t)$ vs. $Q_g(t)$. The rise of $I_d(t)$ is due to the charge accumulation in the gate capacitor. The close relation of the current I_d with gate capacitor charge Q_g shows that the effect of the EDL gate on the current in the ZnO channel is predominantly electrostatic in nature.

3.6 Discussion

In this section, we discuss the important factors that play crucial role in the observed phenomena and suggest a hypothesis for explanation of the observations made. Briefly, the large numbers of GBs that are present in such a nanostructured film play an important role in the observed phenomena. In such films, the regions in the nanocrystallites (grains) adjacent to the GB are depleted regions [20, 53]. The large surface charge induced by the EDL-gate as well as by the UV illumination control the depletion layer in the GB and thereby transport through the ZnO film leading to enhancement of the current when both the gate and the illumination are applied together (control of GB depletion width with EDL gate bias has been explained in detail in chapter 4). We have also measured the photoresponse in epitaxial film grown by pulse laser deposition technique [90]. We observed that the photoresponse of the devices based on the epitaxial film is low in comparison with the nanostructured film. For instance, at an optical power of $16 \mu\text{W}/\text{cm}^2$ in devices with same area, the maximum gain (with gate) obtained in the epitaxial film is ≈ 300 while for the film used here the gain reaches ≈ 1000 under similar condition. The fact that the polymeric electrolyte flows around the grains makes a difference in terms of providing an excess surface area that enhances the response. The presence of large number of GB in the nanostructured film accentuates this effect. This, comes about because the induced surface charge can control filling of positively charged defect states that are present in the depletion layer which in turn enhance the mobility μ_{FE} , as has been observed by the direct correlation of the enhancement of

μ_{FE} with Δn_s . The hypothesis that the filling of defect states in the GB region is controlled by the creation of large surface charge in presence of the FE and the illumination, is also expected to modify the visible emission from the ZnO film because some of these charged defect states are also involved in the visible emission particularly in the 500-600 nm range. To validate this, we also performed an experiment of gate controlled PL. In particular, emission in the blue-green region is known to occur from the doubly and singly charged oxygen defects [47, 101, 102]. It had been shown before that the reduction of the band bending or surface charge controlled by extra charges can reduce the blue-green emission in ZnO nanoparticles [103]. Figure 3.10 (a) shows the PL spectra from the channel at different gate bias. The data were taken using the arrangement shown in Figure 2.25. It can be seen from the

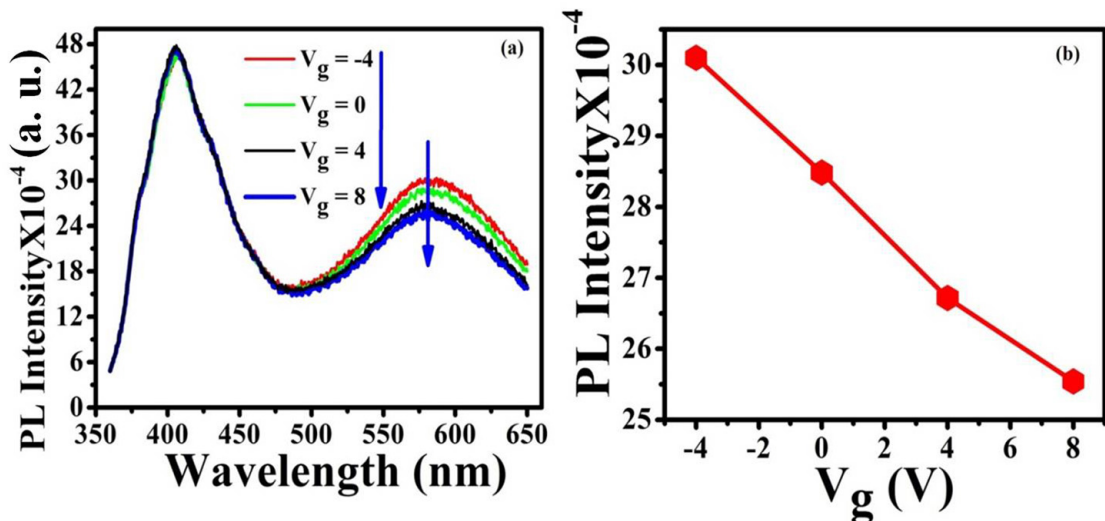


Figure 3.10 (a) Dependence of the PL spectra (taken with excitation 340nm) in blue-green region on the gate bias V_g ; (b) intensity at 580nm as a function of gate bias. Negative gate bias enhances the intensity while positive bias decreases it.

figure that with increase of the gate bias, the defect related PL in the visible region is reduced considerably. In figure 3.10 (b) where the intensity of visible emission at $\lambda \sim 580$ nm is plotted as a function of gate bias, a negative bias enhances the intensity whereas a positive bias decreases it. Here a positive bias induces negative carriers (majority carriers) which fills-up and passivates the charged defect states there by reducing the trap density Q_t in the GB region. The enhancement of the intensity occurs when the depletion region is further depleted due to induction of positive carriers in the channel by a negative

gate bias. The control of the PL in the visible region (that arises from defect states) by the gate provides a clear evidence in favour of the mechanism suggested and also provides a new application potential. In Figure 3.11 we show a simple schematic diagram to show the depletion region and the resulting band bending at a GB. The grain boundary region is depleted of majority carriers and forms a double Schottky barrier with the nanocrystallites on both sides of the grain boundary (see Figure 3.11). The GB region has spatial dimension, which is less than that of the nanocrystallites. This double barrier, characterized by the barrier height ϕ_{GB} , is an important controlling parameter for the carrier transport phenomena in nanocrystalline ZnO TFT. ϕ_{GB} Depends on the carrier concentration (n) within the

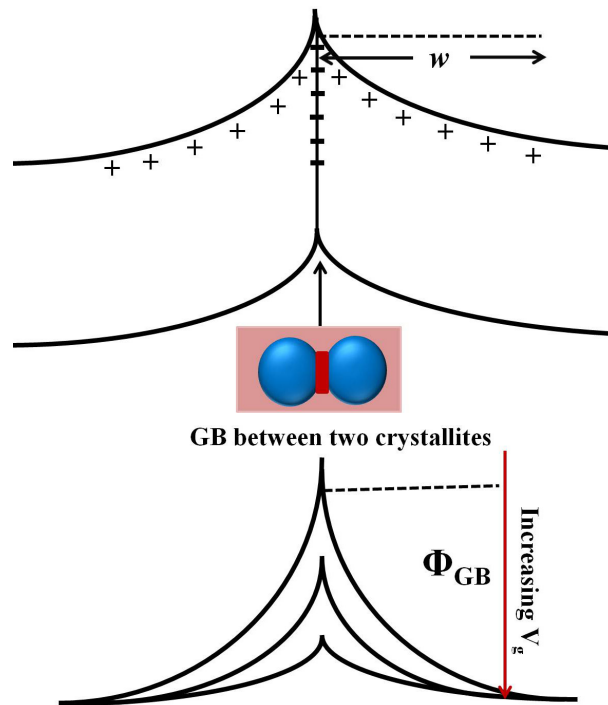


Figure 3.11 Band diagram near GB to explain the effects and band filling.

nanocrystallites (grains) that lie on the two sides of the GB and the trap density Q_t at the interface. It is given as: [20, 53]

$$\phi_{GB} = e^2 \frac{Q_t^2}{8\epsilon_0\epsilon n} \quad (3.2)$$

($\epsilon_0 \epsilon$ is the dielectric constant). The barrier height ϕ_{GB} decreases when there is increase of n and/or decrease of Q_t . Both these changes can be achieved by large carrier generation by light as well as gate. The width of the depletion region varies as $w \propto n^{-1/2}$. The creation of large surface charge (majority carriers) on application of a positive gate bias as well as by illumination leads to reduction of the band bending due to accumulation of the majority carriers (i.e., enhancement of n). This changes the occupation of the charged defect states as seen in the gate control of the visible PL. This also lowers the barrier height ϕ_{GB} in the depletion region due to lowering of trap density Q_t as well as increase of n . Since $\mu_{FE} \propto \exp\left(-\frac{\phi_{GB}}{k_B T}\right)$, this will enhance μ_{FE} , a fact established directly by the experimental observation leading to enhancement of I_d . The enhancement of the device current I_d in presence of gate and illumination occurs due to enhancement of the mobility μ_{FE} as established before (Figure 3.7). μ_{FE} as well as the induced surface charge density (Δn_s) increases almost linearly with the optical power and for the maximum power the enhancement in μ_{FE} is by a factor of 30. Lowering the barrier ϕ_{GB} by even a moderate amount ≈ 90 meV, will enhance the μ_{FE} by a factor of 30.

3.7 Conclusion

In this chapter we have shown, how a large carrier density induced by a gate with EDL dielectric in presence of UV illumination can induce a large enhancement in the photoresponse of ZnO nanostructured films. The enhancement in the drain-source current I_d in the gated photo detector leading to a large gain $G(V_g) = \frac{I_d^{UV}(V_g)}{I_d^{dark}(V_g)}$ as high as 10^3 happens on application of a modest gate bias in presence of illumination intensity $16 \mu\text{W}/\text{cm}^2$ for the nanostructured ZnO film having optimum grain size about 45 nm. This phenomenon occurs due to a large enhancement of the field effect mobility μ_{FE} which is enhanced due to the reduction of the barrier ϕ_{GB} in the GB region by the large carrier density created by FE induced by the gate and the illumination acting in tandem. It has been proposed that the large carrier density, so generated, can passivate the charged defect states thereby reducing the trap density Q_t in the GB region that leads to the enhancement of the mobility μ_{FE} . This hypothesis has been

verified by a separate experiment where it has been shown that the defect- controlled visible emission (PL) that occurs from the same singly and doubly charged oxygen vacancies located predominantly in the GB regions, was controlled by the gate bias. The experiment showed how through control of the defect states at the GBs and control of GB depletion layer in nanostructured n-ZnO film, one can induce a synergy between illumination and gate induced field effects leading substantial enhancement of photoresponse. Though, the experiment is done in specific context of n-ZnO, it has a general validity and can also be applicable in similar photoconductive oxide films where charged defects can control the carrier transport.

Chapter 4

Control of grain boundary depletion layer using electric double layer gate dielectric

Operation of thin film transistor (TFT) using an electrolyte as gate dielectric depends on modulation of grain boundary depletion layer. The experiment done in this chapter investigate this aspect of TFT using this powerful tool impedance spectroscopy. Modulation of the grain boundary barrier in ZnO nanostructured thin films having different surface morphology is investigated using EDL gate bias. The complex impedance is changed by the large number carriers induced by positive gate bias. The observed data were explained as arising from control of the grain boundary depletion layer and the associated grain boundary capacitance (C_{GB}) as well as the grain boundary potential barrier (ϕ_{GB}) by the field induced large charge density.

4.1 Introduction

In recent years, thin film transistors (TFTs) based on oxide semiconductors like ZnO, IGZO, etc. have grown tremendous interest for electronic and optoelectronic applications [104–106]. In polycrystalline or nanocrystalline oxide semiconductor films that are used as TFT channels, the mobility is limited by the presence of a large number of grain boundaries (GBs). Existence of depletion layers at the GBs lead to reduction of mobility in such films. The GBs thus play a critical role in the transport properties of nanostructured thin films due to their localized potential barrier with high density of defect states [42, 95, 107–109]. The low mobility of charge carriers in oxide based semiconductors due to the presence of GBs limits an application potential.

Control of GB defect states would thus lead to control of the grain boundary (GB) transport. One effective way to control GB transport in such films is to have an enabling tool that can control the GB depletion layer. Induction of large surface charge density (n_s) using gate dielectrics can be an effective way to have a reversible control on the grain boundary depletion layer. This is because the energy barrier at the GB reduces upon induction of the majority of the carriers by the gate. The change in chemical potential due to induced charge is $\Delta \phi = (k_B T) \ln(n + (\delta n/n))$, where the n is the native volume charge density, k_B is the Boltzmann constant, δn is the change in native volume charge density, and T is temperature. An increase in charge carrier density by 1 order can change the chemical potential by ~ 0.05 eV.

In the case of oxide semiconductors, the native volume charge density (n) can be very large ($n \geq 10^{19}/\text{cm}^3$) [110, 111]. As a result, creating a large enough n_s using a field effect (FE) that can shift the chemical potential and neutralize the depletion layer considerably. It would need the application of a large gate voltage when conventional gate dielectrics are used. An alternative will be to use dielectrics such as an ionic liquid or a polymeric electrolyte. The polymeric electrolyte creates an electric double layer which can induce a large charge density about 2-3 orders larger than the n_s that can be created by gates with conventional dielectrics. This large charge density on the TFT channel can lead to control of metal insulator transition, optical response, and control of optoelectronic properties like persistent

photo conduction by EDL gate which we have already discussed in chapter 1.

Though control of GB transport in polycrystalline ZnO has been widely investigated [20, 47, 53, 108, 112–114], but the control of the depletion layer at the GB using an EDL as a gate dielectric has not been previously reported. In this chapter, we show that in a channel of ZnO, it is possible to have a large control of the GB depletion layer using EDL as a gate dielectric. Charged defect sites on the individual nanocrystallites surfaces act as trap sites for a majority of carriers and create a potential energy barrier at the contact region of the adjacent crystallites which we have discussed in chapter-III. The grain boundary trap states reduce the mobility of the majority carriers and reduce the conductivity of the film. Depletion layer forms on the ZnO surface, in particular on the surface of ZnO nanoparticles, due to depletion of the majority carriers by surface defects (like positively charged oxygen vacancy). Existence of such depletion layers on ZnO nanoparticles has been established by measurement of the charge on them and by photoluminescence spectroscopy [47]. In nanostructured ZnO films, the depletion layers arise from the majority carriers depleted surface of individual nanocrystallites that make the film. The work presented here has been done in EDL thin film transistor configuration (EDL-TFT) using a ZnO channel with different morphologies that give rise to GB with different extents of depletion layers. We have used frequency-dependent measurement of the drain-source (DS) impedance (Z) in the presence of different gate voltage V_g as the tool to investigate the effect of the gate bias on GB depletion layer. Alteration of the depletion layer by the induced charge changes the ϕ_{GB} as well as the depletion width (w). The modified w predominantly leads to a change in the C_{GB} as well as the GB resistance (R_{GB}) which leads to changes in the complex impedance Z and its frequency dependence. We show that the change in Z with the applied gate bias has a strong dependence on the nature of the film morphology that determines the nature of the GB.

The transport through GB in polycrystalline films as stated before is primarily controlled by the following factors: ϕ_{GB} and w . The effect of these parameters on the transfer characteristics of TFTs have been addressed before [53, 108, 109]. However, the role of these factors in control of C_{GB} and, in particular, how they control the complex impedance of such a film when the GB region is modified by field effect induced charges have also not been addressed. While the effect of the gate in ZnO based TFT has been

discussed in models, [20, 108, 115, 116] there are no experimental studies particularly reporting on the EDL gate to study the GB depletion layer and the associated resistance and capacitance at the GB, when a large charge density is induced by a gate with an EDL dielectric.

In previous chapter, we have discussed the enhancement of field effect mobility by controlling the GB depletion width and charged defect states using EDL gate bias. But, this observation is insufficient to know the carrier transport specially through GB regions. In this chapter, we again use a TFT configuration to study the effect of applied gate bias on complex impedances of n-type ZnO films of different morphologies and investigate how induced charges can control the carriers transport through the GBs.

4.2 Experimental details

4.2.1 Films and their characteristics

In this chapter, we studied nanostructured ZnO films with different morphologies. The films were grown on Si/SiO₂, R-Sapphire (1102) and Kapton[®] substrates using pulsed laser deposition technique. Excimer laser (KrF with $\lambda = 248$ nm) was used for the ablation in a vacuum chamber where the base pressure was 1×10^{-5} mbar. Table 4.1 gives the detail informations of these films. The different substrates using the film growth, lead to different film morphologies that are qualitatively different. The film thickness shown in Table 4.1 was measured by spectroscopic Ellipsometry. XRD pattern (Figure 4.1) of ZnO films on different substrates were taken with CuK α radiation. As it can be seen, the film grown on the SiO₂ (300 nm) on Si is polycrystalline with random grain orientations and incoherent grain boundaries. The films grown on R-Sapphire (1102) and Kapton[®] are strongly textured with growth in (002) direction. The micro/nanostructure of the films was characterized using Atomic Force Microscopy (AFM). Figure 4.2 shows the AFM images of films grown on different substrates. The root mean square roughness of the films grown on Si/SiO₂, R-Sapphire (1102) and Kapton[®] measured by AFM are found to be 4.5 nm, 0.6 nm, and 3 nm respectively. The average grain sizes of the films as measured by AFM are 140 nm, 40 nm and 30 nm respectively. The combination of the XRD and AFM

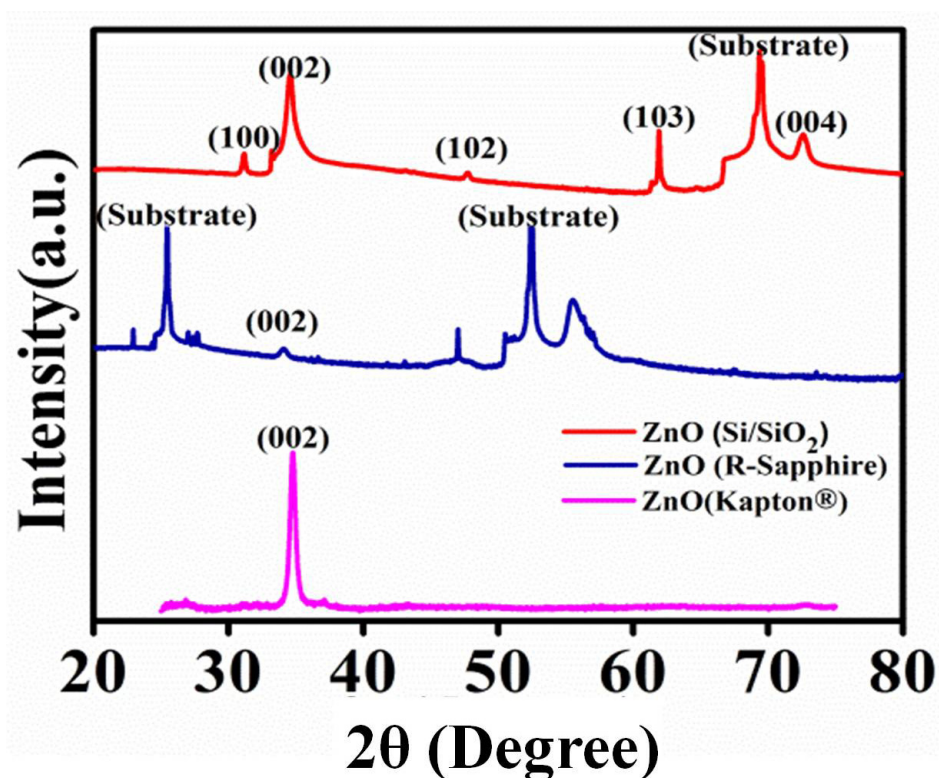


Figure 4.1 X-ray diffraction of three PLD grown nanostructured ZnO films used in the work. Film grown on Si/SiO₂ (Sample A) is nanocrystalline with random grain orientation. Films grown on R-Sapphire (Sample B) and on Kapton[®] (Sample C) are strongly textured in (002) direction.

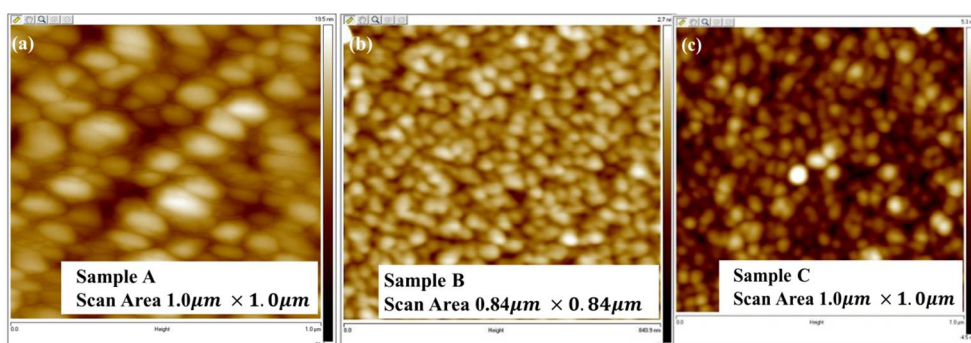


Figure 4.2 AFM micrographs of the films grown on different substrates (a) Si/SiO₂, (b) R-Sapphire (1102) and (c) Kapton[®].

data establish that all the films are nanostructured although the grain sizes vary. The nanostructured films also differ in grain morphologies. While film A has random grain orientations (as established

Table 4.1 Morphology and thickness of the ZnO films grown on different substrate.

Sample	substrate	Thickness (nm)	Average grain (nm) size (nm)	Nature of film
A	SiO ₂ (300 nm)/Si	~140	~140	Polycrystalline, random grain orientations and incoherent grain boundary
B	R-Sapphire (1102)	~40	~40	Strongly textured with coherent grain boundaries
C	Kapton [®]	~100	~30	Nanocrystalline but highly textured with well-connected grains

through XRD), films B and C have oriented grains. For films A and B the average grain sizes are comparable to film thicknesses. This likely makes the film with columnar growth and we may think of the GB as arranged in 2-dimensional network. In contrast, the film C has much larger thickness than the grain size. This makes the GBs within the film arranged in a 3-dimensional network.

4.3 Fabrication of EDL-TFT and impedance measurement

The gate dependence of the impedance spectroscopy was done on the above described ZnO thin films in a TFT device configuration using polymeric electrolyte as a gate dielectric. A schematic of the TFT device is shown in Figure 2.20. The devices were fabricated on patterned films. Au/Cr contact pads as source (S) and drain (D) electrodes were made by thermal evaporation. The preparation of polymeric electrolyte and its implication is already discussed in chapter 2 (Section 2.4). The electrolyte at the interface with ZnO forms an electric double layer (EDL). The D and S contact pads were protected from the electrolytic gate by a layer of PMMA. The gate dielectric before evaporation of the solvent

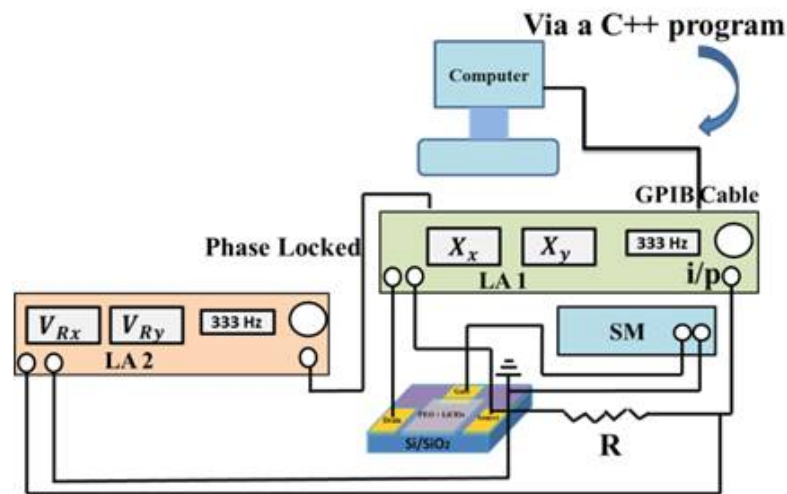


Figure 4.3 Schematic of the impedance measurement circuit used.

flows into the rough regions of the channel and makes a conformal coating. This leads to inhibition of roughness induced degradation of field effects seen in gates with solid dielectric.

Complex impedance ($Z(\omega) = Z'(\omega) + iZ''(\omega)$) of the thin film channel between D and S electrodes (with fixed gate bias (V_g) applied on the EDL gate) was measured at room temperature in the frequency range 100 Hz to 100 KHz using a lock-in amplifier technique [117, 118]. The schematic of the measurement circuit is shown in Figure 4.3 (The impedance measurement was set-up and done by Mr. Ravindra Singh Bisht of our group). The impedance measurement set up had a standard resistor (R) connected in series with the device (X). The lock-in amplifier LA1 measures the bias across the terminals D and S for a given current through the device. X_x And X_y are the in-phase and out- of phase voltages across the D-S terminals of the sample measured by LA1. The second lock-in amplifier LA2 measures the in-phase (V_{Rx}) and out- of- phase (V_{Ry}) component of the voltage across R. LA1 provides the a.c excitation and LA2 is phase-locked with LA1. The complex impedance $Z(\omega)$ is given as: [117, 118]

$$Z(\omega) = R \times \left(\frac{X_x}{\sqrt{V_{Rx}^2 + V_{Ry}^2}} + j \frac{X_y}{\sqrt{V_{Rx}^2 + V_{Ry}^2}} \right) \quad (4.1)$$

The observed $Z(\omega)$ was analysed using a model to extract the lumped parameters such as R_{GB} and C_{GB} (discussed later on). The bias dependence of the lumped parameters was used to investigate the bias dependence of the average grain boundary barriers and the average depletion layer width of the GB. In

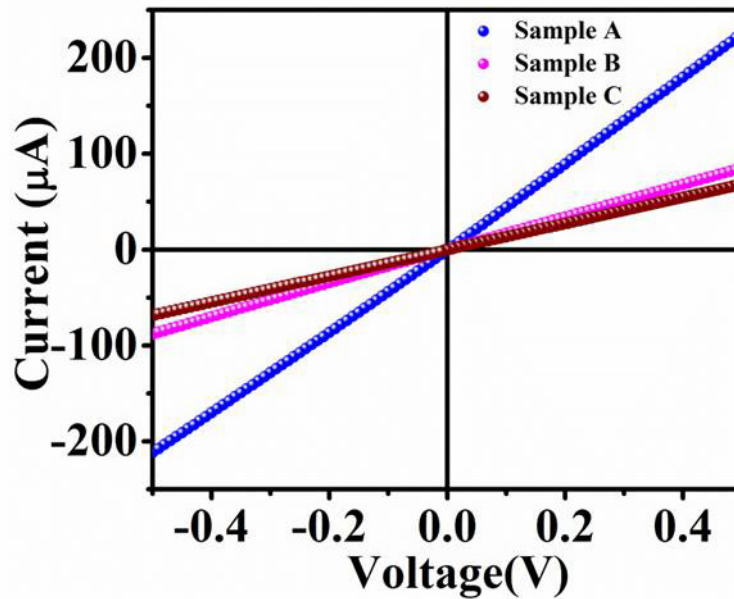


Figure 4.4 *I-V* characteristics of the films measured with the Cr/Au contact pads showing their Ohmic nature.

in addition to impedance spectroscopy, which is the main focus of the work, we also carried out dc measurements of the *I-V* characteristics of the ZnO thin film channel and also the transfer characteristics of the EDL-TFT devices using source meters. The transfer characteristics are presented to show the basic differences in the transport in the three films in presence of the gate bias, when they have different morphologies.

4.4 Basic TFT characteristics

Figure 4.4 shows the *I-V* characteristics for the three samples. The linear behaviour of the *I-V* curves establishes ohmic nature of the transport in the channel as well as that at the contacts. One of the important characteristics that reflect the different morphologies of the three films is the transfer characteristics of the EDL-TFT's. The data are shown in Figure 4.5. The current (I_d) is shown in the log scale to accommodate the transfer characteristics of all the three EDL-TFT's. The TFT made on film grown on R-Sapphire that has oriented grains with coherent GBs shows maximum current.

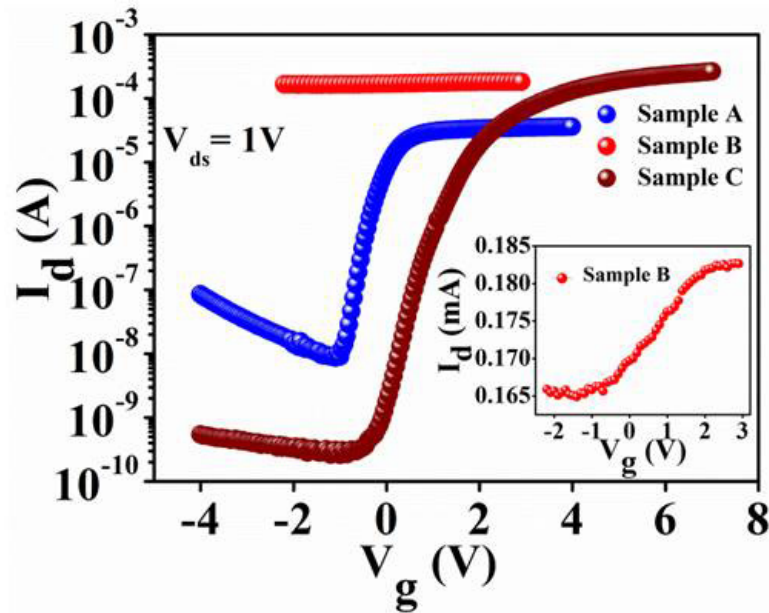


Figure 4.5 Transfer characteristics of the gated TFT. The inset shows the characteristics of the sample B (grown on R-Sapphire) in linear scale.

However, it has very low ON/OFF ratio and it starts to conduct at $V_g = V^* = -1.5 V$ and has a threshold voltage $V_{th} \approx -1.2 V$ (see inset of Figure 4.5 for more details). This film, as we will see below does not have much contribution from GBs that get tuned by the gate bias. In contrast, film A is grown on Si/SiO₂ has nanograins with random GB's (although with somewhat larger grain size) shows much larger ON/OFF ratio $\sim 10^2 - 10^3$. This film shows onset of transport at $V^* = -1 V$ and a threshold $V_{th} \approx -0.3 V$. In this film the GBs are more depleted of majority carriers compared to those in film B as can be concluded from the values of V_{th} and V^* . The film C grown on Kapton[®] that has nanostructured films with strongly oriented grains shows very large ON/OFF ratio reaching a value close to 10^6 . The GBs in this film appear to be more depleted as appear from the values of $V^* = -0.5 V$ and $V_{th} \approx 1.75 V$. The transfer characteristics and the ON/OFF ratio in these TFT depend critically on the GBs and the depletion layer on them as well as the trap states. We show below that control of these parameters by the gate bias arise primarily due to change in the depletion layer at the GBs which leads to a change in the barrier potential as well as the characteristic capacitance and resistances at the GB.

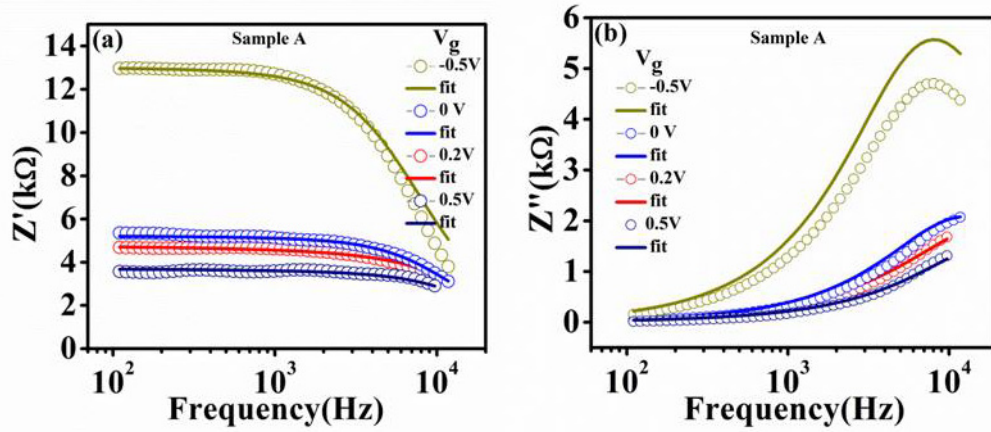


Figure 4.6 (a) Real (Z') and (b) imaginary (Z'') parts of impedance of sample A for different gate bias.

4.5 Frequency dependent impedance $Z(\omega)$ with varying gate bias

Figure 4.6-4.8 show the frequency dependent complex impedance data $Z(\omega)$ on the three films taken with varying gate bias V_g . The data was taken over the frequency range from $f = 100$ Hz to 100 KHz ($\omega = 2\pi f$). Application of gate bias has large effects on the impedance of samples A and C and negligible effect on that of sample B. In particular, in sample C (the oriented nanostructured film) the gate effect on the impedance is very large. We have plotted both Z' and Z'' for 0 V and 3 V in the inset also. The observed behaviour reflects the different nature of the GBs in the films arising from different morphologies. The change of the gate bias from negative to positive makes the n-type films go from highly depleted conditions (due to induction of positive charge by gate) to accumulation region (due to induction of negative charge). The gate bias also changes the frequency dependence of both Z' and Z'' . The change in the frequency dependence on application of gate bias arise largely due to change in the GB capacitances with additional contribution from a changing GB resistances, which we will discuss later on.

The relative changes in Z' and Z'' on application of gate bias has been parametrized by 2 quantities namely $\xi' = -(1/Z'_0) (\Delta Z' / \Delta V_g)$ and $\xi'' = -(1/Z''_0) (\Delta Z'' / \Delta V_g)$, where the negative sign reflects the negative changes $\Delta Z'$ and $\Delta Z''$ in Z' and Z'' respectively, for a positive swing in gate bias ΔV_g

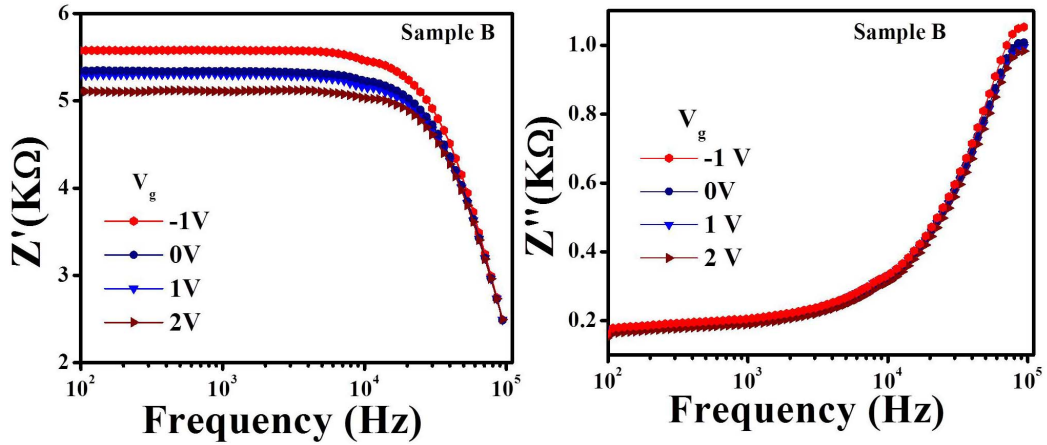


Figure 4.7 (a) Real (Z') and (b) imaginary (Z'') parts of impedance of sample B for different gate bias.

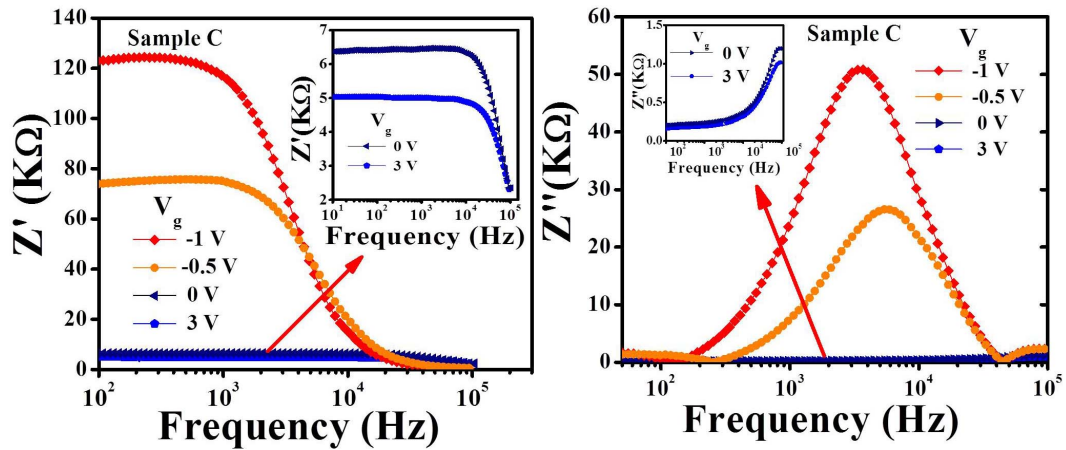
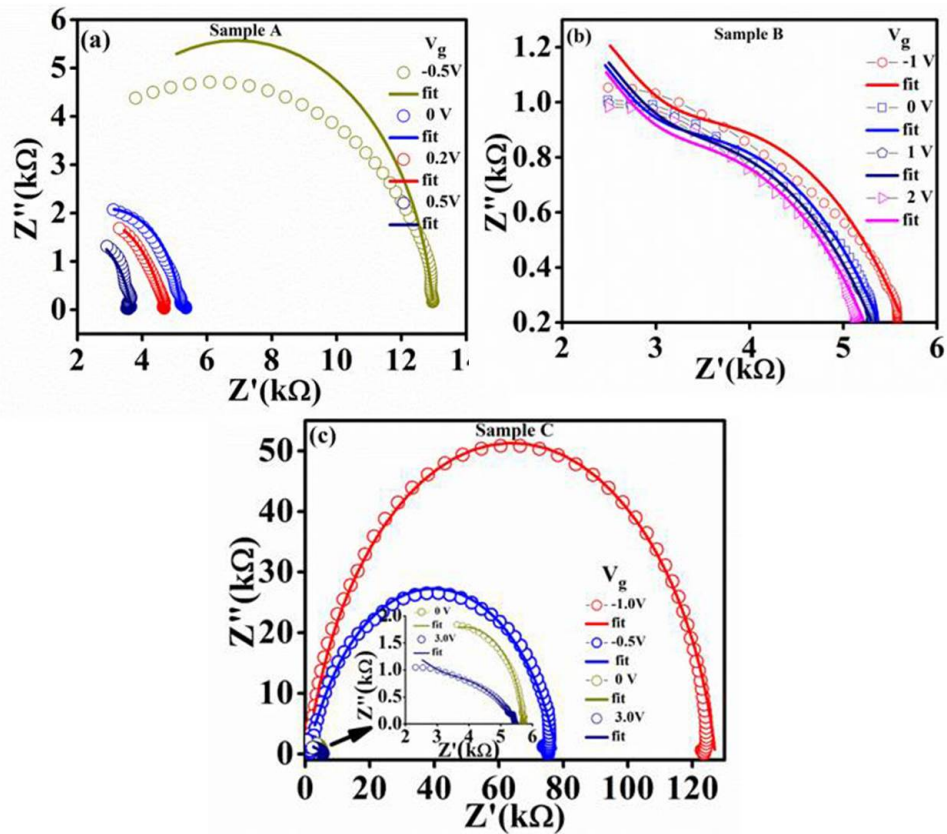


Figure 4.8 (a) Real (Z') and (b) imaginary (Z'') parts of impedance of sample C for different gate bias.

that drives the gate from negative to positive which makes the film go from depletion to accumulation regimes (Z'_0 and Z''_0 represent value of Z' and Z'' respectively at $V_g = 0$). For the swing of the gate bias from -0.5 V to $+0.5$ V ($\Delta V_g = 1$ V) the change in carrier surface charge density (Δn_s) at the EDL-ZnO interface is given by the specific gate capacitance C_i , $\Delta n_s = C_i \Delta V_g / q$. From the measured gate capacitance $\sim 4 \mu\text{F}/\text{cm}^2$ (sample A) one can estimate that for $\Delta V_g = 1$ V, $\Delta n_s \approx 2.5 \times 10^{13} / \text{cm}^2$. The value of ξ' and ξ'' evaluated at two frequencies 100 Hz and 10 KHz are shown in Table 4.2. It can be seen from Table 4.2 that in the samples A and C the parameters ξ' and ξ'' are relatively larger and

Table 4.2 Parameters ξ' and ξ'' at 100 Hz and 10 KHz.

Sample	with gate bias		with gate bias	
	100 Hz	10 KHz	100 Hz	10 KHz
	ξ' (V^{-1})	ξ' (V^{-1})	ξ'' (V^{-1})	ξ'' (V^{-1})
A ($ZnO/SiO_2/Si$)	2.00	0.43	5.31	1.89
B ($ZnO/Sapphire$)	0.03	0.027	0.028	0.023
C ($ZnO/Kapton$)	5.11	0.408	10.41	16

**Figure 4.9** (a) Nyquist plots for the three films taken with different gate bias (a) sample A, (b) sample B and (c) sample C.

both show a strong dependence on measurement frequency f . On the contrary the sample B shows very small value of ξ' and ξ'' and the parameters are mainly frequency independent. The different values of

the parameters as well as their frequency dependence reflect the grain morphologies and the resulting GBs that get controlled by the charge induced (Δn_s) by the gate.

The impedance spectroscopy data are often plotted as Nyquist plots shown in Figure 4.9. As expected the Nyquist plots show strong dependence on the gate bias for samples A and C and have negligible dependence for sample B. The Nyquist data show that there is at least one prominent relaxation time in the films which gets tuned by the gate bias. Though the Nyquist plots do not show closure of the semicircles in most of the data regions (except that in strongly depleted film C), it may be noted that the relaxation is non-Debye type.

The qualitative differences in the impedance data and their gate bias dependences in the three films presented above, along with the transfer characteristics of the TFT made from these films very clearly establish the role of the grain morphology and GBs. In the following analysis and the accompanying discussion we would like to bring out the quantitative changes that the gate bias do to the GB parameters (and the suggested mechanisms) that lead to these changes.

The main effects investigated are the effects of the GBs and C_{GB} that can be changed by the gate bias due to modification of the GB depletion region caused by large induced charges that an EDL gate dielectric can induce.

The data presented above establish a strong connection of the gate bias dependence of impedances of films with different morphologies. In the following part of this chapter we first extract out parameters such as R_{GB} and C_{GB} from the data. Next the effect of gate bias on these parameters is discussed and it is established that the modification of the GB depletion region by the gate induced charges is a prime factor that leads to changes in R_{GB} and C_{GB} . The data above show that the changes occur at a low gate voltage $V_g < 3$ V. This is possible by induction of large surface charge density (n_s) by the applied gate bias using the EDL as gate dielectric.

A simple schematic model of the potentials, length scales and the relevant energy levels are shown in Figure 4.10 (a) and (b). The ϕ_{GB} at GB and depletion width w are marked. The defect states like those arising from oxygen vacancy are shown within the band gap. Induced charges by gate bias shift E_F . The GB region is generally considered as a double Schottky like junction with a barrier potential (ϕ_{GB})

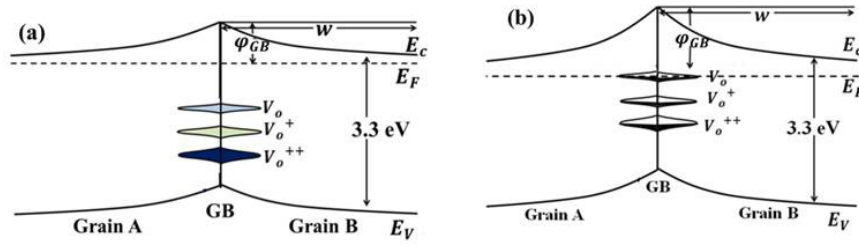


Figure 4.10 (a) Schematic of GB in accumulation region and (b) depletion Region. (Note: The Figure shown is adapted from Reference [108] and modified.)

caused by the band bending in the depletion region. There is a distribution of trap states (areal density N_t) at the surface of the GB. The gate bias, by inducing charges in the interface region (extending to a depth \sim few Debye length λ_D) changes the electron concentration (n) in a grain. Enhancement of n raises the Fermi level E_F and fills up the traps located just below the conduction band.

The induced negative charges also change the w at the GB interface which is given as follows [20, 53, 108, 115, 116]

$$w \cong \left(\frac{2\phi_{GB}\epsilon'}{qn} \right)^{1/2} \quad (4.2)$$

where ϵ' represent permittivity of ZnO.

In general, the depletion width becomes important if the barrier potential $\phi_{GB} > k_B T/q$. For $\phi_{GB} < k_B T/q$, the length scale for potential change and charge distribution from the GB to inside a grain is determined by $\lambda_D (= \frac{\epsilon' k_B T}{q^2 n})^{1/2}$. The depletion width w determines the C_{GB} since C_{GB} is $\sim 1/w$. The applied gate bias tunes the C_{GB} primarily by tuning w . Current through the film (which in the TFT configuration is the drain current I_d) is governed by the barrier ϕ_{GB} and $I_d \sim \exp(-q\phi_{GB}/k_B T)$. A small reduction in ϕ_{GB} by the gate bias will cause a substantial enhancement in I_d and will increase the effective mobility. The filling up of the traps when E_F is raised reduce the number of ionized donors (N_d^+) and also reduce scattering and hence enhance mobility leading to large ON/OFF ratio in the nanostructured films as has been seen in sample A and particularly sample C.

The morphology of the film, determined by the deposition conditions as well as the substrate, controls occupied acceptor like trap density (n_a) and unoccupied donor like trap density (n_d). These in turn determine the net negative charge ($n_e = n_a - n_d$) in the GB region. These parameters in turn control

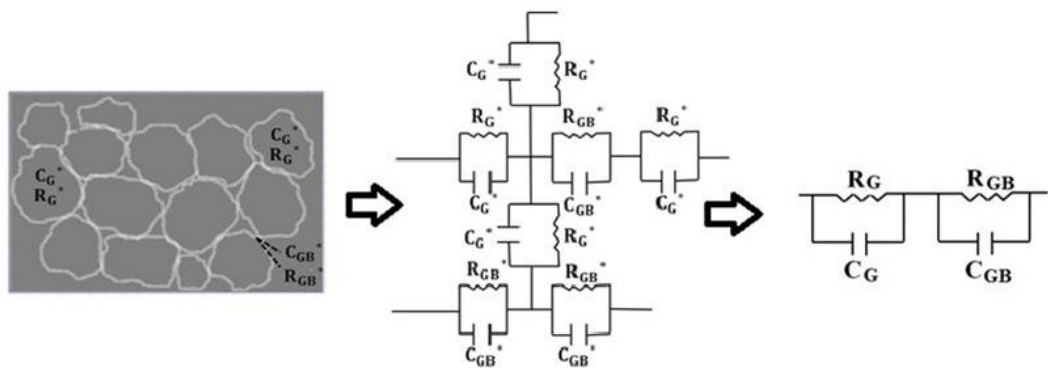


Figure 4.11 The network of grains and grain boundaries with model used for fitting.

the charge distribution in the GB region through the self-consistency relation [108]. Basic physics of the control of the depletion width w , the C_{GB} and the barrier arise from this. It is thus expected that the morphology and the details of the GB region will determine these parameters like C_{GB} and the barrier. The above brief discussion is used below to analyse and understand the impedance data.

4.6 Model analysis to extract the GB parameters

Gate bias dependent impedance data have been analysed using a simple model. The nanostructured ZnO films can be considered as a network of series and parallel combination of capacitors and resistors, representing the crystalline grains as well as the grain boundaries. A schematic of such a network is shown in Figure 4.11. The grains in the films (the crystallites) will depend on the substrates they are grown on. However, the major differences are expected to arise from the GB regions that are qualitatively different in the three films. A detailed networked model encompassing the distribution in the grains as well the GB parameters would have been the best to analyse the data. However, to capture the essential physics we used out a simple lumped circuit model where the crystallite grains have been represented by the Grain resistance (R_G) and capacitance (C_G) and the GB region represented by the parameters GB resistance (R_{GB}) and capacitance (C_{GB}) (see Figure 4.11). The relaxation has been

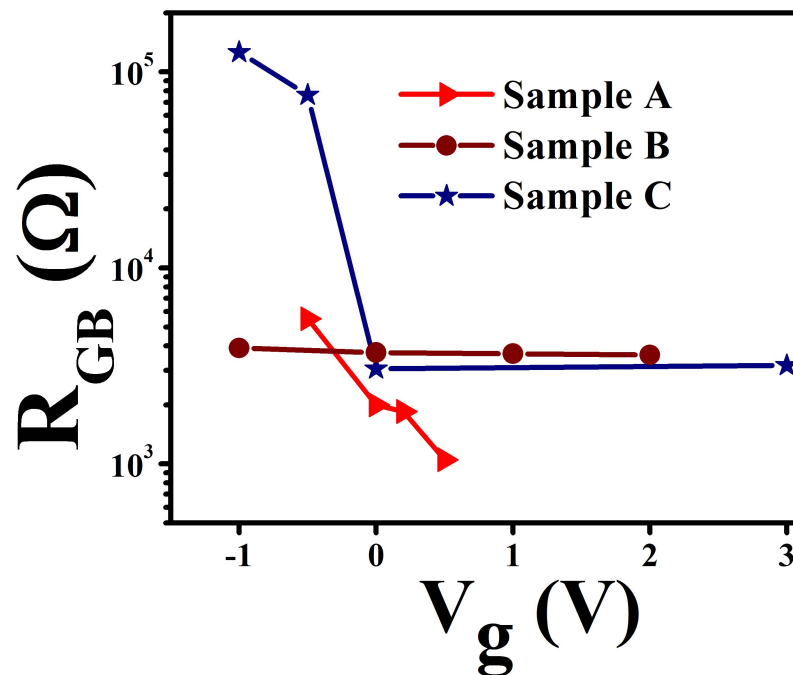


Figure 4.12 The obtained parameter R_{GB} as a function of V_g .

assumed as non-Debye type and given by following equation: [119, 120]

$$Z(w) = \frac{R_G}{1 + jwR_G C_G} + \frac{R_{GB}}{1 + (jw)^\beta R_{GB} C_{GB}} \quad (4.3)$$

Where the factor $\beta (<1)$ signifies non-Debye relaxation. The factor β has been obtained from the fit to the data and was found to be ≈ 0.5 .

A typical example of the fit of the model to the data (complex impedance) is shown by solid lines in Figure 4.6 (a) and (b). An example of the fit to the Nyquist plots is shown in Figure 4.9. The data clearly show that while the model give satisfactory fit to the data both in regions of strong depletion (negative V_g) as well as accumulation (positive V_g) for the nanostructured films A and C, it deviates at the high frequency end for the film B that has very little GB contribution.

The important parameters obtained from the model fits and their variations as a function of V_g are shown in Figure 4.12 and Figure 4.13. These two figures bring out clearly the extent of control on these parameters (and hence the complex impedance Z) by the applied gate bias and also the role of the film morphologies. It can be seen from Figure 4.12, the parameter R_{GB} in film B is almost independent of

the gate bias V_g , showing that the exposure of the GB region to the induced charge is minimal. Though the film has well defined grains, fact that they are well connected and the GB region is not depleted ensures that R_{GB} has very little dependence on gate bias. For the film C, that has oriented grain as that in film B has very similar R_{GB} as film B, but it has a large enhancement by nearly a factor of 30 when a gate bias of only -1 V is applied where the GB region gets strongly depleted. The GB morphology allows strong exposure to the gate dielectric and a small $V_g = -1$ V can create rather pronounced depletion. For film A, that has randomly oriented grains (with somewhat larger size) R_{GB} decrease gradually as the bias V_g is changed from -1 V to +1 V and the GB region is taken from depletion to accumulation. At $V_g = 0$, the R_{GB} in all the three films are similar to within a factor of 2. However, as stated before the response of R_{GB} to V_g differs qualitatively as the film morphologies change.

The R_{GB} is determined primarily by the GB potential barrier GB, $R_{GB} \propto \exp(-q\phi_{GB}/k_B T)$. The gate induced changes in R_{GB} thus can be interpreted as changes in ϕ_{GB} caused by change in the depletion layer by the induced charges. Each grain boundary has its own localized potential barrier (ϕ_{GB}), which is related to the acceptor surface density and carrier concentration (n) is given by the following: [53, 115, 116]

$$\phi_{GB} = \frac{qN_s^2}{8\epsilon_0\epsilon_r n} \quad (4.4)$$

where N_s , ϵ_0 and ϵ_r are the acceptor surface density, permittivity of free space and relative permittivity of ZnO respectively.

Relative enhancement in the RGB by a factor or 30 in film C by a negative V_g can be caused by an enhancement in GB barrier by ≈ 0.085 eV. For positive V_g , the surface charge induced in the channel lowers the acceptor surface density (N_s) on the grain surface as well as increases the carrier density (n) within a grain and vice versa. This results in reduction of barrier potential and hence reduces depletion width.

The decrease in C_{GB} values for negative V_g and an enhancement for positive V_g have been observed for all the devices as shown in Figure 4.13. The changes in depletion width of the channel control C_{GB} as given by following: [120]

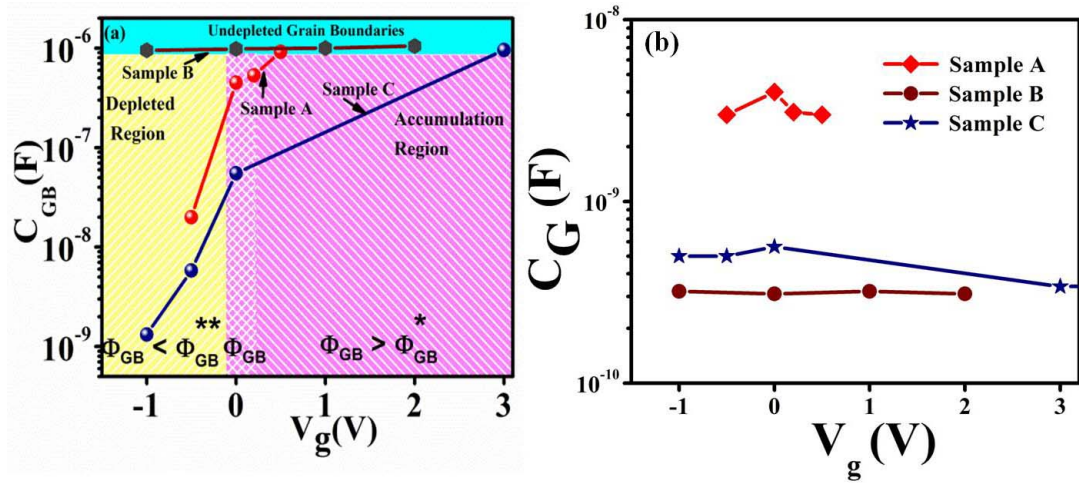


Figure 4.13 The obtained parameter (a) C_{GB} as a function of V_g and (b) C_G as a function of V_g .

$$C_{GB} = \left(\frac{q\epsilon'n}{8\phi_B} \right)^{1/2} \approx \epsilon' \frac{n}{n_s} \quad (4.5)$$

Application of negative bias creates depletion and hence reduces n and enhances N_s , leading to decrease in C_{GB} .

The ZnO channel in Sample A is polycrystalline in nature with high surface roughness, and has a large number of grain boundaries. C_{GB} in this film is enhanced by ≈ 2 orders. In Sample B the C_{GB} is fairly constant with V_g . It can be understood in terms of less GB contribution and absence of depletion in GB regions. Sample C has oriented nanostructured with moderate roughness and GB's can be controlled considerably by applied gate bias which results in a large change by nearly 3 orders in C_{GB} . Most of the change in C_{GB} occurs (2 orders) when V_g changes from -1 V to 0 V. This change in V_g causes a large change in R_{GB} as noted before. The overall experiment concludes that higher modulation of C_{GB} is obtained on films with highly oriented grains and with moderate roughness.

In all the films it is to be noted (see Figure 4.13 (a)) that for the positive gate bias the value of C_{GB} approaches a single limiting value, which is comparable to the gate bias independent value of C_{GB} observed for Sample B. It is likely that this value of C_{GB} is reached when the w on large charge accumulation, reaches the value comparable to the Debye length.

The C_G is mainly decided by the size of the crystallites/grain. For an individual grain of radius a , the capacitance of the grain is $\sim a$. The value of C_G is thus expected to increase as the average grain size increases. This is reflected in Figure 4.13 (b) where the film A with largest average grain size has the highest C_G and it decreases progressively as the average grain size decreases. Since this part of the capacitance is mainly determined by the size of grains, the gate bias V_g has essentially no effect on it.

4.7 Conclusion

Impedance spectroscopy of nanostructured ZnO films with different morphologies have been carried out in TFT configuration with EDL as gate dielectric. The induction of large surface charge in the film by EDL gate leads to large modulation of the complex impedance by moderate gate bias V_g . The observed data were explained as arising from control of the GB depletion layer and GB potential barrier by the field induced large charge density that leads to large change in C_{GB} as well as R_{GB} . The work carried out shows how the gate with EDL dielectric can be an enabling tool to control reversibly the complex impedance of a thin film. The investigation is not study of TFT device from the view point of device performances. However the lesson obtained from this experiment will have the implication on such TFT's. In particular, the control of the C_{GB} by gate bias has been shown in the chapter will allow control on the device response time as well capacitance.

Chapter 5

High performance flexible thin film transistor (Flex-TFT) based on highly textured ZnO film using electric double layer gate dielectric

Fabrication of ZnO based TFT on flexible substrate is very desirable thing for application. Since flexible TFTs are made on polymeric substrates, there is need for low temperature processing of ZnO. Research in low temperature processed flexible electronics using oxides suffer mainly from the limitations of the mobility of carriers in thin film. In spite of having higher mobility than a-Si and organic semiconductor, ZnO has serious draw back on low temperature chemically synthesis film due to its poor crystalline quality. Under low temperature chemical process, the film has low mobility and the TFT so fabricated has low ON/OFF current ratio, high subthreshold swing and high threshold voltage. To improve the performance of flexible thin film transistor, we have grown the good quality textured nanocrystalline film on flexible Kapton[®] substrate and utilized the EDL as gate dielectric. In this chapter, we have investigated the effect of EDL gate dielectric on highly textured nanocrystalline ZnO film

grown on the flexible substrate. We show that the ultra high carrier density accumulated at the surface by EDL gate bias produces high value of field effect mobility (μ_{FE}) ≥ 70 cm²/Vs as well as Hall mobility ≈ 100 cm²/Vs. This can bring down the operating voltage as well as the sub threshold swing and can lead to a high current switching ratio. While flexible TFT has been investigated before there very few reports of flexible TFT with EDL gate dielectric that show high performance as reported in this chapter.

5.1 Introduction

New and advanced form of electronics technology is light, thin and flexible circuit that can be attached to movable surfaces such as human skin. Oxide semiconductors are appropriate candidates for next generation of flexible thin film transistor (Flex-TFT) technology because of their high value of mobility compared to a-Si or organic semiconductors, high transparency, possibility of low temperature processibility and large area uniformity that can be achieved in solution process. TFT fabricated on flexible substrates at low processing temperature form an important component for electronic and optoelectronic applications such as wearable and stretchable electronic devices, flat panel displays and sensors [121–129]. These devices based on low cost plastic substrates have advantages such as low profile, small size and mechanical flexibility. Flex-TFT based on metal oxide semiconductors such as ZnO or InGaZnO (IGZO) have many advantages over those fabricated using materials like amorphous silicon or organic thin films as channels [124, 129–134]. Generally, fabrication of Flex-TFT with oxide channels use low temperature synthesis routes such as sol-gel or chemical solution deposition to make it compatible for flexible polymeric substrate.

Many attempts have been made to realize high performance Flex-TFT based on oxide semiconductors at low annealing temperature [122, 133–136]. In context to ZnO, which is the specific channel material used in this investigation, several groups have used different types of flexible substrates to realize the Flex-TFT based on solution grown nanostructured ZnO channels [123, 134, 137–142]. The low temperature processing has the limitation that it gives rise to poor crystalline quality of the film which in turn leads to low carrier mobility that limits the ON/OFF ratio as well as gives rise to large subthreshold swing (SS). Below we give an overview of published work in this area.

Song et. al. [137] fabricated ZnO TFT on polyimide (PI) substrate using SiO₂ as back gate dielectric. ZnO channel layer was grown by spin coating chemical process at temperature 200⁰ C. In this experiment, they reported that the value of saturation mobility, threshold voltage and ON/OFF current switching ratio were 0.35 cm²/Vs, 6.7 V, and ~ 10⁶ respectively. Another common method to protect the film from environment induced degradation is the surface passivation by oxide layers. Lin et.

al. [123] used TiO_2 passivation layer on ZnO film and enhanced the transistor performances. They employed the low temperature atomic layer deposition (ALD) to passivate the ZnO film. They fabricated flexible ZnO TFT using ALD deposited ZnO as a channel layer and $\text{Al}_2\text{O}_3/\text{HfO}_2$ as a gate dielectric. After passivation, there was no significant change in ON/OFF current ratio ($\sim 10^5$), V_{th} (2.4 V) and SS (0.4 V/dec.) but the value of field effect mobility slightly increased from 16 to 20 cm^2/Vs . Ion-gel electrolyte gated Flex-TFT on kapton tape was reported by Hong group [127], where the ZnO channel was grown by aerosol jet printing method [127]. They reported V_{th} and μ_{FE} are 0.97 V, and 1.61 cm^2/Vs respectively. Lee et. al. [140] in 2010 fabricated flexible TFT based on solution grown transparent ZnO film using PMMA as a gate dielectric. They studied the structural and electrical characteristics of the ZnO TFT with varying the concentrations of precursor solution (50 mM, 80mM, 110 mM) of ZnO. The different precursor concentrations produced different surface morphologies and grain sizes. They investigated the effect of grain boundaries on the performances of the Flex-TFTs. TFT fabricated with highest precursor concentration yielded the μ_{FE} of 7.5 cm^2/Vs under high source drain bias ($V_{ds} = 20$ V). Values of V_{th} , ON/OFF current ratio and SS were 5.4 V, $\sim 10^4$ and 2 V/dec. obtained respectively. Wang et. al. [141] fabricated Al doped ZnO TFT on flexible polyethylene terephthalate (PET) substrate using two different carrier density layers of ZnO which was achieved by varying oxygen pressure. The performance of the device was increased with stacking the double layers. The value of field effect mobility was increased from 3 to 30 cm^2/Vs in double layer device with reducing the sub threshold swing from 0.46 to 0.33 V/dec. Zhao et. al. [139] reported TFT characteristics based on ZnO film on kapton tape as a flexible substrate. The film was grown by plasma-enhanced atomic layer deposition at 200⁰ C and Al_2O_3 was used as a gate dielectric. In this report, field effect mobility, threshold voltage and subthreshold swing of 20 cm^2/Vs , 2 V and 350 mV/dec. respectively and current ON/OFF ratio of $\geq 10^7$ achieved.

Most of reports in flexible TFT used the conventional metal oxide as gate dielectric that can only operate at high gate voltage and also produce low carrier mobility. To improve the transistor performance many authors used IGZO and IZO as a channel material. Liu et. al. [143], Park et. al. [144], Jeong et.al. [134] etc., described the performances of the flexible thin film transistors based on IGZO. Most of

these efforts on Flexible substrates did not yield a field effect mobility more than $20 \text{ cm}^2/\text{Vs}$ and often a large SS value more than 200 mV/dec. or even more.

The conventional metal oxide get dielectrics require higher deposition temperature $\geq 400^\circ$ which are not suitable for low temperature polymer substrates. In this experiment, we use polymer electrolyte to fabricate the flexible TFT. Here, we discuss the performance of the Flex-TFT fabricated from PLD grown highly textured ZnO nanostructured film using EDL as gate dielectric. The performance parameters are carrier mobility, threshold voltage, ON/OFF current ratio and subthreshold swing. In oxide based TFT, when conventional oxides are used as gate insulator, the threshold voltage V_{th} is often very high and can be tens of volts unless the gate dielectric is too thin. In this investigation the EDL at the gate formed by the polymeric electrolyte as a gate dielectric leads to very large carrier accumulation at the surface of the channel at a low gate voltage ($\Delta n_s \geq 10^{13}/\text{cm}^2$ for a gate bias of 1 V). The performance of the flexible TFT has been improved by using EDL gate dielectric. As we have earlier described in section 3 and 4, EDL gate bias modulate the defect distribution as well as the GB barrier that we have utilized to improve the characteristic of Flex-TFT. Other important physical origin of the high performance is oriented (textured) nature of the ZnO film used as channel. Coherent nature of GB in this textured film is crucial for giving high mobility.

5.2 Fabrication of flexible thin film transistor

The highly textured ZnO thin film used in this study was grown by pulsed laser deposition (PLD) technique on a flexible polyimide tape commonly available as Kapton[®]. During the PLD growth the tape was fixed on a glass backing. The film deposition was done using KrF excimer laser ($\lambda = 248 \text{ nm}$) and ZnO (99.9%) target at an oxygen atmosphere of $1.3 \times 10^{-3} \text{ mb}$. The film was characterized by X-Ray Diffraction(XRD), Atomic Force Microscopy (AFM) and Photoluminescence (PL) measurement. The film thickness was determined by ellipsometry. Typical film thickness used was $\approx 100 \text{ nm}$ (Measured by ellipsometry Figure 2.15 (b)).

The atomic force microscopy (AFM) image (Figure 5.1 a) shows that average diameter of the grain is

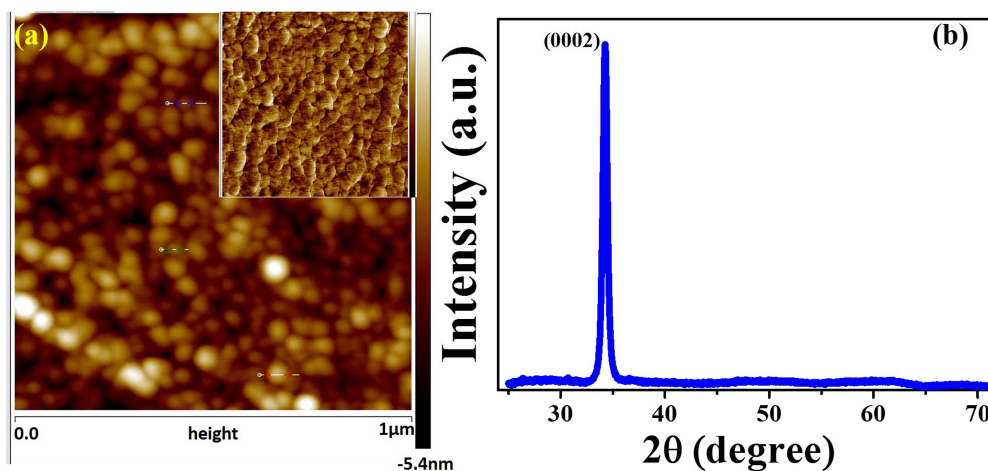


Figure 5.1 (a) AFM image and (b) XRD pattern of nanostructured ZnO film.

close to 30 nm with root mean square roughness of the film of about 2 nm. Lateral force microscope mode image (inset in figure 5.1 (a)) shows a dense growth pattern of the nanograins. The XRD pattern of the film (Figure 5.1 (b)) shows only one peak along (0002) direction indicating the highly textured nature of the film with c- axis perpendicular to the substrate. The photoluminescence (PL) spectra (Figure 5.2) of the oriented film has a sharp band edge peak around 375 nm and a broad small peak around 500 nm, which in ZnO originate from defects like charged oxygen vacancies. The ratio of the intensities between UV to visible ($I_{UV}/I_{visible}$) is ≥ 8 , which shows that the visible emission intensity is much lower than that of the band edge emission, indicating reasonable good quality of the film with low defect oxygen vacancies.

The Flex-TFT with effective channel length of 4 mm and width of 1 mm were fabricated in Hall bar geometry (Figure 5.3) with contact pads of Au/Cr (100 nm/10 nm) made by thermal evaporation. Electrodes (source and drain) were covered by thick layer of PMMA to avoid contact between the source and drain electrodes and gate electrolyte. PEO/LiClO₄ in 10:1 was dissolved in methanol to make the electrolyte in gel form and applied to the exposed region of the channel which further solidified as a polymer layer before used. A thin aluminium foil was used as the gate electrode.

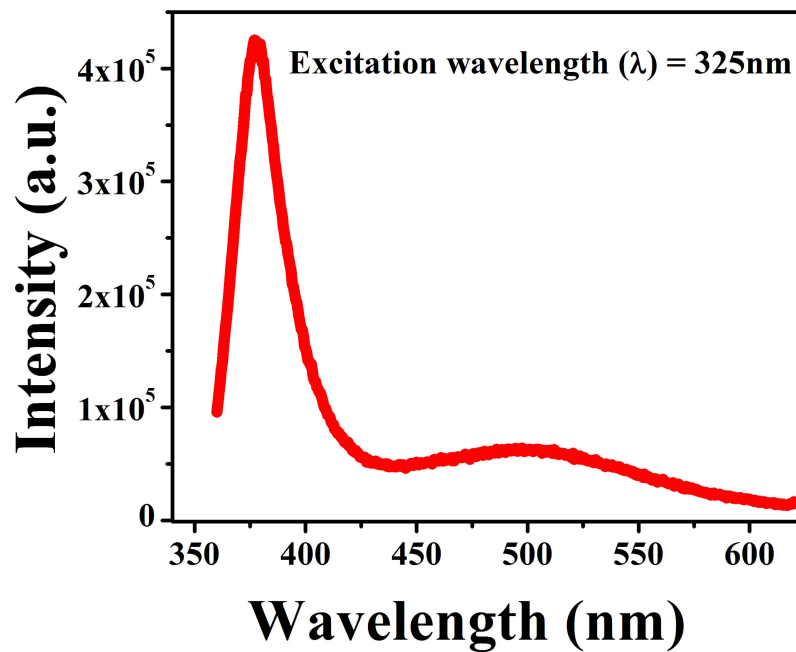


Figure 5.2 PL spectra of nanostructured ZnO film.

5.3 Sheet resistance, carrier density and Hall mobility measurement

To determine the carrier concentration and the mobility of carriers, Hall measurements were performed on the ZnO channel with different gate bias in the Hall bar geometry as shown in Figure 5.3. This allows us to measure the induced charge in the ZnO channel. The Hall voltage ($V_H = V_1 - V_3$) was measured at constant current ($I = 100 \mu\text{A}$) supply at room temperature with varying the magnetic field (B). The V_H as a function of the B varying from 0 to -4 T is shown in inset of Figure 5.4 in log scale for different gate bias. The induced surface charge carrier (Δn_s) at the surface of semiconducting channel for different gate bias has been calculated from the Hall data, along with the Hall mobilities (μ_H). The value of Hall coefficient (R_H) and the incremental carrier concentration Δn_s are calculated using the following equations:

$$R_H = \frac{V_H t}{IB} \quad (5.1)$$

$$\Delta n_s = -\frac{1}{R_H e} \quad (5.2)$$

Where t and e are sample thickness and value of the elementary charge respectively. Δn_s at a gate bias

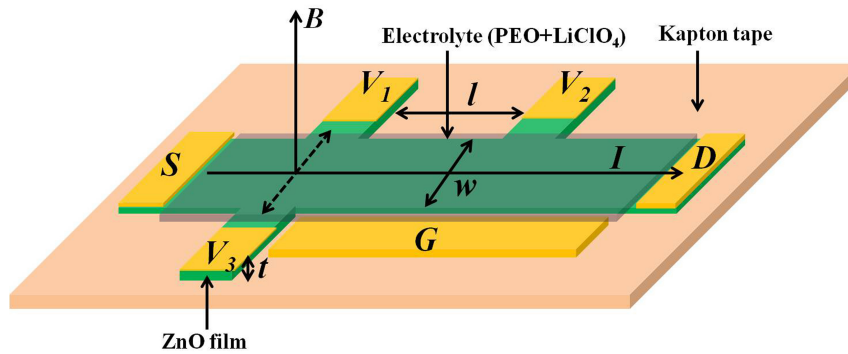


Figure 5.3 Schematic diagram of Flex-TFT in Hall bar geometry where l , w and t represent the channel length, width and thickness respectively.

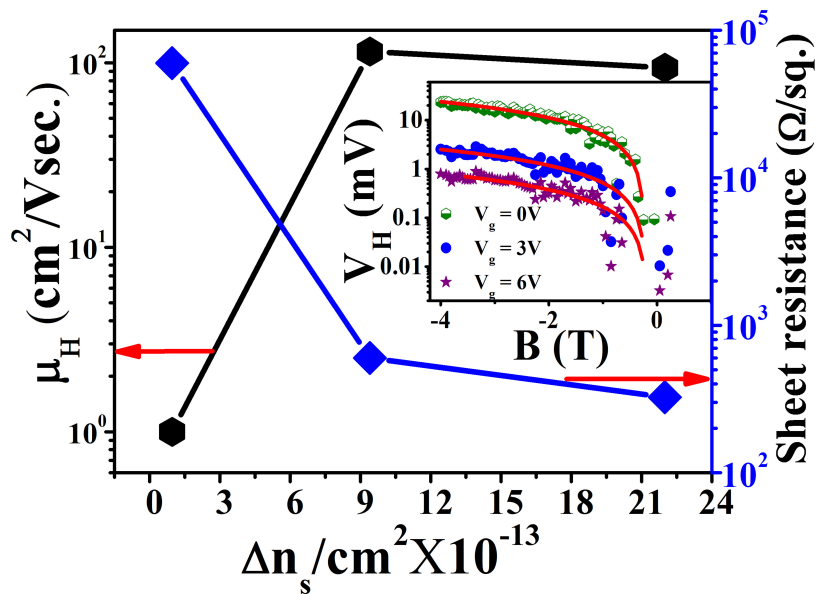


Figure 5.4 Dependence of Hall mobility and sheet resistance on carrier concentration. Inset shows the Hall voltage vs. applied magnetic field.

of 3 V is $\simeq 1 \times 10^{14} \text{cm}^{-2}$, which is appreciable induced surface charge density at a low bias.

Figure 5.4 shows that the dependence of μ_H and the sheet resistance R_s of the channel with induced surface charge density. The value of μ_H increases appreciably with increasing gate bias. It changes from nearly 1-2 cm^2/Vs at zero gate bias to a saturation value of $\approx 100 \text{cm}^2/\text{Vs}$ for a gate bias of 3 V. This large rise in the Hall mobility is a crucial factor in the sharp turn on of the TFT which is discussed later on. ZnO Hall mobility in single crystals and epitaxial films often lie between few tens to 100

cm^2/Vs . Thus the nanostructured textured film of ZnO grown on the flexible substrate can reach high Hall mobility value where surface charges are induced on it.

The sheet resistance of the channel having length (l) and width (w) is determined using the longitudinal voltage $V_x = V_1 - V_2$ as follow.

$$R_s = \left(\frac{V_x}{I}\right) \times \left(\frac{w}{l}\right) \times s \quad (5.3)$$

where s is the number of square in Hall bar (3 in our case). Figure 5.4 also shows that the sheet resistance (R_s) of the sample decreases with increasing carrier concentration. R_s of the ZnO channel decrease from 60 $\text{K}\Omega$ to about 0.3 $\text{K}\Omega$. Interestingly, the value of R_s at zero gate bias is $\geq h/e^2$ which is the Thouless maximum metallic resistance value [145] and at gate bias of 3 V the sheet resistance is $\leq h/e^2$, indicating a likely gate induced metal-insulator transition in the ZnO channel, which has been observed in epitaxial films [28] and single crystals [90] before. We will see below that high mobility of the film grown by the PLD (in comparison to other low temperature methods) leads to enhanced performance of the Flex-TFT even at a low gate bias.

The highly oriented nanostructured ZnO film, that constitutes the channel, consists of densely packed arrays of grains. At zero bias $\mu_H \sim 1 - 2 \text{ cm}^2/\text{Vs}$. Though it is not very large but is high compared to the μ_H most observed in polycrystalline or nanocrystalline ZnO films. This enhancement arises from the textured nature of the film, which gives rise to coherent GBs thus reducing the grain boundary barrier ϕ_{GB} . This enhances the overall charge mobility in the film. This is an important factor which adds to the enhanced performance of the TFT as well.

5.4 Performance of flexible thin film transistor (Flex-TFT)

Figure 5.5 shows that the transfer curves of the device (i.e. the drain-source current I_d as a function of the gate voltage V_g). The important performance characteristics achievable in Flex-TFT are contained in this graph. For the data shown in the figure, drain-source voltage $V_{ds} = 1 \text{ V}$ and the gate voltage (V_g) was varied in the range of -1 to 2.5 V. The I_d increases as V_g is increased till it saturates for $V_g \geq 2.5 \text{ V}$

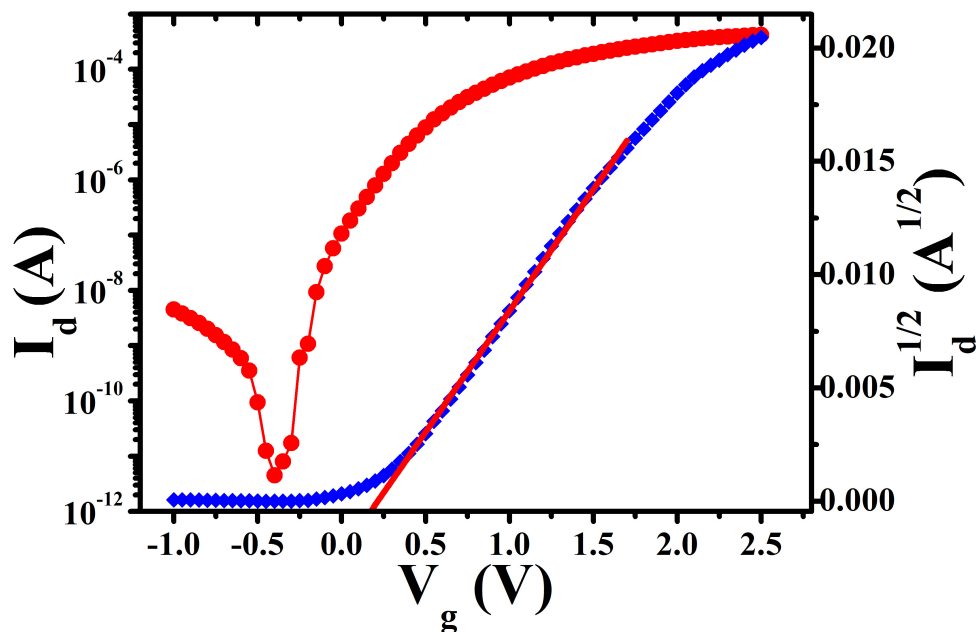


Figure 5.5 Transfer characteristic of ZnO Flex-TFT.

to a value of nearly 0.4 mA. The increase of I_d with positive V_g is expected of a n-type channel. The OFF state current of the device is close to 10 pA. The ON/OFF current ratio (I_{ON}/I_{OFF}) at $V_{ds} = 1$ V is thus $\geq 10^7$, a very high performance index that have not been reported in flexible ZnO based TFT before [123, 130, 137, 140]. High performance oxide based TFT behavior with ON/OFF ratio $\approx 10^5$ - 10^7 , have been fabricated with ITO, IGZO channels and proton conducting EDL as gate dielectric. However, these have been made on non-flexible substrate [146–148]. In some reports, flexible TFTs with ion gel as gate dielectric [127, 149] show ON/OFF ratio nearly 10^5 . In Figure 5.5 we also show a plot of $I_d^{1/2}$ vs V_g . From the data the field effect mobility μ_{FE} of the channel and the threshold voltage V_{th} of the TFT have been calculated using the following conventional equation for a field effect transistor.

$$I_d = \mu_{FE}(wC_i/2L)(V_g - V_{th})^2 \quad (5.4)$$

Where, L and w are length and width of device and C_i is the specific gate capacitance. C_i has been obtained from the charging time of the gate in response to a step change in gate bias as described before in chapter 3.

Figure 5.6 shows the output characteristics of the Flex-TFT. The drain current first increases linearly

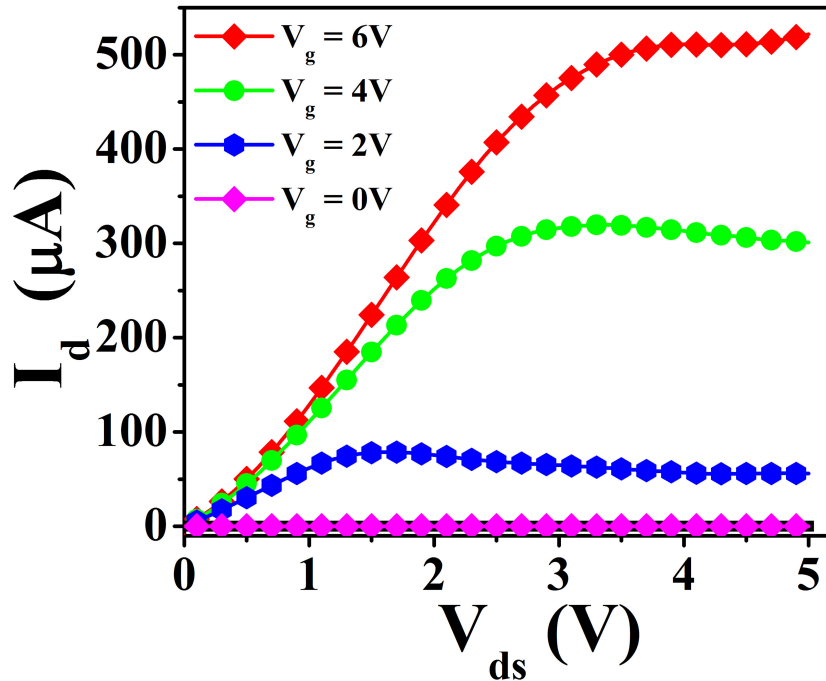


Figure 5.6 Output characteristic of ZnO Flex-TFT.

and saturates at higher drain source (V_{ds}) bias which match with the basic output characteristics of the TFT.

One of the important aspect for TFT with EDL as gate dielectric, is the nature of the gate. The static gate current I_g was found to be about 3 orders less than the drain current I_d ensuring a proper electrostatic behaviour where charges in channel are induced by field effect. We have measured the transient response of gate current (I_g) for a step change of the gate bias (Figure 5.7). The study of gate charging in response to a step-change in voltage in a gate with EDL dielectric has been discussed by us before in section 3.5. From the exponential decay of the gate current, the charging time constant τ_g has been obtained. We obtain the total gate resistance (R_g) by using the maximum gate current at the onset of charging the gate capacitor with a given bias. The value of the gate capacitance $C_g = (\tau/R_g)$. The specific gate capacitance (C_i) is calculated from C_g by using the gate area ($=wL$). For the devices used here, the value of $C_i \approx 3 \mu F/cm^2$. The value of R_g is $\approx 90 M\Omega$, which is much larger than the sheet resistance of the channel.

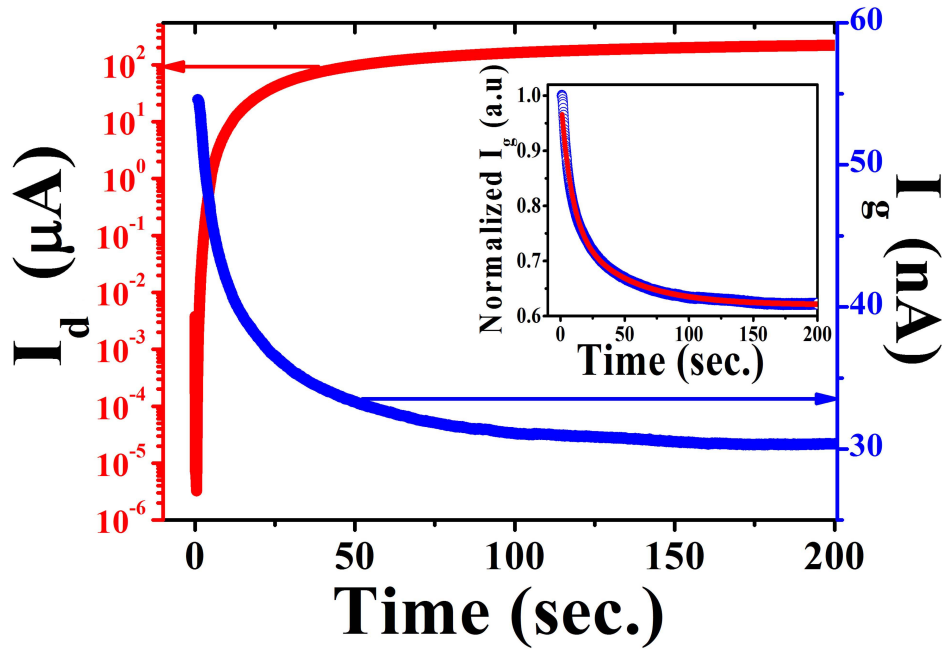


Figure 5.7 Transient response in step bias of gate voltage.

Another important performance parameter of the TFT is the subthreshold swing (SS) defined as $S \equiv \left[\frac{\delta \log I_d}{\delta V_G} \right]^{-1}$, which has been calculated from the data for $V \leq V_{th}$ shown in Figure 5.5. For the devices with the ON/OFF ratio 10^7 the SS value is around 95 mV/dec. This compares well with oxide based non-flexible TFT's with that can show $SS \approx 100$ mV/dec [150]. A lower value of SS ensures sharp turn-on on switching.

Table 5.1 compares the characteristics of some reported Flex-TFT with our device. The large ON/OFF ratio and the relatively small SS seen in our TFT, originates predominately from the high mobility of nanostructured ZnO film, which is rather substantial when compared with most reported nanostructured or polycrystalline ZnO film. It is also noted that with positive gate bias as more electrons are induced into the channel this enhanced the mobility substantially. We have shown in previous chapter (chapter 3) that such a phenomena can occur when induced electrons passivate a part of charged defect states that act as scattering centres. To ensure that the device performance indeed depends on the film mobility, we tested the TFT characteristics on films that have been fabricated by changing some of the deposition conditions (oxygen pressure). This leads to a change of the field effect mobility. In Figure 5.8 we plot

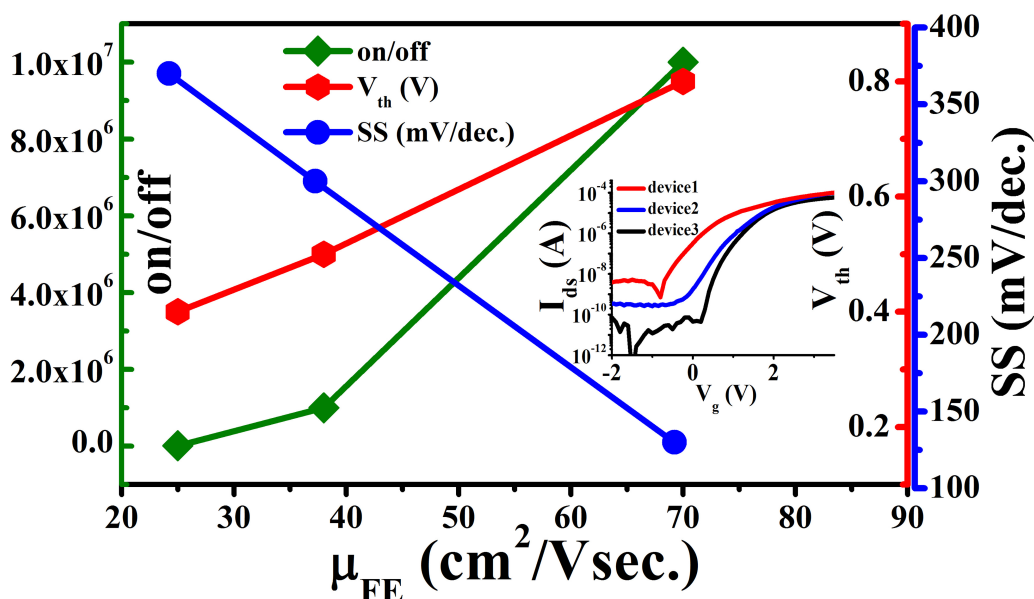


Figure 5.8 Dependence of TFT performance parameters (ON/OFF, V_{th} , SS) with μ_{FE} .

the dependence of the performance indices ON/OFF ratio, V_{th} , and SS on the field effect mobility μ_{FE} of the ZnO in the channel. In all the devices the saturation current is close to 0.10 mA (inset of Figure 5.8) for $V_{ds} = 1$ V. The figure clearly shows that a small change of μ_{FE} can change the ON/OFF ratio by orders of magnitude and it also affects the SS significantly. Interestingly, reduction of μ_{FE} reduces the V_{th} . This graph gives us an important information that the largest switching ratio and smallest SS are obtained in the film with largest R_s and highest carrier mobility. This can be explained from the fact that the charged oxygen vacancy in the ZnO acts as a source of scattering as well as a source that contributes carriers in the conduction band. Balance of these two opposing factors determine the charge transport quality in the films. For a film with larger R_s , the resistance is high due to less number of carriers which in turn arise due to relatively less number of ionized defect sites. This gives a larger R_s but leads to higher mobility. The large switching ratio thus arises from a lower OFF state current. This may be seen from inset of Figure 5.8. For films with less R_s , the OFF state current is higher due to larger contribution of charge carriers from more ionized defects, which in turn act as scattering centres that reduce the mobility. The lower R_s , and larger carrier density also brings down the value of V_{th} in these films. Figure 5.8 summarizes the basic underlying physics of the ZnO channel and the parameters

Table 5.1 Characteristic of ZnO Flex-TFT: field-effect mobility (μ_{FE}), subthreshold swing (SS), threshold voltage (V_{th}), and ON/OFF ratio.

Oxide semi- conductor	Gate dielectric	μ_{FE} (cm^2 /V.s.)	V_{th} (V)	ON/ OFF	SS mv/dec.	Refe- rences
ZnO	$\text{Al}_2\text{O}_3/\text{HfO}_2$	20	2.4	10^5	380	[123]
ZnO	SiO_2	0.35	6.7	10^6	-	[137]
ZnO	Al_2O_3	20	2	10^7	350	[139]
ZnO	PMMA	7.5	5.4	10^4	2000	[140]
IGZO	Y_2O_3	8.3	-	10^3	-	[132]
IGZO	SiN_x	15	0.8	10^8	400	[151]
ZnO	EDL	70	0.2	$\geq 10^7$	~ 95	[our device]

that need be optimized to get a high performance from these Flex-TFTs.

The highly oriented nanostructured ZnO film that constitutes the channel, consists of densely packed arrays of grains. At zero bias $\mu_H \sim 1.5\text{-}2 \text{ cm}^2/\text{Vs}$. Though it is not very large but is high compared to the μ_H in most polycrystalline ZnO film. This enhancement arises from the textured nature of the film, which gives rise to coherent GBs thus reducing the grain boundary resistance which enhances the overall charge mobility in the film. This is an important factor which adds to the enhanced performance of the TFT as well.

The performance of the TFT depends largely on how the large charge induced by the gate with EDL gate insulator tunes the transport in the film. In Figure 5.4, shows the result of change in the Hall mobility as the gate bias is changed. It shows that a change in the gate bias by about 3 V, μ_H changes by more than a factor of 50. The predominant cause of the change in the film conductance thus arises from a change in the μ_H . The role of large induced charge in bringing about a change in mobility is the passivation of cross-sections of the charged oxygen vacancies that act as scattering centres. The reduced charged scatterers bring about an enhancement of the mobility. The reduction in the charged

oxygen vacancy centres also reduce the intensity of PL spectra in visible region which is discussed in section 3.6 [114].

In a nanostructured film used here, there is a large contribution of the depleted grain boundaries (GB) that creates a barrier ϕ_{GB} at the grain boundary to electronic transport reducing the mobility. Induction of large charge density of majority carriers that passivates the charged defects reduces the depletion layers at the GBs thus reducing the barrier ϕ_{GB} created at the GBs. A direct proof of the model of TFT action in ZnO, that the depletion in GB can be changed effectively by charge induction using gate with EDL dielectric has been given by measurement of the GB capacitance as discussed in chapter 4. It has been shown that change in gate bias from 0 V to 3 V can change the GB capacitance by at least one order. The grain boundary capacitance $C_{GB} \sim N_s^{-1}$, where N_s is the charged acceptor surface density at the GB surface [120]. Passivation of charged defects by induced charge reduces N_s leading to enhanced C_{GB} . This also reduces significantly ϕ_{GB} due to its quadratic dependence on N_s [152]. The performance enhancement of the TFT thus depends largely on the specific nature of the GB of the film that the depletion layer at the GB can be controlled by the charge induced by the gate. In this respect, the ZnO TFT operation differs qualitatively from a conventional MOSFET [153]. It may be that this gate induced control of depletion at the GB may be the underlying model of TFT in many oxide TFT's. The efficacy of EDL as gate insulator is related to the large carrier density induced by them that can effectively control the carrier transport.

The reduction of V_{th} to sub 1 V region, which is an attractive feature because, it can be used directly with battery operated systems that utilize Li ion batteries (operating voltage 3.6 V/cell). The principal cause for reduction of the V_{th} arise due to the nature of the gate dielectric. Use of the polymeric gate dielectric leads to formation of the EDL at the channel, electrolyte interface, which in turn leads to large specific gate capacitance $C_i \approx 3 \mu\text{F}/\text{cm}^2$. The field effect, due to large C_i , induces a surface charge of $(\Delta n_s) \approx 1.2 \times 10^{13} / \text{cm}^2$ by 1 V gate bias. Accumulation of such a large induced surface charge brings down the threshold voltage of the TFT to sub 1 V range. There is another aspect of the polymeric gate which also adds upto to large inter-facial charge accumulation. The polymeric gate makes an all-around-gate structure, that occurs during the solidification process of the polymeric gate

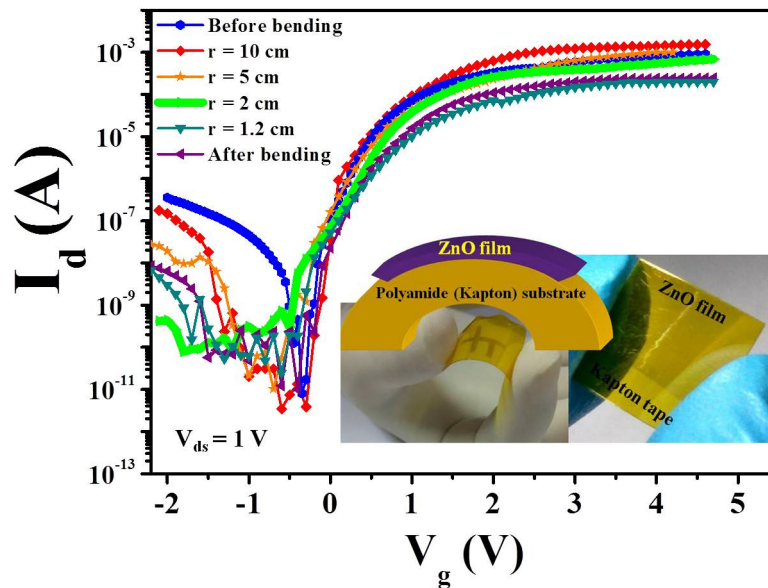


Figure 5.9 Transfer characteristic of Flex-TFT in convex bending of different radius.

when it can flow around, conformally covering the channel surface as well as voids in the channel. This helps in reducing effect of surface roughness.

The results presented above clearly establish, that a Flexible TFT can be fabricated on a polyimide substrate like Kapton® on which a textured nanocrystalline film of ZnO can be grown by PLD that exhibit high electron mobility (both Hall and Field effect), which are much larger than those grown on Flexible substrates by sol-gel or chemical deposition. The high mobility ensures that the flexible TFT fabricated from the ZnO film with EDL as gate dielectric shows very large ON/OFF ratio (10^7) on switching, a relatively small subthreshold swing (~ 100 mV/dec.) and a sub 1 V threshold voltage.

5.5 Bending results

To check the operational stability of Flex-TFT on bending, we have measured the transfer characteristic of the device for different bending radius (10 cm, 5 cm, 2 cm and 1.2 cm) (Figure 5.9). The bending

position of ZnO film on kapton tape is shown in inset of figure 5.9. There is no significant change in V_{th} , μ_{FE} and SS of the device under convex bending (tensile strain) of radius of curvature ≥ 1.2 cm. The significant change in current On/OFF ratio is observed only below the radius ≤ 1.2 cm. This observation says that the device can be operated safely under bending condition with radius of curvature ≥ 1.2 cm. Table 1 shows the change in performance parameter with changing the bending radius of the device. This observation suggests that the device can be operated safely under bending condition with radius of curvature ≥ 1.2 cm.

Table 5.2 Change in performance parameters with bending radius.

Bending radius cm	$\sim \mu_{FE}$ ($\text{cm}^2/\text{V.s.}$)	$\sim V_{th}$ (mV)	ON/OFF mv/dec.	$\sim \text{SS}$
Before bending	70	200	10^7	90
10	70	200	10^7	90
5	70	200	10^7	125
2	66	200	10^7	125
1.2	60	200	10^6	125
After bending	65	200	10^6	125

5.6 Conclusion

Using conventional oxide gate dielectric in Flex-TFT, it is insufficient to modulate the large carriers in functional oxide which results the high threshold voltage as well as large SS. Instead of oxide gate dielectric, the EDL gate dielectric can induce the ultra high carrier density ($\Delta n_s > 10^{13}$ near the surface of the channel). These large number of carriers can enhance the field effect mobility by reducing the distribution of the defect states and GB barrier. The enhancing the mobility leads to drastic reduction of threshold voltage, SS with high ON/OFF current ratio that determine the high performance of the Flex-TFT based on a flexible substrate like Kapton[®]. We also found that the device can operate suc-

cessfully with a bending radius down to 1.2 cm.

Chapter 6

A high performance ZnO nanowire film based broadband photo-detector fabricated with ligand free plasmonic Au nanoparticles synthesized by pulsed laser ablation

The enhanced light matter-interaction by coupling of ZnO nanostructured with plasmonic nanoparticles can be utilized for broad band photodetection. A novel idea based on pulsed laser ablation in liquid medium is utilized for decoration the plasmonic nano particles on ZnO nanowire surface. The responsivity of Au-NP below a wavelength of 500 nm reaches 10 mA/W and reaches a saturation value close to 0.5 A/W for $\lambda < 400$ nm. In the longer wavelength range the responsivity stays at around 0.1 mA/Watt for λ close to 600 nm. The photo-active Au-NP decorated ZnO NW film has been made by a single step method using pulsed laser ablation of Au target in a liquid medium that leads to attachment of Au-NP to ZnO nanowires. It has been found that the attachment of Au-NP also makes the relaxation

of the photo current considerably faster when the illumination is turned off. The enhancement of the photo detection capability was found to be strongly linked to the enhancement of the absorption over a broad spectral range on Au-NP attachment. It has been proposed that plasmonic property of the Au-NP which enhances the absorption for wavelengths ≤ 600 nm is responsible for the enhanced performance of the photo-detector through creation of substantial amount of electron-hole pair which can directly or indirectly populate the conduction band of ZnO

6.1 Introduction

ZnO is widely used as an UV photo-detector [4, 19]. However, one of the drawbacks of ZnO based photo-detectors is its lack of response in the visible, in particular above a wavelength $\lambda \geq 450$ nm. This fundamental limitation of ZnO (as well as that of similar oxides with wide band gap) arises from the fact that its bandgap lies in the UV (≈ 3.3 eV). This limits the use of ZnO significantly in broad band photo-detection, particularly in the visible spectrum. ZnO based photo-detectors have an edge over other elemental or complex semiconductor photo-detectors that it is easy to fabricate and it is extremely cost effective. Removal of this road block and extending its operation in broader wavelength range will be a significant progress in its application potentials.

One of the ways ZnO photoactivity in the visible can be enhanced by increasing the sub-band gap defect states that correspond to energy ranges from 500 nm to 600 nm. This enhances the absorption of ZnO at longer wavelengths [154, 155]. However, enhancing the photo-response by increasing sub-band gap defects is not a viable option for enhancing photo response, because such defect states decrease significantly the charge mobility leading to reduction in light generated current. The alternative that has been utilized in this report, is use of small plasmonic Au nanoparticles to decorate/functionalize the ZnO nanowire photo detectors that leads to a significant absorption in the visible in addition to enhancing its absorption in the UV. Such enhancement of absorption of light leads to performance enhancement in the photo-conductive response of ZnO by extending its range of operation upto a wavelength of ≥ 600 nm as well as enhancing its UV response significantly. It also leads to significant lowering of the decay constant of the photo-current when the illumination is turned off, thus making the response faster, which is otherwise slow in case of ZnO photo detectors.

In general, the Au-NP, particularly those synthesized by solution route needs stabilizing ligands or dispersing medium. It has been observed that this influences the surface plasmon resonance and also weakens the interband transition which plays a detrimental role for photoresponse [156]. It will be thus important to have a synthesis route that would lead to enhancement of the optical absorption as well as photocurrent response utilizing the plasmonic of Au NP over a wide range without interfering effects

of ligands. In this chapter, we have proposed a physical method by which semiconducting nanowires (of any material) can be decorated by plasmonic nanoparticles (average diameter ~ 10 nm) in a single ligand free step where the coverage of the Au-NP can be controlled with ease. The ligand free physical process uses pulsed laser ablation (PLA). The attachment process is carried out by laser ablation of the Au target in a liquid medium like water where NWs are suspended or kept on a substrates. We can control the coverage of the attached Au nanoparticles that are uniformly attached to the surface of the nanowires. We have showed that the process of ligand free Au-NP attachment to surface of ZnO nanowires (NW) results in significant decrease of the dark current, increase in photo response both in UV and visible region. We also found that attachment of the Au-NP leads to faster relaxation of the photocurrent.

Enhanced photoresponse both in UV and visible region (with responsivity R reaching > 0.1 mA/W even at a wavelength of $\lambda = 600$ nm, deep in visible and increasing significantly to 4×10^2 mA/W at shorter wavelength $\sim \lambda = 375$ nm), a decrease the persistence of the photocurrent in Au-ZnO NW films due to significant shortening in decay time. The responses of the Au decorated ZnO NW films strongly depend on the surface coverage of the nanowire by plasmonic Au nanoparticles which in turn can be controlled by varying the number of laser shots.

The decoration of ZnO nano wires by plasmonic nanoparticles is an useful & effective technique to change the surface and interface behaviour of the materials which can control the electronic transport properties in ultraviolet (UV) [157–161]. It has been established that the physical properties of the ZnO nanowires can be tuned by surface attachment with plasmonic nano particles of Au, Ag, Pt, Pd etc. [157, 158, 162–166]. Vapor phase grown ZnO single nanowire photo-detector with solution deposited Plasmonic Au NP (diameter 30nm) have been reported [157] before. In the UV range $\lambda = 350$ nm the Au attachment leads to decrease of the dark current by nearly 2 decades and enhancement of gain by a factor of 500. The attachment also leads to shortening of the photocurrent decay time by a factor of nearly 30. However, no enhancement in the visible range has been reported. A very recent work Gogurla et. al. [158] reports similar enhancement of UV response in Au decorated ZnO nanosheets, where the Au was deposited from HAuCl_4 by prolonged UV exposure followed by oxygen

annealing at 600⁰ C that leads to formation of Au NPs with diameters ranging from 10-50 nm. They report a high photoconductivity which they infer arise from large built-in electric field at Au-ZnO junction. The Au decorated ZnO nanosheets show enhanced absorption in the visible (with contribution from plasmonic band) but the photoresponse is limited primarily in the UV region. The optical gain in the UV gets enhanced by a factor of nearly 10-15. Responsivity of ~ 60 mA/W has been achieved at $\lambda = 330$ nm. However this has been decreased to below 1 mA/W at $\lambda \geq 360$ nm. p-Si/n-ZnO nanorod heterojunction photo-detector with enhanced performance enabled by Au-NP surface plasmon resonance has been reported [167]. The photo-detector shows enhanced responsivity in the UV ($\lambda = 350$ nm) but it falls significantly at longer wavelengths.

The work discussed in this chapter has the novelty that the Au-ZnO NW photo-detector not only shows significant enhancement in photo response (~ 0.4 A/W) in UV but it has even higher enhancement (nearly four order) in visible range of the spectrum (≥ 475 nm) than the bare ZnO NW photodetector. We have shown that the problem of slow response in ZnO photo-detector can be significantly mitigated by the attachment of the Au-NP, which brings down the decay time of the photo-current. We also suggest that the process of enhancement of performance in the visible is linked to charge transfer between ZnO and the plasmonic nanoparticles. This work also establishes a simple one step ligand free attachment of Au-NP on nanowire surface using PLA in liquid medium.

6.2 Decoration of ZnO nanowire by plasmonic Au nanoparticles and fabrication of photodetector

The ZnO nanowire films, used in this work, were grown by hydrothermal method [168] from a solution of zinc nitrate hexahydrate and hexamethylenetetramine on ZnO nanoparticle seeded quartz substrate using an auroclave. The decoration of the plasmonic Au nanoparticles is done using vacuum free pulsed laser ablation in liquid medium like water. The experimental details for the nanowire synthesis and decoration of plasmonic nanoparticles are explained in chapter 2. Standard characterization tools

like X-ray diffraction (XRD), Scanning Electron Microscope (SEM), and High Resolution Transmission Electron Microscope (HRTEM) have been used to characterize the films.

6.2.1 Structural characterization of the Au-ZnO NW films

In Figure 6.1 (a) we have shown FESEM image of the undecorated ZnO NWs. The diameters of the nanowires vary from ≈ 30 to 70 nm and the length lie within the range ≈ 500 nm to $1 \mu\text{m}$. The SEM images in Figure 6.1 (b), (c) and (d) show the Au decorated ZnO nanowires where the Au deposition have been made with at 4,000 (4K), 8,000 (8K) and 16,000 (16K) laser shots. (A film with Au-NP coverage made with 16K pulses is named as Au-ZnO-16K and similar for other films). With variation of laser shots (4K-16K), the area coverage of the Au nanoparticles (Au-NP) on ZnO surface increases. The average size of the nanoparticles is ≈ 10 nm.

Figure 6.2 (a) shows the X-ray diffraction pattern of the ZnO NW films grown on quartz substrates. The films are strongly textured along (002) direction. There are also other small peaks in the XRD pattern corresponding to other indices showing that the film grown is not completely textured because all the wires are not vertically aligned. Along with the lines from ZnO, for films with sufficient Au-NPs coverage, four additional peaks associated with Au are also observed (shown in Figure 6.2 (b) and (c)). These peaks at indices marked as (111)*, (200)*, (220)* and (222)* belong to FCC metallic Au nanoparticles. The intensity of the Au- peaks increase with increasing Au coverage.

The high resolution transmission electron micrograph (HRTEM) image of the ZnO NW with the Au-NP (see Figure 6.3) shows two types of cross linked fringes, one related to ZnO (lattice spacing 0.26 nm) and other to Au (lattice spacing 0.25 nm). The HRTEM image shows that there is no diffusion of Au into ZnO and the interface between them is free of other materials.

6.2.2 UV-Visible absorption of the Au-ZnO NW films

To enhance the performance of ZnO with Au NP decoration, it is essential that the UV-Visible absorption changes substantially by decorating ZnO surface with Au NPs. In Figure 6.4, we show the optical

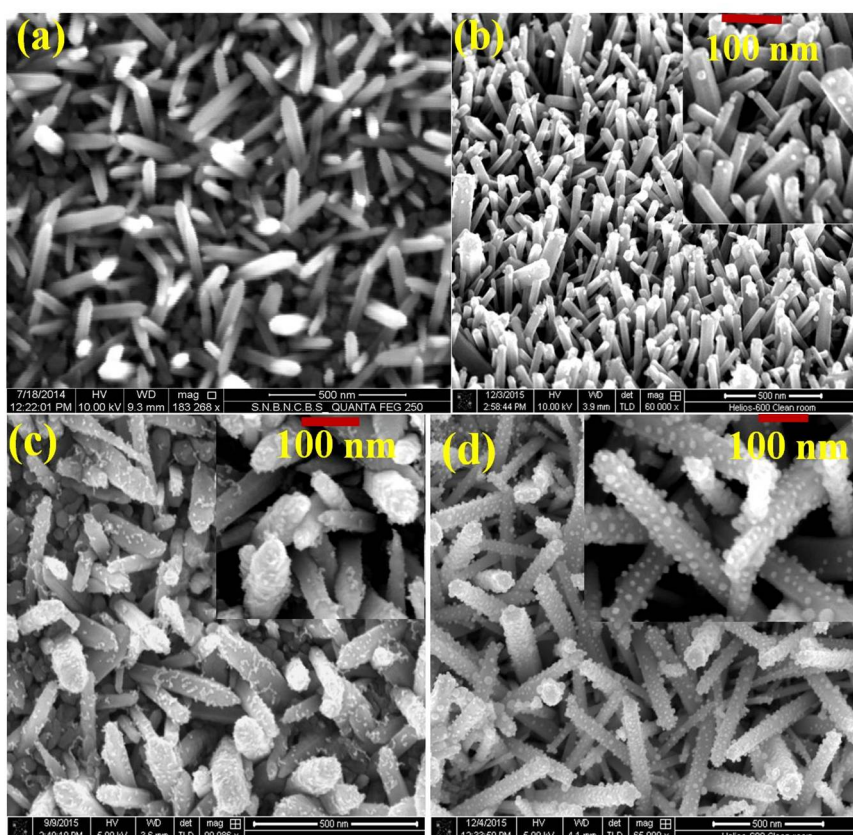


Figure 6.1 SEM images of (a) bare - ZnO nanowire film and (b)-(d) Au-NP decorated NWs with 4,000 (c) 8,000 and (d) 16,000 laser pulses. Increasing number of laser shots lead to increase of Au-NP coverage.

absorption spectra of both bare and decorated ZnO NWs films with different Au NP coverages in the conventional linear scale. Inset in Figure 6.4 the absorbance is plotted in log scale to show the large change that occurs in the absorbance of Au-ZnO NW film compared to that of the bare film. This also accentuates the changes that happen even at low absorbance region of the absorption spectra at visible range. The important observation is that the attachment of the Au-NP leads to a large change in the absorbance over a large wavelength range. The spectrum of the bare ZnO NW film shows the usual strong absorption edge at 375 nm which corresponds to the band gap absorption of ZnO. The kink in the absorbance data (marked by an arrow in inset Figure 6.4) close to $\lambda = 420$ nm can be seen in the data for all the samples. This is the region where there is a rapid change in the absorbance as the band-edge

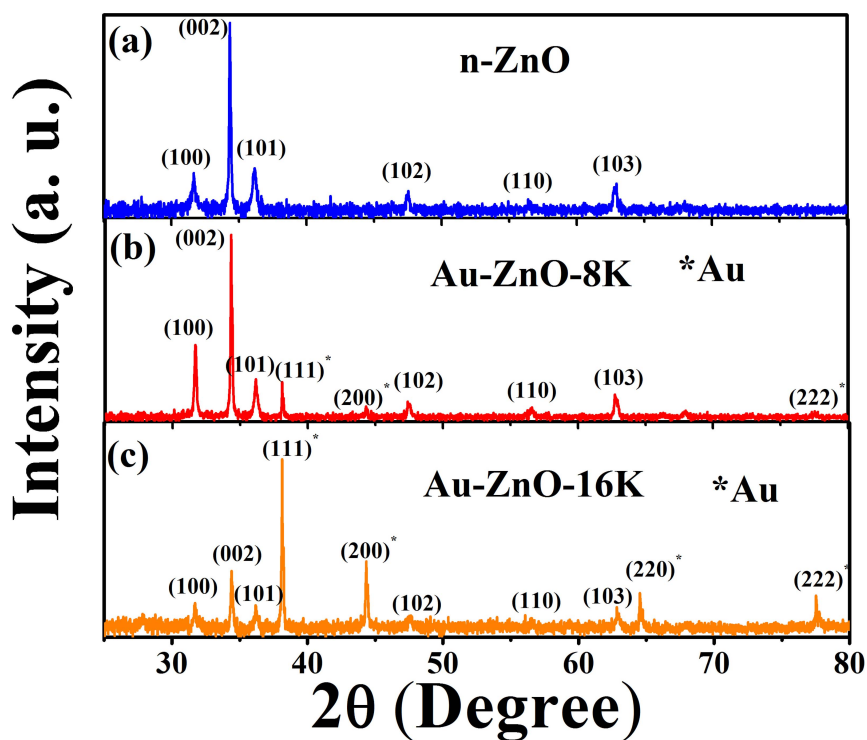


Figure 6.2 XRD pattern of (a) bare - ZnO NW film; (b) Au-ZnO-8K and (c) Au-ZnO-16K NWs films. The XRD peaks corresponding to Au-NP can be clearly seen.

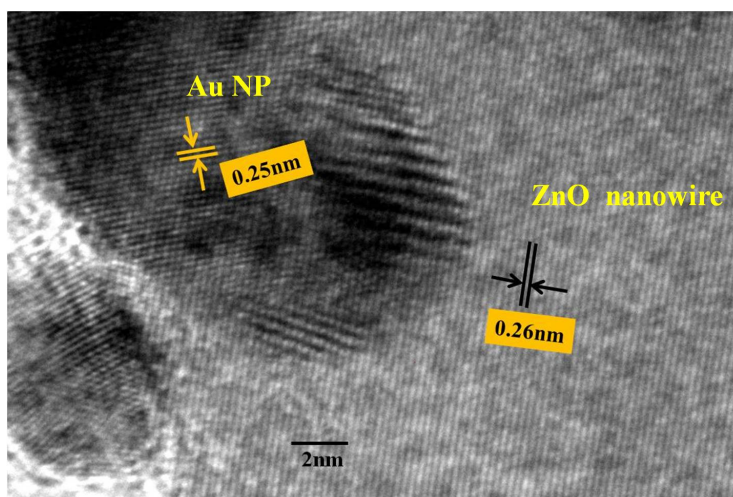


Figure 6.3 HRTEM image of the the Au nanoparticles on ZnO NW surfaces.

is approached. The wavelength is somewhat larger than the fundamental band edge (375 nm) and arises due to sub band gap defect states that may have a substantial density of states close to the band-edge.

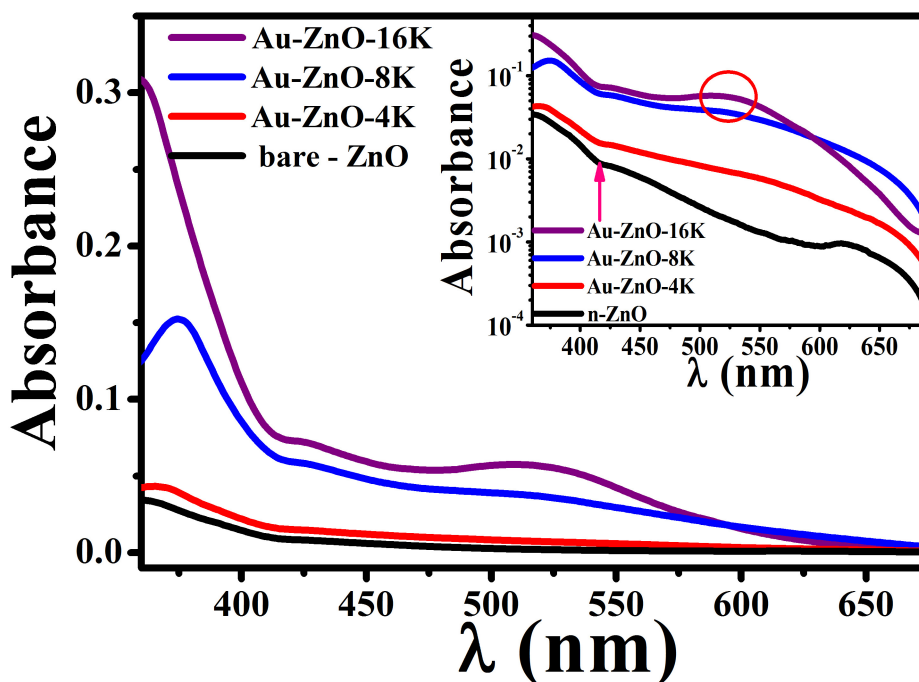


Figure 6.4 UV-Visible spectra of bare ZnO NWs film and Au-ZnO NWs films made with different Au coverage (varying number of laser shots). Note the log scale for the absorbance axis.

In the visible region the absorbance shows a broad hump like feature around ≈ 525 nm (encircled inset Figure 6.4) that correspond to the surface plasmon resonance (SPR) of Au NPs. In the UV region ($\lambda \leq 375$ nm) the absorbance of the film with largest Au-NP coverage (sample Au-ZnO-16K) is nearly a factor of 10 larger compared to that of the bare ZnO film at the same wavelength. In the visible region ≈ 500 nm the change in absorbance is a factor of 20 larger for the Au-ZnO-16K sample. This enhanced absorption in the visible, we will see below, leads to large photocurrent in the Au decorated NW film.

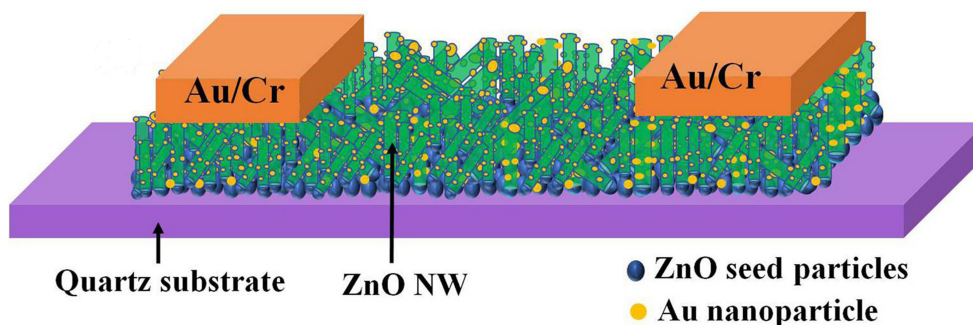


Figure 6.5 Schematic of Au-ZnO nanowire film photo-detector.

6.3 Fabrication of the photo-detector on Au decorated ZnO nanowire film and photocurrent measurement

The schematic of the photo-detector based on Au-ZnO NW film as a channel is shown in Figure 6.5. The photo-detectors were made from patterning the NW films (grown on Quartz substrate) and thermally evaporated Au/Cr were used as contacts. The I - V curves of bare ZnO NW film as well as Au-ZnO NW films are linear in dark, indicating that the contacts used are ohmic. The photo-detectors were illuminated by light of constant power density ($\approx 300 \mu W cm^{-2}$) using a Xenon lamp and a monochromator. The electrical measurements were done with a Keithley sourceMeter 2400.

6.4 Broad band photo-response of the Au-ZnO NW film.

In this sub-section we present one of the important results of this work, that there is indeed a substantial enhancement of the response of the photo-detector made from the Au-ZnO NW film that extends to longer wavelength in the visible. Figure 6.6 (a) shows that the I - V curve of the photo-detector with Au-ZnO-16K NW film at illumination wavelength $\lambda = 350 nm$ and visible $\lambda = 525 nm$ (All data were taken with illumination power density $300 \mu W/cm^2$). In the same graph, we show the response of the same photo-detector in dark to show the enhancement of spectral response of the Au-ZnO photo-detector. The photo-detector current is enhanced (at 1V bias) by a factor of nearly 3.5×10^3 for $\lambda = 350 nm$ over the dark current. In the visible region at a wavelength $\lambda = 525 nm$ the gain over dark current is nearly

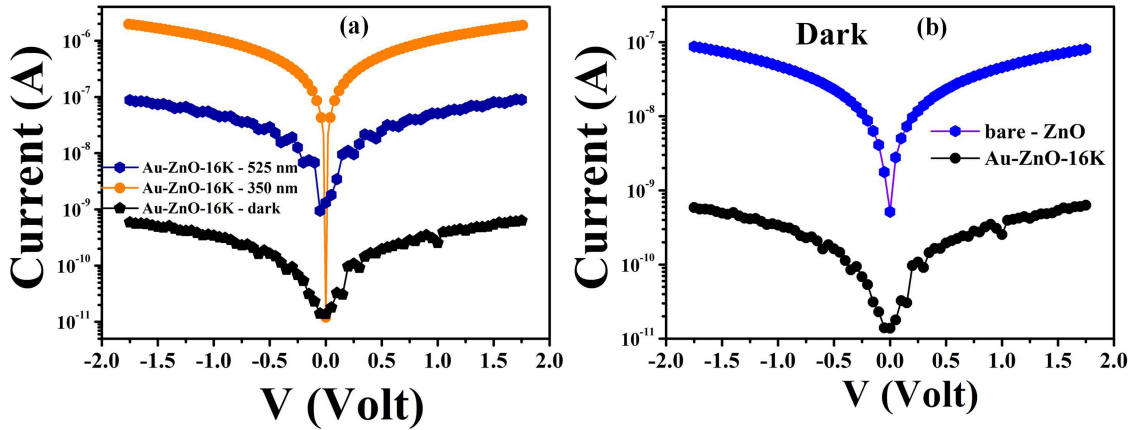


Figure 6.6 (a) I-V characteristics of Au-ZnO-16K NW film under dark and under illumination at $\lambda = 350$ nm and $\lambda = 500$ nm; (b) comparison of dark currents in undecorated ZnO NW film and Au-ZnO-16K NW film.

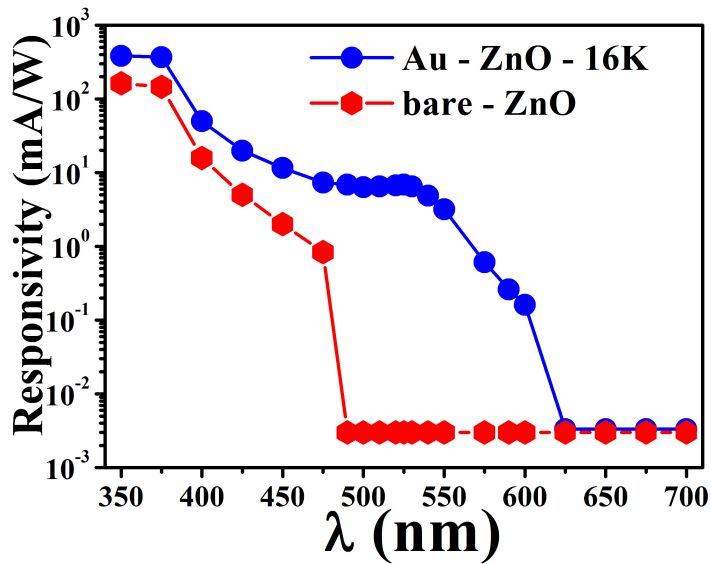


Figure 6.7 Spectral dependence of the responsivity R in a bare ZnO NW film and in Au-ZnO-16K NW film in UV and visible region. Data taken with a bias of 1 V and with illumination power density $300 \mu\text{W}/\text{cm}^2$.

200 in the Au-ZnO NW film. For the undecorated ZnO NW film at same wavelength the gain over dark current is nearly zero.

One of the significant observations is that the dark current (I_d) in the Au-ZnO NW film is at least 2 orders less than that in the undecorated film. This is shown in Figure 6.6 (b). Lowering of the dark

current that arises from the Au NP decoration helps to enhance the optical gain when the films are illuminated. The spectral response R of a photodetector is an important factor that bench marks its utility as a detector over broad spectral range. To quantify the response we use responsivity R is defined as $R = \frac{I_{ph} - I_{dark}}{P \times A}$ (where I_{ph} is photocurrent, I_d is dark current, P is optical power density and A is illumination area of the sample). Spectral response of R (at 1 V bias) taken over the wavelength range 350-700 nm region are shown in Figure 6.7. Data are shown for both the photo-detectors fabricated on undecorated as well as Au-NP decorated ZnO NW films. Data are shown for the film Au-ZnO-16K NW film that has maximum Au-NP coverage. It can be seen that R has been significantly enhanced in the Au-ZnO NW film not only in the UV region but upto a wavelength of 600 nm. Even at 600 nm $R = 0.2$ mA/W which is small but may be good enough for many detection purpose. It rises to nearly 10 mA/W for λ just smaller than 550 nm. R shows a plateau in the range $\lambda = 475$ nm to 550 nm and then it rises again at shorter wavelength range reaching a plateau for $\lambda \leq 375$ nm the fundamental band-edge of the ZnO. The highest R obtained in this range is around 400 mA/W. In comparison to the photo-detector made on bare ZnO-NW film, the enhancement in the responsivity R is substantial, particularly for λ longer than 475 nm, where for the photo-detector on the bare film, R very low ($\simeq 10^{-3}$ mA/W). It is worthwhile to compare the R obtained on the photo detectors in this report to those that have been reported recently in similar photo-detectors with plasmonic nanoparticles attached to ZnO, which have been discussed in the introduction section. The comparison shows that the responsivity R obtained in this work is substantially higher. We attribute this to the PLA assisted attachment of the Au-NP as used in this case, which appears to make a better interface with the ZnO NW surfaces.

Current gain G defined as $\frac{I_{ph} - I_d}{I_d}$, (where I_d is the dark current and I_{ph} is the photocurrent) have been compiled for the Au-ZnO photodetectors for UV and visible illumination. Figure 6.8 (a) & (b) shows the G with respect to the bias voltage under UV ($\lambda = 350$ nm) and visible ($\lambda = 525$ nm) illumination respectively. G increases as the Au NP coverage increases. The enhancement of the G in Au-ZnO-16K is two order larger in UV region than that of the bare ZnO NW film. Results indicate that the number of laser shots used to grow the Au-NP and that control the coverage of Au-NP on ZnO NW surface can effectively control the photocurrent gain.

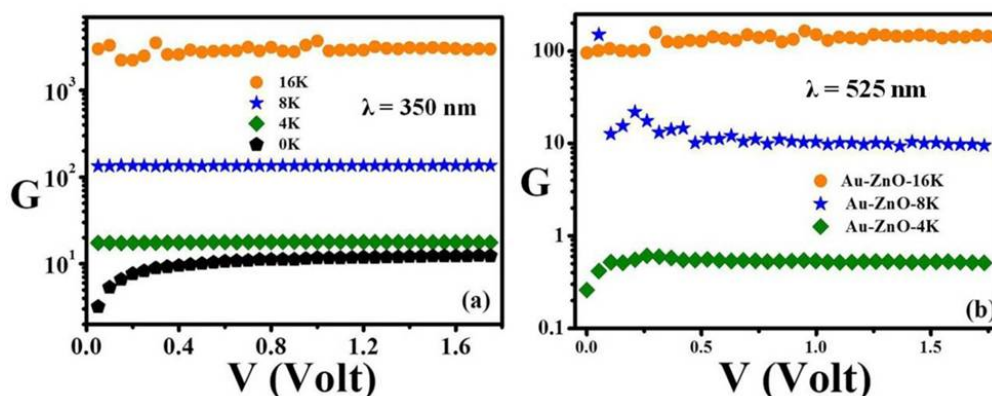


Figure 6.8 Current gain (G) of bare ZnO NW film and Au-ZnONW film (for Au-ZnO-4K,8K & 16K) (a) $\lambda = 350$ nm and (b) $\lambda = 525$ nm.

6.4.1 Change in Photoresponse kinetics

Another important result that we report in this work is about the quickening of the photo-response brought about by the Au NP coverage. Improvement in the kinetics of response, we note, has not been investigated before except the report on single ZnO NW photo-detectors where a reduction in response time was also found [157]. ZnO (and indeed similar oxides) that are used in UV photo-detection have a severe draw back that the photoresponse can be very slow, both when the illumination is turned on as well as when it is turned off. When the illumination is turned off, the decay of the photocurrent in ZnO may even show a long tail, often known as persistent photo conductivity (PPC) [36, 169–171]. The slow response is mainly related to the occupation of sub-band gap defect states. We show in this section that Au-NP attachment to the ZnO surface leads to a pronounced reduction of the response time both in the UV as well as in the visible region.

The time dependences of the normalized photo-current decay, taken with a bias of 1 V are shown in Figure 6.9 (a) and (b) under UV and visible illumination respectively. The time dependence of the decay of the photo-current I_{pc} are shown in the figure for three samples, two Au NP decorated film and one for bare ZnO NW film. The current is plotted in log scale to highlight the existence of two

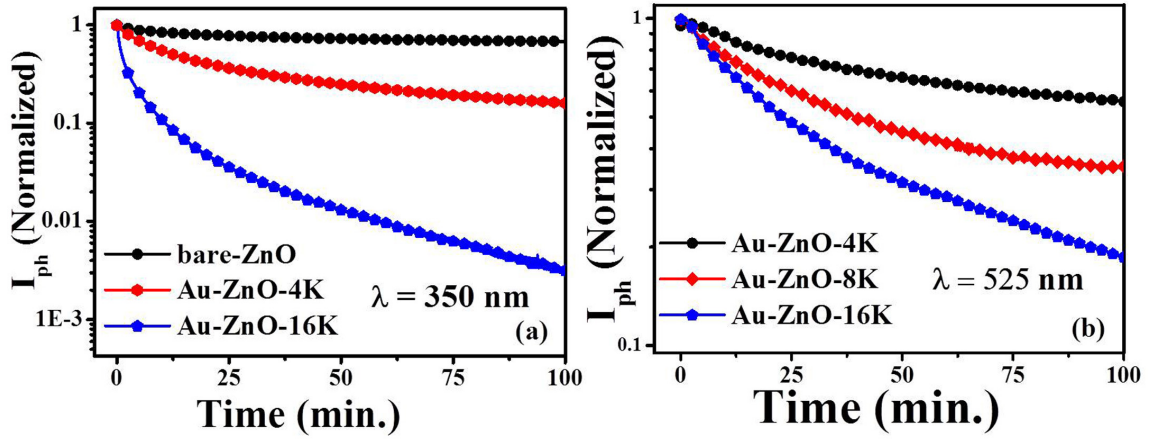


Figure 6.9 Decay of the normalized photocurrent of in bare-ZnO NW film and Au-ZnO NW films taken with (a) UV (350 nm) and (b) visible illumination (525 nm) .

exponentials in the decay curve. The current curves are fitted to the following expressions with two exponentials with a fast component with time constant (τ_1) and a slow component with time constant (τ_2):

$$I_{ph} = I_0 + (I_{min} - I_0)[(1 - c) \exp^{-t/\tau_1} + c \exp^{-t/\tau_2}] \quad (6.1)$$

Where, I_d is normalized photocurrent, I_0 is the current at $t = 0$ and I_{min} is the current at $t = \infty$ and $(1-c)$ and c are the weight factors of the fast and slow components respectively. The results for the fit are in table 6.1. The faster time response in decay of photocurrent achieved on attachment of Au NP's can be seen from Figure 6.9 as well as from the table 6.1. The long decay time constant for the slow decay in bare ZnO NW film is around 2450 sec, which reduces to 300 sec with Au coverage for the slow decay. The fast decay time constant comes down to nearly 10 sec. For illumination with sub-band gap illumination (λ 525 nm), the fast time constant reduces but not as much that happens for the shorter wavelength illumination. The attachment of the Au NP to the ZnO NW film thus leads to a number of improvements in its performance as a photodetector.

The data presented above establish that the attachment of Au NP to the ZnO NW leads to significant enhancement of its responsivity as a photodetector not only in the UV region but its performance has been extended to much longer wavelength in the visible. It decreases the dark current by orders of magnitude and also reduces the response time for the photo-current decay which in case of ZnO photodetectors

Table 6.1 Time constants for the decay of photocurrent.

in air		
Sample specification	Wavelength (nm)	decay(τ_1, τ_2 sec.)
bare-ZnO	350	$\approx 600, 2450$
Au-ZnO-8K	350	$\approx 200, 1230$
Au-ZnO-16K	350	$\approx 10, 300$
Au-ZnO-4K	525	$\approx \times, 3030$
Au-ZnO-8K	525	$\approx 250, 1800$
Au-ZnO-16K	525	$\approx 200, 1150$

are often plagued by problem of persistent photo current. In the rest of the chapter we would like to investigate the physical factors that leads to this enhancement.

6.5 Discussions

6.5.1 Relation of photo-current and absorption

Figure 6.10 shows the optical gain G plotted as a function of the absorption coefficient α . The figure is generated from the spectral dependence of G and the spectral dependence of α . As λ changes over the studied spectral range, α evolves and so is the G corresponding to the α . Beyond a threshold value of absorption α , G increases as α increases. For α less than this threshold value, G is detection limited. Figure 8 establishes that the enhancement of the photo-response is linked to the enhancement of the absorption over the whole spectral range that is significantly enhanced due to the attachment of the plasmonic Au nanoparticles.

The photo-current is created by the electron-hole pair generation and thus the optical gain G is expected to be $\propto \alpha$. For the NW films, we find that over a large range of α (that also covers the spectral range studied), $G \sim \alpha^\eta$ for α beyond the threshold value. For the bare ZnO NW film $\eta \rightarrow 2.4-2.5$). In case

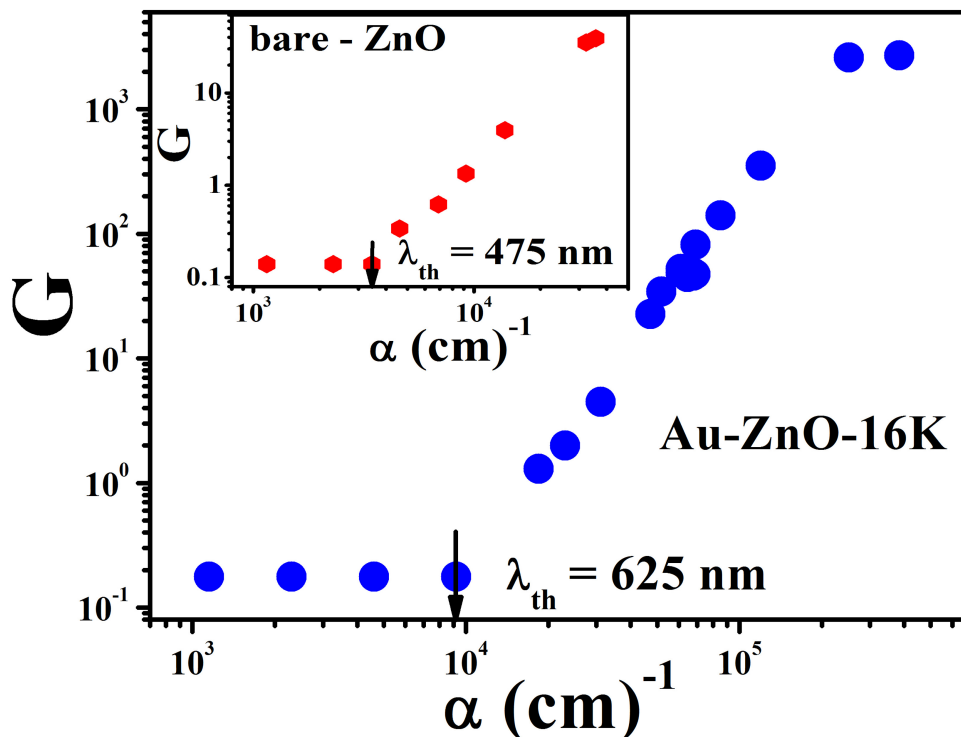


Figure 6.10 Dependence of the optical gain G on the absorption coefficient in the bare-ZnO NW film and that in Au-ZnO-16K NW film. λ_{th} is defined as the wavelength where the G starts to rise.

of the Au-ZnO-16K film the exponent is somewhat larger and $\eta \rightarrow 3$. The non-linear dependence of G on α may have its origin in focusing of the electric field of the light in the nanowire as has been shown by simulation by us in a previous publication on Si NW photodectors [172]. Such an enhancement of the electric field would make the current gain to have non-linear dependence on the electric field and hence the absorption. The enhancement of the exponent in case of the Au-ZNO NW film may be due to further enhancement of electric field that occurs near a plasmonic nanoparticle [173]

6.5.2 Origin of enhanced photoresponse

The origin of the photo response of Au-ZnO NWs devices in UV and visible region has been explained on the basis of a model shown in schematically Figure 6.11 [157, 174, 175]. The energy band diagram of ZnO and Au nanoparticles before the attachment is shown in Figure 6.11 (a). Generally, the oxy-

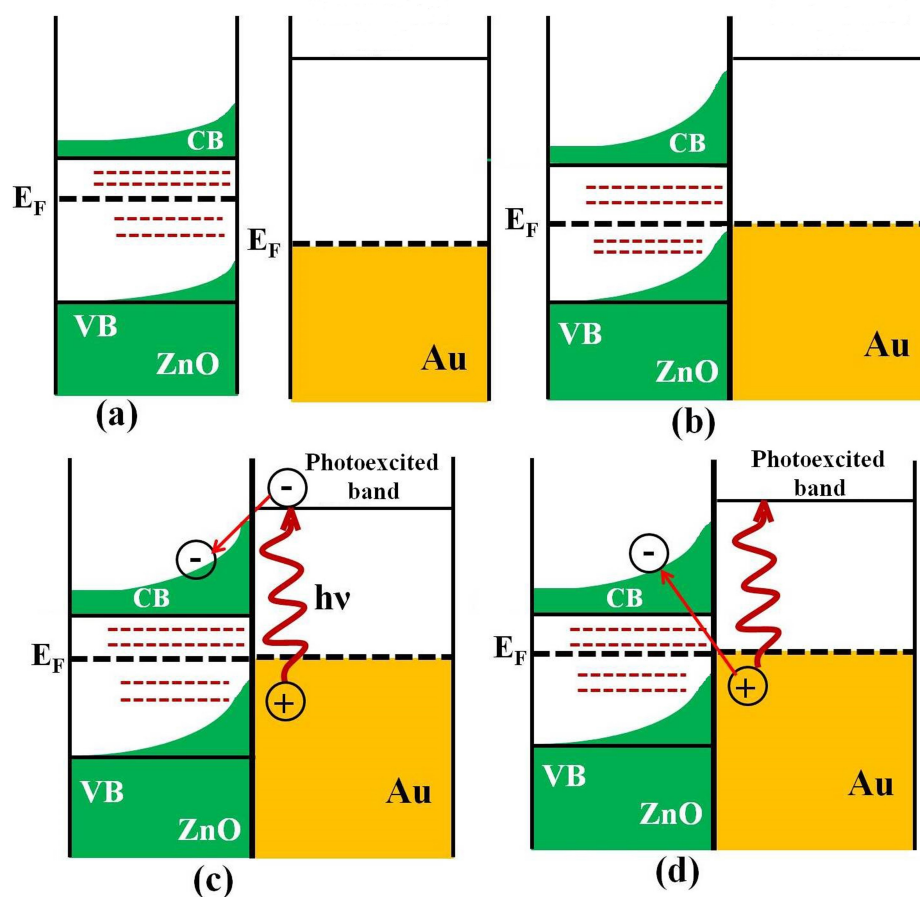


Figure 6.11 Schematic of the band diagram of ZnO NW film and Au NP (a) isolated ZnO and Au-NP, (b) ZnO & Au-NP in contact, (c) Indirect transfer of carrier from photoexcited band of Au (*sp/* SPR) band to CB of ZnO and (d) direct creation of carrier (electron) in conduction band of ZnO.

gen molecules adsorbed on the nanowire surfaces, form a depletion layer on the surface by accepting electrons from ZnO, which also reduce the conductivity of the film. After decorating the nanowires by Au nanoparticles, the electrons flow from ZnO site to Au site because the work function of ZnO ($\phi_1 \approx 4.1$ eV) is smaller than that of the Au ($\phi_2 \approx 5.1$ eV). This charge flow establish alignment of the Fermi levels (E_f) at the metal semiconductor interfaces as shown in Figure 6.11 (b). This charge flow at the interface leads to further depletion and this manifests itself in the lowering of the dark current in the Au decorated ZnO film. The enhanced depletion manifests itself in the significant lowering of the dark current in the Au decorated ZnO film (shown in Figure 6.6 (b)). The enhanced optical gain G

in Au-ZnO NWs arise primarily from the enhancement of the optical absorption due to the plasmonic nanoparticles. The enhancement of the absorption in the visible as well as UV region, primarily due to two reasons: (a) the surface plasmon resonance (SPR) that occurs in the visible and (b) the inter band transition (d to sp) that starts in the visible and extends to shorter wave lengths in the UV. The band structure of gold has comparatively flat d -bands (with the ten $5d$ -electrons) which lie 1-3 eV below the Fermi level E_F . The Fermi level lies in the sp hybridized band that accommodates the lone s -electron. The inter band transition shows weak absorption starting from around 650 nm and becoming stronger for wavelength shorter than 515 nm. This overlaps with the surface plasmon resonance in Au-NP at around 520 - 530 nm range (depending on particle size and shape) [176]. The presence of the two absorption processes extending over a broad band starting for $\lambda < 650$ nm, leads to a broad absorption band in Au-NP [176].

Both the absorption processes, albeit due to different reasons, populate the conduction band of Au- NP when illuminated. Since the photoexcited band (sp /SPR) in Au has higher electron energy than the conduction band (CB) minimum in ZnO (see Figure 6.11 (c) & (d)) these electrons will be transferred to the CB as well as to the broad sub-band gap defect states enhancing the optical gain. The large enhancement of the optical absorption as well as the photo current response thus occurs due to plasmon resonance as well as d to sp band transition. For the plasmon resonance in small particles, the absorption is the dominant process over scattering [177]. The process of absorption dissipates the energy by non-radiative carrier process that leads to electron-hole creation. These electrons can populate the conduction band of ZnO being transferred from the SPR band of Au. A process that we refer to as an indirect process. Very recently a strong process for plasmon resonance assisted carrier generation process has been suggested in context of Au-NP attached to CdSe NW [175]. In this process, the excitation of the plasmonic resonance by illumination directly creates an electron in the semiconductor and a hole in the metal. For plasmon enhanced optical absorption in the visible region thus can lead to enhanced photo-current in this spectral region. This process of charge generation is important that it needs no intervening chemical bonds for charge transfer of electrons from Au-NP to the semiconductor and thus can work without any functionalization also. Another important aspect that need be brought out that

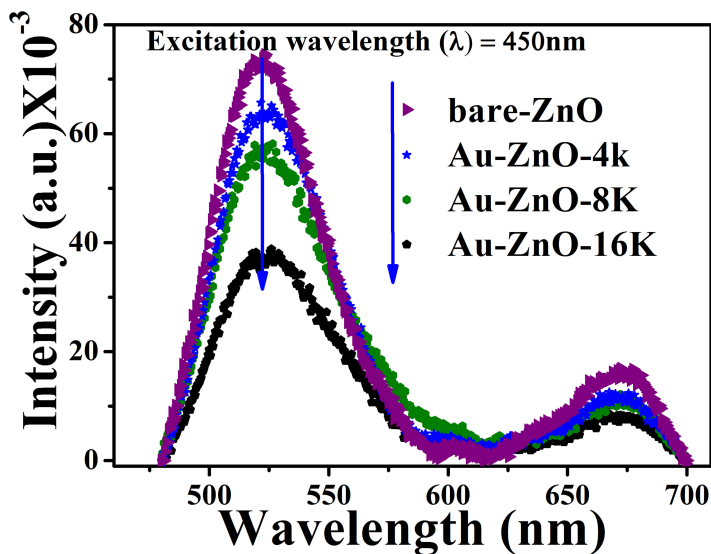


Figure 6.12 Reduction of visible emission from Au-NP decorated ZnO. Data taken with excitation of 450nm.

injection of large carrier density in the conduction band (with the holes generated remaining in metal NP) will raise the position of the Fermi level E_F towards the conduction band which will populate some of the defect levels. Some of these defect levels (predominantly singly or doubly charged Oxygen vacancy) being charged act as scattering centre for carriers thus limiting photo-current out put. The filling of the charged states will significantly reduce scattering and will increase photocurrent [90]. Some part of the enhancement of the photocurrent (in particular the super-linear dependence on absorption) can arise from this effect. The filling of charged defects on illumination is expected to reduce the emission in the visible which arise from these charged defect states.

To check this we have measured the PL with illumination of $\lambda = 450$ nm, which is just below the fundamental edge. This avoids the near band edge (NBE) emission. The data shown in Figure 6.12 show that the broad visible emission centred around 525 nm is strongly reduced on decoration by Au-NP. In the sample Au-ZnO-16K the emission intensity is about half that seen in the bare film without Au-NP. This observation is in conformity with the proposed model that the population of the conduction band by majority carriers created by illumination indeed leads to filling of the charged oxygen vacancy.

6.5.3 Change in kinetics of photo-current relaxation

The kinetics of the photo current relaxation in ZnO is limited by non-radiative pathways that involve the defect states within the band gap. The population of the defect levels (in surface as well as in the bulk) thus will control time constants of the kinetics associate with the relaxation of the photo current. Generally, the slow kinetics of photocurrent decay is linked to the slow relaxation of singly charged oxygen vacancy (that creates a shallow donor) to neutral vacancy (that creates a deep donor). The relaxation is slow because the charged state of the vacancy have different local configurations that are separated by a potential barrier. (Some times role of oxygen absorption and desorption at ZnO surface is linked to slow kinetics. A recent careful experiment in vacuum and under controlled atmosphere has ruled out any dominant role for such a process [178]. The transfer of electrons from the Au-NP to ZnO defect states facilitate the process of reconversion of singly charged vacancy to neutral vacancy that leading to faster relaxation of photo-current.

While the relaxation of the photocurrent for band gap illumination ($\lambda=325\text{nm}$) is rather substantial, it has been observed that even for the sub-band gap illumination ($\lambda=525\text{nm}$) the long decay time of the photo-current is reduced considerably. This shows the involvement of the defect states in extending the photo response in the longer wave length in the visible. The electron transfer from the plasmonic Au-NP on illumination to defect states lying in the band gap enhances the photo current in the longer wave length range and also reduces the current decay time when light is turned off.

6.6 Conclusion

To summarize, the performance of ZnO NW based photo detector can be significantly enhanced using ligand free attachment of Au-NP on its surface. The Au- NP attachment was done using ablation from a Au target using an excimer laser in a liquid medium (water). As the surface coverage of Au-NP increases with use of more number of laser shots, the performance gradually is enhanced. We observed significant enhancement of the optical gain G and the responsivity R not only in the UV region but

also in the visible region. This extends the capability of ZnO as a broad band photo-detector. The attachment of the Au-NP also shortens the decay time of the photo current when the illumination is turned off. The extension of performance over a wider range of optical spectrum is a desirable feature as this allows use of relatively cheap and easy to fabricate ZnO to be used as a broad band detector. The enhancement of the photo detection capability has been shown to be strongly linked to the enhancement of the absorption over a broad spectral range on Au-NP attachment. It has been proposed that plasmonic property of the Au-NP which enhances the absorption for wavelengths < 650 nm also leads to extra carrier generation that populates the conduction band of ZnO. The excitation of the plasmon in the Au-NP on illumination leads to generation electron-hole pair. The electron can be directly created in the conduction band of ZnO or it is transferred to the conduction band of ZnO from the conduction band of Au-NP. This leads to substantial optical gain over a broad spectral region.

Chapter 7

Conclusion and future outlook

7.1 Conclusion

In this thesis, we have studied and investigated novel electronic and optoelectronic properties of nanostructured ZnO. The ZnO nanostructures used in this thesis works were polycrystalline and highly textured thin films as well as plasmonic Au nanoparticles decorated ZnO nanowire films. The electrical properties such as field effect mobility, Hall mobility, carrier concentration, photoresponse, current ON/OFF ratio etc., have been studied in detail. We have also studied the grain boundary capacitance and its significant role for carrier transport in GB region. We have used the novel tool i.e. EDL gate dielectric and plasmonic Au nanoparticles for these investigations in different nanostructured ZnO. Interestingly, the effect of EDL gate bias enhanced the carrier mobility as well as photo response in ZnO thin film. The main outcomes of this thesis work is given below.

(a) In chapter-3 we discussed how a EDL gate bias can influence the ultraviolet photoresponse in polycrystalline nanostructured ZnO channel. The large charge carriers induce by EDL gate bis play the vital role for large enhancement of field effect mobility (From 2.8×10^{-2} to $0.9 \text{ cm}^2/\text{Vs}$) as well as the ultraviolet photoresponse. The enhancement of carrier mobility leads to enhance the photocurrent gain ($G(V_g) = \frac{I_d^{UV}(V_g)}{I_d^{dark}(V_g)}$) as high as 10^3 under modest gate bias in presence of illumination $16 \mu\text{W}/\text{cm}^2$. This large enhancement of the field effect mobility is due to the reduction of GB potential (ϕ_{GB}) as well

as the passivation of charged oxygen vacancies by field induce charge carriers. The gate controlled visible emission in PL spectra verified this hypothesis. The control of GB depletion layer as well as the charged defect states can build the synergy between the gate bias and illumination which gives the substantial enhancement of photoresponse. This observation has a general validity for all kind of oxide semiconductors and can explore the further applicability where the charged defect states play the crucial role for carrier transport.

(b) In chapter-4 we investigated the charge transport through GB region in nanostructured ZnO films with different surface morphologies. In this study, impedance measurement of ZnO films was carried out in TFT configuration where a large number of surface charge induced by the EDL gate bias leads to modulate the complex impedance. The observed data explored the large change in C_{GB} as well as R_{GB} due to field induce charge carriers. This investigation shows how the gate with EDL dielectric can be an enabling tool to control the the complex impedance reversibly in thin film.

(c) In chapter-5 investigation has been done to establish the application domain of a flexible TFT based on ZnO film grown on kapton tape using EDL as a gate dielectric. The high performance TFT parameters such as low threshold voltage, high current ON/OFF ratio, low value of threshold swing are controlled by the field effect mobility of carriers. The ultrahigh charge carriers induced by EDL gate bias reduced the defect distributions and GB barrier which lead to enhance the field effect mobility. The low voltage operation using EDL gate dielectric can forecast the Flex-TFT as a high potential candidates for flexible electronic applications.

(c) In chapter-6 we discussed the effect of plasmonic Au nanoparticles for enhancing the performance and extending the detection limit from UV to visible region of the ZnO based photo detector. The plasmonic nanoparticles used here were synthesized using vacuum free laser ablation precess and attachment was done on the nanowire surface without any ligand. The performances of the photodetectors have been increased with increasing the surface coverage of the nanowire by plasmonic Au-nanoparticles which can be controlled by the variation of laser pulses. The decay time of photo current also reduces by the attachment of Au nanoprtcles when illumination is turned off. The process of fabrication of such a photodetector is relatively cheap and easy. The enhancement of the photodetection is

strongly linked to the enhancement of absorption in UV and visible region due to the Au nanoparticle attachment. The excitation of the plasmonic nanoparticles create electron hole pairs on illumination and electrons are transfer to the conduction band of the ZnO from photo excited band of Au nanoparticles. This leads to substantial optical gain over a broad spectral region. The significant enhancement of the optical gain G as well as photoresponse R in UV and visible region manifest the application potential as a broad band photo detector.

7.2 Future outlook

In this thesis, we have investigated role of defect states associated with GB regions in transport properties of the nanostructured ZnO using EDL gate dielectric. We have also used the plasmonic nanoparticle to enhance and extend the photo response from UV to visible region. Still there is some physics issues that can be solved in nanostructured material using EDL gate dielectric.

In chapter-3 and 4, we have studied the role of defect states and GB depletion layer for the carrier transport phenomena. The control of defect states using field induce charge carrier is utilized to enhance the field effect mobility as well as the photo response. One could study the kinetic of photo generated charge carrier under EDL gate bias. similarly, the photo generation and relaxation dynamics can be studied under different temperature using EDL gate bias. The single nanowire field effect device can be fabricated using polymer electrolyte as a gate dielectric which can give more responsivity than the nanostructured ZnO films.

In chapter-6, we have used Au nanoparticles to enhance and extend the photo detection from UV to visible region. One can fabricate the wave guide based on ZnO nanowire using plasmonic Au-NPs synthesized by ligand free pulsed laser ablation method. similarly, this technique can be employed to decorate the nanowire by other plasmonic nanoparticle (copper, silver, platinum etc.) for different sensing applications.

Appendix A

Appendix

A.1 Transient photocurrent of nanostructured ZnO channel under different gate bias and illumination of different wavelength.

Field induce charge carriers due to EDL gate bias can be utilized to control the deep level trap centres (DX) and fermi level (E_f) of the channel due to which it can reduce the persistence of photocurrent, enhance the photoresponse and extract the relaxation time for photo generated charge carriers. Figure A.1 shows the transient photocurrent of nanostructured ZnO channel without gate electrolyte. Generally, the photocurrent generation and relaxation consist of fast (τ_1) and slow (τ_2) time components. The photocurrent rises rapidly under illumination of shorter wavelength (closed to band gap illumination) where as it rises slowly under illumination of longer wavelength region. The generation of the photocurrent is unsaturated for all wavelength where as the relaxation is almost linear for higher wavelength and a small fraction of fast time component τ_1 is appeared in shorter wavelength (close to band gap wavelength) region. The fast component τ_1 arises due to band to band transition (for rise) and band to band recombination (for relaxation) of photo excited carriers. Similarly, some fraction of carriers are generated as well as relaxed through the sub band gap defect states which give rise to slow time component τ_2 .

Figure A.2 shows the transient photocurrent under two different mode of gate bias. In enhancement

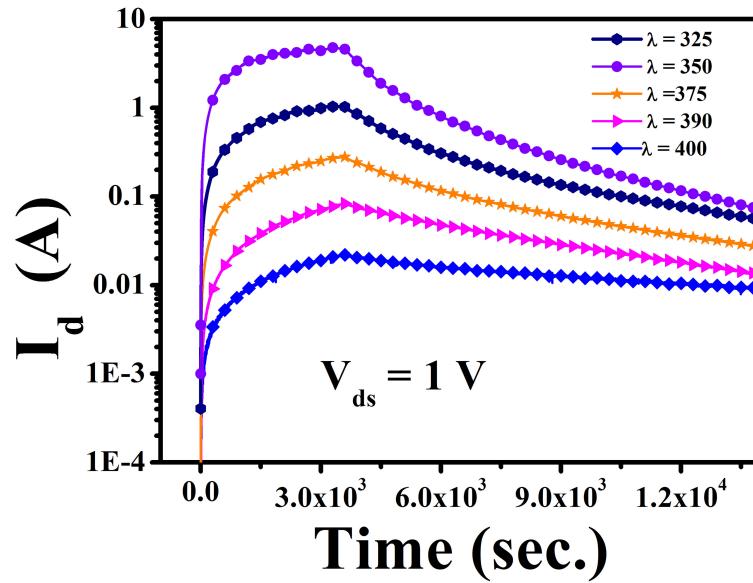


Figure A.1 Transient photocurrent of nanostructured ZnO channel without applying gate bias under the illumination of different wavelengths.

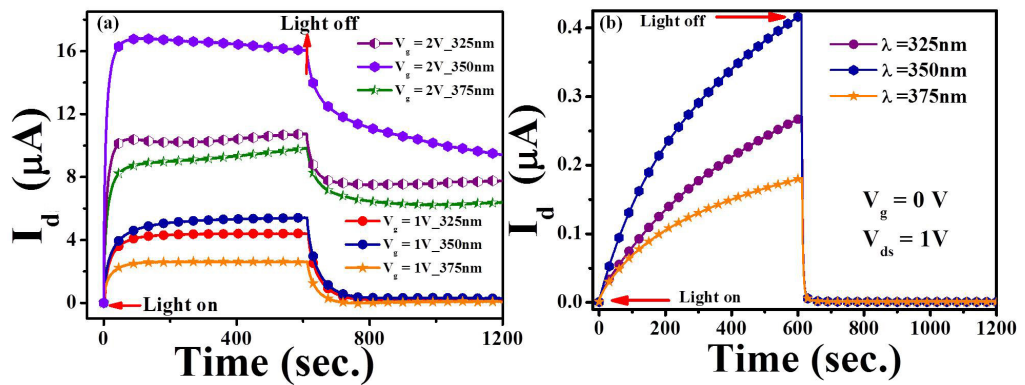


Figure A.2 Transient photocurrent of field effect device based on nanostructured ZnO channel under illumination of different wavelengths (a) enhancement mode (b) depletion mode.

mode (Figure A.2 (a)), photo current rises quickly and relax slowly. On the other hand, in case of depletion mode (Figure A.2 (b)) photocurrent rises slowly and relax quickly. The enhancement mode allow to persist the photocurrent but the depletion mode rapidly relax the photocurrent when illumination is off. The depletion mode vacant the mid gap defect states which allow the fast relaxation of the photogenerated charge carriers.

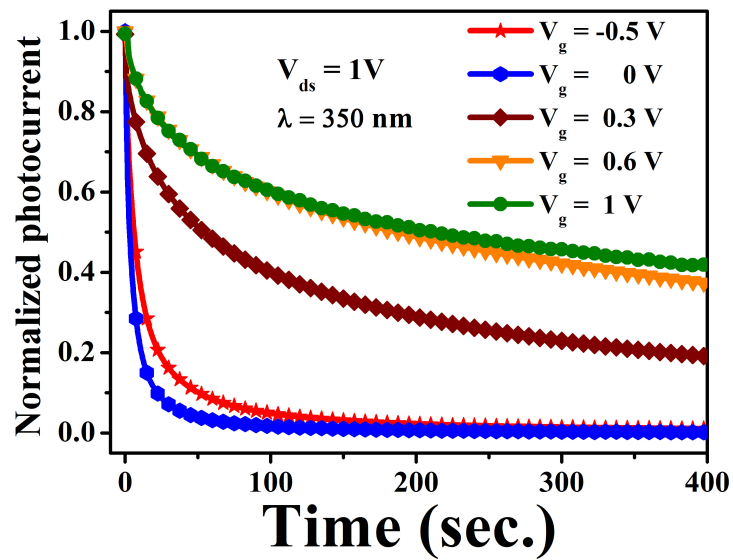


Figure A.3 Normalized transient photocurrent of field effect device based on nanostructured ZnO channel under different gate bias.

We have also observed the persistence of the photocurrent with different gate bias under the illumination of wavelength $\lambda = 350$ nm. (Figure A.3). The persistence of the photo current increases with positive gate bias where as it reduces with negative bias.

Bibliography

- [1] T. P. Chow and R. Tyagi, IEEE Trans. Electron **41**, 1481 (1994) .
- [2] H. Morkoc, S. Strite, G. B. Gao, M. E. Lin, B. Sverdlov, and M. Burns, J. Appl. Phys. **76**, 1363 (1994).
- [3] D. C. Look, Mater. Sci. Eng., B, **80**, 383-387, (2001).
- [4] Ü. Özgür, Y. I. Alivov, C. Liu, A. Teke, M. A. Reshchikov, S. Dogan, V. Avrutin, S. J. Cho and H. Morkoc, J. Appl. Phys. **98**, 041301 (2005).
- [5] Z. L. Wang, J. Phys.: Condens. Matter. **16**, 829 (2004).
- [6] A. B. Djuricic, X. Chen, Y. H. Leunga and A. C. Ng, J. Mater. Chem. **22**, 6526 (2012).
- [7] L. Schmidt-Mende and J. L. MacManus-Driscoll, Mater. Today **10**, 40 (2007).
- [8] V. Khranovskyya, U. Grossner, V. Lazorenko, G. Lashkarev, B.G. Svensson, R. Yakimova, Superlattices Microstruct. **39**, 275-281 (2006).
- [9] M. Lee, T. Lee, J. Lim, J. Bang, W. Lee, T. Lee, and J. Myoung, Electron. Mater. Lett. **5**, 127-133 (2009).
- [10] G. Shen and D. Chen, J. Phys. Chem. C **114**, 21088-21093 (2010).
- [11] C. G. Granqvist, A. Azens, P. Heszler, L. B. Kish, L. Osterlund, Sol. Energy Mater. Sol. Cells **91**, 355-365 (2007).

- [12] L. M. Wong, S. Y. Chiam, J. Q. Huang, S. J. Wang, W. K. Chim, J. S. Pan, *Sol. Energy Mater. Sol. Cells* **95**, 2400-2406 (2011).
- [13] A. Janotti and C. G Van de Walle, *Rep. Prog. Phys.* **72**, 126501 (2009).
- [14] A. Janotti and C. G. Van de Walle, *Phys. Rev. B* **76**, 165202 (2007).
- [15] F. Oba, M. Choi, A. Togo and I. Tanak, *Sci. Technol. Adv. Mater.* **12**, 034302 (2011).
- [16] S. Lany and A. Zunger, *Phys. Rev. B* **72**, 035215 (2005).
- [17] A. B. Djurisic, Y. H. Leung, K. H. Tam, Y. FHsu, L. Ding, W. K. Ge, Y. C. Zhong, K. S. Wong, W. K. Chan, H. L. Tam, K. W. Cheah, W. M. Kwok and D. L. Phillips, *Nanotechnology* **18**, 095702 (2007).
- [18] A. B. Djurisic, Y. H. Leung and K. H. Tam, *Appl. Phys. Lett.* **88**, 103107 (2006).
- [19] H. Morkoc and Ümit Özgür, *Zinc Oxide Fundamentals, Materials and Device Technology*, Wiley-vch Verlag Gmbh & Co. KGaA, (2009).
- [20] F. Greutert and G. Blatterx, *Semicond. Sci. Technol.* **5**, 111-137 (1990).
- [21] P. Pattanasattayavong, S. Rossbauer, S. Thomas, J. G. Labram, H. J. Snaith, and T. D. Anthopoulos, *J. Appl. Phys.* **112**, 074507 (2012).
- [22] D. H. Zhang, *J. Phys. D Appl. Phys.* **28**, 1273-1277 (1995).
- [23] B. H. Yuan, H. Shimotani, A. Tsukazaki, A. Ohtomo, M. Kawasaki, and Y. Iwasa, *Adv. Funct. Mater.* **19**, 1046-1053 (2009).
- [24] K. H. Lee, M. S. Kang, S. Zhang, Y. Gu, T. P. Lodge and C. D. Frisbie, *Adv. Mater.* **24**, 4457-4462 (2012).
- [25] L. G. Kaake and X. Y. Zhu, *J. Phys. Chem. C* **112**, 16174-16177 (2008).
- [26] H. Du, X. Lin, Z. Xu, D. Chu, *J. Mater. Sci.* **50**, 5641 (2015).

- [27] M. J. Panzer and C. D. Frisbie, *J. Am. chem. SOC.* **129**, 6599 (2007).
- [28] H. Shimotani, H. Asanuma, A. Tsukazaki, A. Ohtomo, M. Kawasaki, and Y. Iwasa, *Appl. Phys. Lett.* **91**, 082106 (2007)
- [29] S. Xu, Z. L. Wang, *Nano Res.* **4**, 1013-1098 (2011).
- [30] S. A. Chevtchenko, J. C. Moore, Ü. Özgür, X. Gu, A. A. Baski and H. Morkoc, *Appl. Phys. Lett.* **89**, 182111 (2006).
- [31] Y. Dong, Z. Q. Fang, D. C. Look, D. R. Douth, G. Cantwell, J. Zhang, J. J. Song, and L. J. Brillson, *J. Appl. Phys.* **108**, 103718 (2010).
- [32] D. G. Thomas, *J. Phys. Chem. Solids* **15**, 86-96 (1960).
- [33] R. H. Bube, *Photoelectronic Properties of Semiconductor*, Cambridge University Press, (1992).
- [34] H. Yuan, H. Wang and Y. Cui, *Acc. Chem. Res.* **48**, 81-90 (2015).
- [35] H. Wang and L. Pilon, *J. Phys. Chem. C* **115**, 16711-16719 (2011).
- [36] S. Mondal and A. K. Raychaudhuri, *Appl. Phys. Lett.* **98**, 023501 (2011).
- [37] C. Lu, Q. Fu, S. Huang, and J. Liu, *Nano Lett.* **4**, 623-627 (2004).
- [38] K. Ueno, S. Nakamura, H. Shimotani, A. Ohtomo, N. Kimura, T. Nojima, H. Aoki, Y. Iwasa, and M. Kawasaki, *Nat. Mater.* **7**, 855 (2008).
- [39] K. Shibata, H. Yuan, Y. Iwasa, & K. Hirakawa, *Nat. Commun.* **4**, 2664 (2013).
- [40] T. Fujimoto and K. Awaga, *Phys. Chem. Chem. Phys.* **15**, 8983 (2013).
- [41] R. Nath and A. K. Raychaudhuri, *RSC Adv.* **5**, 57875-57882 (2015).
- [42] R. Nath and A. K. Raychaudhuri, *Appl. Phys. Lett.* **104**, 083515 (2014).
- [43] Y. Zhou and S. Ramanathan, *Crit. Rev. Solid State Mater. Sci.* **38**, 286-317 (2013).

- [44] H. Y. Xu, Y. C. Liu, J. G. Ma, Y. M. Luo, Y. M. Lu, D. Z. Shen, J. Y. Zhang, X. W. Fan and R. Mu, *J. Phys.: Condens. Matter* **16**, 5143 (2004).
- [45] X. Ma, P. Chen, D. Li, Y. Zhang and D. Yang, *Appl. Phys. Lett.* **91**, 021105 (2007).
- [46] B. Oh, M. Jeong, and J. Myoung, *Appl. Surf. Sci.* **253**, 7157-7161 (2007).
- [47] M. Ghosh, A. K. Raychaudhuri, *Appl. Phys. Lett.* **93**, 123113 (2008).
- [48] M. Ghosh, A. K. Raychaudhuri, *Appl. Phys. Lett.* **98**, 153109 (2011).
- [49] P. F. Cai, J. B. You, X. W. Zhang, J. J. Dong, X. L. Yang, Z. G. Yin, and N. F. Chen, *J. Appl. Phys.* **105**, 083713 (2009).
- [50] V. Papamakarios, E. Polydorou, A. Soultati, N. Droseros, D. Tsikritzis, A. M. Douvas, L. Palilis, M. Fakis, S. Kennou, P. Argitis and M. Vasilopoulou, *Appl. Mater. Interfaces* **8**, 1194 (2016).
- [51] P. I. Reyes, C. Ku, Z. Duan, Y. Xu, E. Garfunkel, and Y. Lu, *Appl. Phys. Lett.* **101**, 031118 (2012).
- [52] S. Thiemann, S. Sachnov, S. Porscha, P. Wasserscheid and J. Zaumseil, *J. Phys. Chem. C* **116**, 13536 (2012).
- [53] P. Pattanasattayavong, S. Rossbauer, S. Thomas, J. G. Labram, H. J. Snaith, and T. D. Anthopoulos, *J. Appl. Phys.* **112**, 074507 (2012).
- [54] J. Chang, Z. Lin, C. Zhu, C. Chi, J. Zhang, J. Wu, *ACS Appl. Mater. Interfaces* **5**, 6687 (2013).
- [55] L. Xu, Q. Chen, L. Liao, X. Liu, T. Chang, K. Chang, T. Tsai, C. Jiang, J. Wang and J. Li, *ACS Appl. Mater. Interfaces* **8**, 5408 (2016).
- [56] A. Abliz, C. Huang, J. Wang, L. Xu, L. Liao, X. Xiao, W. Wu, Z. Fan, C. Jiang, J. Li, S. Guo, C. Liu and T. Guo, *ACS Appl. Mater. Interfaces* **8**, 7862 (2016).
- [57] J. Choi, Y. Gu, K. Hong, W. Xie, C. D. Frisbie, and T. P. Lodge, *ACS Appl. Mater. Interfaces* **6**, 19275 (2014).

- [58] S. Jeon, S. Ahn¹, I. Song¹, C. J. Kim, U. Chung, E. Lee, I. Yoo, A. Nathan, S. Lee, J. Robertson and K. Kim, *Nat. Mater.* **11**, 301 (2012).
- [59] F. Yakuphanoglu, *Sens. and Actuators A* **173**, 141 (2012).
- [60] K. Lee, J. Choi, D. K. Hwang, M. S. Oha, J. K. Kimb, Y. Jung, K. Oha, S. Ima, *Sens. and Actuators A* **144**, 69 (2008).
- [61] G. Xiong, G. C. Jones, R. Rungsawang, D. Anderson, *Thin Solid Films* **518**, 4019 (2010).
- [62] H. S. Bae, C. M. Choi, J. H. Kim, and S. Im, *J. Appl. Phys.* **97**, 076104 (2005).
- [63] Y. Hou, Z. Mei¹ and X. Du, *J. Phys. D: Appl. Phys.* **47**, 283001 (2014).
- [64] S. Lee, S. Ahn, Y. Jeon, J. Ahn, I. Song, S. Jeon, D. Yun, J. Kim, H. Choi, U. Chung, and J. Park, *Appl. Phys. Lett.* **103**, 251111 (2013).
- [65] K. Lee, K. Kim, J. Choi, M. S. Oh, D. K. Hwang, S. Jang, E. Kim and S. Im, *J. Phys. D: Appl. Phys.* **41** 135102 (2008).
- [66] T. Chen, K. Lee, S. Chang, S. Chang, and P. Chang, *Appl. Phys. Lett.* **103**, 022101 (2013).
- [67] L. Znaidi, *Mater. Sci. Eng. B* **174**, 18-30 (2010).
- [68] V. Musat, B. Teixeira, E. Fortunato, R. C. Monteiro, P. Vilarinho, *Surf. Coat. Technol.* **180-181**, 659-662 (2004).
- [69] K. Y. Cheong, Norani Muti, S. Ramanan, *Thin Solid Films* **410**, 142-146 (2002).
- [70] B. Xu, Z. Cai, *Appl. Surf. Sci.* **254**, 5899-5904 (2008).
- [71] H. Zhang, D. Yang, X. Ma, Y. Ji, J. Xu and D. Que, *Nanotechnology* **15**, 622-626 (2004).
- [72] M. Vafaei, M. S. Ghamsari, *Mater. Lett.* **61**, 3265-3268 (2007).
- [73] A. Kolodziejczak-Radzimska and T. Jesionowski, *Materials* **7**, 2833-2881 (2014).

- [74] S. A. Studenikin, N. Golego and M. Cocivera, *J. Appl. Phys.* **84**, 2287 (1998).
- [75] J. M. Bian, X. M. Li, X. D. Gao¹, W. D. Yu and L. D. Chen, *Appl. Phys. Lett.* **84**, 541 (2004).
- [76] Z. Jiwei, Z. Liangying and Y. Xi, *Ceram. Int.* **26**, 883-885 (2000).
- [77] M. H. Aslana, A. Y. Oral, E. Mensur, A. Gül and E. Basaran, *Sol. Energy Mater. Sol. Cells* **82**, 543-552 (2004).
- [78] www.brewerscience.com/processing-theories/spin-coat/
- [79] S. Xu, C. Lao, B. Weintraub, and Z. L. Wang, *J. Mater. Res.* **23**, 2072 (2008).
- [80] S. Xu and Z. L. Wang, *Nano Res.* **4**, 1013-1098 (2011).
- [81] K. Wang, Laser Based Fabrication of Graphene, In Mahmood Aliofkhaezrai (Ed.), *Advances in Graphene Science InTech.*, 77-95 (2013).
- [82] R. Nath, Investigation of novel electrical and magnetic properties of perovskite oxides, thesis submitted to university of Calcutta, (2015).
- [83] R. K. Neogy, R. Nath, *Micro and Nanosystems* **3**, 319 (2011).
- [84] M. Ghosh Optical Properties of ZnO-based Nanostructured Materials, thesis submitted to Jadavpur University, 2009.
- [85] D. Guo, G. Xie and J. Luo, *J. Phys. D: Appl. Phys.* **47**, 013001 (2014).
- [86] hlee.khu.ac.kr/research.htm.
- [87] www2.chemistry.msu.edu/faculty/reusch/virttxtjml/spectrpy/uv-vis/uvspec.htm
- [88] [@Optical-Characterization-of-Gr.](http://cnx.org/contents/gRPw0_eN)
- [89] J. Sun, & J. Kosel, Finite-Element Modelling and analysis of Hall effect and Extra ordinary Magnetoresistance effect, *Intech open sciences*, (2012).

- [90] S. Mondal, R. R. Ghimire, and A. K. Raychaudhuri, *Appl. Phys. Lett.* **103**, 231105 (2013)
- [91] A. H. Adl, A. Ma, M. Gupta, M. Benlamri, Y. Y. Tsui, D. W. Barlage, K. Shankar, *ACS Appl. Mater. Interfaces* **4**, 1423-1428 (2012).
- [92] L. Hu, L. Zhu, H. He, Y. Guo, G. Pan, J. Jiang, Y. Jin, L. Sun, and Z. Ye, *Nanoscale* **5**, 9577-9581 (2013).
- [93] D. E. Walker, M. Major, M. B. Yazdi, A. Klyszcz, M. Haeming, K. Bonrad, C. Melzer, W. Donner, H. Seggern, *ACS Appl. Mater. Interfaces* **4**, 6835-6841 (2012).
- [94] H. Faber, M. Klaumunzer, M. Voigt, D. Galli, B. F. Vieweg, W. Peukert, E. Spieckerc and M. Halik, *Nanoscale* **3**, 897-899 (2011).
- [95] S. Dasgupta, M. Lukas, K. Dossel, R. Kruk, H. Hahn, *Phys. Rev. B* **80**, 085425 (2009).
- [96] D. H. Redinger, *IEEE Trans. Electron Devices* **57**, 3460 (2010).
- [97] K. Lee, J. M. Choi, D. K. Hwang, M. S. Oh, J. K. Kimb, Y. Jung, K. Oh, S. Im, *Sensors and Actuators A* **144**, 69-73 (2008).
- [98] K. K. Banger, R. L. Peterson, K. Mori, Y. Yamashita, T. Leedham, H. Sirringhaus, *Chem. Mater.* **26**, 1195-1203 (2014).
- [99] L. E. Aygun, F. B. Oruc, F. B. Atar, A. K. Okay, *IEEE Photon. J.* **5**, 2200707 (2013).
- [100] S. M. Sze, K. K. Ng, *Physics of Semiconductor Devices* (New Jersey, John Wiley and Sons inc. Third edition, p.306. (2007)
- [101] Y. W. Heo, D. P. Norton, S. J. Pearton, *J. Appl. Phys.* **98**, 073502 (2005).
- [102] K. Vanheusden, C. H. Seager, W. L. Warren, D. R. Tallant, J. A. Voight, *Appl. Phys. Lett.* **68**, 403 (1996).
- [103] M. Ghosh, A. K. Raychaudhuri, *Nanotechnology*, **19**, 445704 (2008).

- [104] B. Sun, R. L. Peterson, H. Sirringhaus, K. Mori, *J. Phys. Chem. C* **111**, 18831-18835 (2007).
- [105] A. J. Morfa, N. Kirkwood, M. Karg, T. B. Singh, P. Mulvaney, *J. Phys. Chem. C* **115**, 8312-8315 (2011).
- [106] L. Lan, J. Peng, *IEEE T. Electron. Dev.* **58**, 1452-1455 (2011).
- [107] S. Mandal, H. Mullick, S. Majumdar, K. Dhar, S. K. Ray, *J. Phys. D: Appl. Phys.* **41**, 025307 (2008).
- [108] F. M. Hossain, J. Nishii, S. Takagi, A. Ohtomo, T. Fukumura, H. Fujioka, H. Ohno, H. Koinuma, M. Kawasaki, *J. Appl. Phys.* **94**, 7768-7777 (2003).
- [109] J. Nomoto, H. Makino, T. Yamamoto, *J. Appl. Phys.* **117**, 045304 (2015).
- [110] S. J. Pearton, C. R. Abernathy, M. E. Overberg, G. T. Thaler, D. P. Norton, N. Theodoropoulou, A. F. Hebard, Y. D. Park, F. Ren, J. Kim, L. A. Boatner, *J. Appl. Phys.* **93**, 1-13 (2003).
- [111] P. P. Edwards, C. N. R. Rao, *Metal-Insulator Transitions Revisited*; Taylor and Francis: London, (1995).
- [112] X. Ji, Y. Zhu, M. Chen, L. Su, A. Chen, C. Zhao, X. Gui, R. Xiang, F. Huang, Z. Tang, *Appl. Phys. Lett.* **104**, 242114 (2014).
- [113] X. Ji, Y. Zhu, M. Chen, L. Su, A. Chen, X. Gui, R. Xiang, Z. Tang, *Sci. Rep.* **4**, 4185 (2014).
- [114] R. R. Ghimire, S. Mondal and A. K. Raychaudhuri, *J. Appl. Phys.* **117**, 105705 (2015).
- [115] Y. Kajikawa, *J. Appl. Phys.* **114**, 043719 (2013).
- [116] A. Bikowski, K. Ellmer, *J. Appl. Phys.* **116**, 143704 (2014)
- [117] E. Barsovkov, J. R. Macdonald, *J. R. Impedance Spectroscopy Theory, Experiment, and Applications*; John Wiley & Sons, Inc., Hoboken, New Jersey (2005).
- [118] P. N. Vishwakarma, *Solid State Commun.* **149**, 115-120 (2009).

- [119] N. H. Al-Hardan, M. J. Abdullah, H. Ahmad, A. Abdul Aziz, L. Y. Low, *Solid-State Electron.* **55**, 59-63 (2011).
- [120] T. B. Adams, D. C. Sinclair, A. R. West, *Phys. Rev. B* **73**, 094124 (2006).
- [121] Y. Zhao, Q. Li, X. Xiao, G. Li, Y. Jin, K. Jiang, J. Wang and S. Fan, *ACS Nano* **10**, 2193-2202 (2016).
- [122] J. H. Park, J. Y. Oh, S. W. Han, T. Lee, and H. K. Baik, *ACS Appl. Mater. Interfaces* **7**, 4494-4503 (2015).
- [123] Y. Lin, C. Hsu, M. Tseng, J. Shyue and F. Tsai, *ACS Appl. Mater. Interfaces* **7**, 22610-22617 (2015).
- [124] P. F. Carcia, R. S. McLean, and M. H. Reilly, *Appl. Phys. Lett.* **88**, 123509 (2006).
- [125] W. Wang, S. K. Hwang, K. L. Kim, J. H. Lee, S. M. Cho, and C. Park, *ACS Appl. Mater. Interfaces* **7**, 10957-10965 (2015).
- [126] Y. H. Hwang, J. Seo, J. M. Yun, H. Park, S. Yang, S. K. Park and B. Bae, *NPG Asia Mater.* **5**, e45(2013).
- [127] K. Hong., S. H. Kim , K. H. Lee , and C. D. Frisbie, *Adv. Mater.* **25**, 3413-3418 (2013).
- [128] J. S. Meena, M. Chu, Y. Chang, C. Wu, C. Cheng, F. Chang and F. Ko, *ACS Appl. Mater. Interfaces* **4**, 3261-3269 (2012).
- [129] E. Fortunato, P. Barquinha, and R. Martins, *Adv. Mater.* **24**, 2945-2986 (2012).
- [130] Elvira M. C. Fortunato, Pedro M. C. Barquinha, Ana C. M. B. G. Pimentel, Alexandra M. F. Goncalves, Antonio J. S. Marques, Rodrigo F. P. Martins, and Luis M.N. Pereira, *Appl. Phys. Lett.* **85**, 2541 (2004).
- [131] H. Yabuta, M. Sano, K. Abe, T. Aiba, T. Den, H. Kumomi, K. Nomura, T. Kamiya, and H. Hosono, *Appl. Phys. Lett.* **89**, 112123 (2006).

- [132] K. Nomura, H. Ohta, A. Takagi, T. Kamiya, M. Hirano and H. Hosono, *Nature* **432**, 488 (2004).
- [133] J. S. Lee, Y. Kwack, and W. Choi, *ACS Appl. Mater. Interfaces*. **5**, 11578-11583 (2013).
- [134] W. H. Jeong, D. L. Kim, and H. J. Kim, *ACS Appl. Mater. Interfaces*. **5**, 9051-9056 (2013).
- [135] I. Park, C. Jeong, I. Cho, J. Lee, E. Cho, S. Kwon, B. Kim, W. Cheong, S. Song and H. Kwon, *Semicond. Sci. Technol.* **27**, 105019 (2012).
- [136] J. K. Jeong, *Semicond. Sci. Technol*, **26**, 034008 (2011)
- [137] B. K. Song, J. Noh, T. Jun, Y. Jung, H. Y. Kang and J. Moon, *Adv. Mater.* **22**, 4308-4313 (2010).
- [138] J K. Lee and D. K. Choi, *J. Nanosci. Nanotechnol.* **12**, 5859 (2012).
- [139] D. Zhao, D. A. Mourey and T. N. Jackson, *IEEE Electron Device Lett.* **31**, (2010).
- [140] C. Y. Lee, M. Y. Lin, W. H. Wu, J. Y. Wang, Y. Chou, W. F. Su, Y. F. Chen and C. F. Lin, *Semicond. Sci. Technol.* **25**, 105008 (2010).
- [141] W. Wang, D. Hang, J. Cai, Y. Geng, L. Wang, Y. Tian, X. ZZhang and S. Zhang, *Jpn. J. Appl. Phys.* **52**, 04CF10 (2013).
- [142] S. Boi, W. Wu, Y. Qin, N. Cui, D. J. Bayerl and X. Wang, *Adv. Funct. Mater.* **21**, 4464-4469 (2011).
- [143] Y. Liu, H. Zhou, R. Cheng, W. Yu, Y. Huang, and X. Duan, *Nano Lett.* **14**, 1413-1418 (2014).
- [144] I. Park, C. Jeong, I. Cho, J. Lee, E. Cho, S. Kwon, B. Kim, W. Cheong, S. Song and H. Kwon, *Semicond. Sci. Technol.* **27**, 105019 (2012).
- [145] D. J. Thouless, *Phys. Rev. Lett.* **39**, 1176 (1977).
- [146] A. Lu, M. Dai, J. Sun, J. Jiang, and Q. Wan, *IEEE Electron Device Lett.* **32**, 518 (2011).
- [147] A. Suresh, P. Wellenius, A. Dhawan, and J. Mutha, *Appl. Phys. Lett.* **90**, 123512 (2007).

- [148] T. T. Trinh, V. D. Nguyen, K. Ryu, K. Jang, W. Lee, S. Baek, J. Raja and J. Yi, *Semicond. Sci. Technol.* **26**, 085012 (2011).
- [149] H. Bong, W. H. Lee, D. Y. Lee, B. J. Kim, J. H. Cho and K. Cho, *Appl. Phys. Lett.* **96**, 192115 (2010).
- [150] N. C. Su, S. J. Wang, and A. Chin, *IEEE Electron Device Lett.* **30**, 1317 (2009).
- [151] C. Chien, C. Wu, Y. Tsai, Y. Kung, C. Lin, P. Hsu, H. Hsieh, C. Wu, Y. Yeh, C. Leu, and T. Lee, *IEEE Trans. Electron* **58**, 1440 (2011).
- [152] A. Bikowski and K. Ellmer, *J. Appl. Phys.* **116**, 143704 (2014).
- [153] R. S. Bisht, R. R. Ghimire and A. K. Raychaudhuri, *J. Phys. Chem. C* **119** (49), 27813-27820 (2015).
- [154] S. Baruah, S. S. Sinha, B. Ghosh, S. K. Pal, A. K. Raychaudhuri, and J. Dutta, *J. Appl. Phys.* **105**, 074308 (2009).
- [155] M. K. Kavitha, K. B. Jinesh, R. Philip, P. Gopinath and H. John, *Phys. Chem. Chem. Phys.* **16**, 25093-25100 (2014).
- [156] F. Frederix, J. Friedt, K. Choi, W. Laureyn, A. Campitelli, D. Mondelaers, G. Maes and G. Borghs, *Anal. Chem.* **75**, 6894-6900 (2003).
- [157] K. Liu, M. Sakurai, M. Liao and A. Masakazu, *J. Phys. Chem. C* **114**, 19835-19839 (2010).
- [158] N. Gogurala, A. K. Sinha, S. Santra, S. Manna, S. K. Ray, *Sci. Rep.* **4**, 6483 (2014).
- [159] M. Gwon, A. Sohn¹, Y. Cho¹, S. Phark, J. Ko, Y. Kim, D. Kim, *Sci. Rep.* **5**, 16727(2015).
- [160] Z. Chen, Y. Tang, C. Liu, Y. Leung, G. Yuan, L. Chen, Y. Wang, I. Bello, J. Zapien, W. Zhang, C. Lee, S. Lee, *J. Phys. Chem. C* **113**, 13433-13437 (2009).
- [161] C. Cheng, E. Sie, B. Liu, C. Huan, T. Sum, H. Sun, H. Fan, *Appl. Phys. Lett.* **96**, 071107 (2010).

- [162] T. Chen, G.Z. Xing, H. Y. Chen, T. Wu, *Nanotechnology* **19**, 435711 (2008).
- [163] S. J. Chang, T. J. Hsueh, I. Chen, B. Huang, *Nanotechnology* **19**, 175502 (2008).
- [164] Y. Zhang, J. Xu, P. Xu, Y. Zhu, X. Chen, W. Yu, *Nanotechnology* **21**, 285501 (2010).
- [165] H. Qi, D. Alexson, O. Glembocki, S. M. Prokes, *Nanotechnology* **21**, 215706 (2010).
- [166] A. Bera, D. Basak, *Nanotechnology* **22**, 265501 (2011).
- [167] J. D. Hwang, F. H. Wang, C. Y. Kung, M. J. Lai and M. C. Chan, *J. Appl. Phys.* **115**, 173110 (2014).
- [168] S. Bai and S. Wu, *J. Mater. Sci. Mater. Electron.* **22**, 339-344 (2011).
- [169] S. Hullavarad, N. Hullavarad, D. Look and B. Claffin, *Nanoscale Res. Lett.* **4**, 1421-1427 (2009).
- [170] J. Bao, I. Shalish, Z. Su1, R. Gurwitz, F. Capasso, X. Wang and Z. Ren, *Nanoscale Res. Lett.* **6**, 404 (2011).
- [171] D. Cammi and C. Ronning, *Adv. Condens. Matter Phys.* **2014**, 184120 (2014).
- [172] K. Das, S. Mukherjee, S. Manna, S. K. Ray, A. K. Raychaudhuri, *Nanoscale* **6**, 11232-11239 (2014).
- [173] H. A. Atwater, A. Polman, *Nat. Mater.* **9**, 205 (2010).
- [174] A. Kolmakov, D. O. Klenov, Y. Lilach, S. Stemmer, M. Moskovits, *Nano Lett.* **5**, 4 (2005).
- [175] K. Wu, J. Chen, J. R. McBride, T. Lian, *science* **349**, 632 (2015).
- [176] B. Balamurugan and T. Maruyama, *Appl. Phys. Lett.* **87**, 143105 (2005).
- [177] Y. Gao, Z. Yuan, and S. Gao, *J. Chem. Phys.* **134**, 134702 (2011).
- [178] R. Gurwitz, R. Cohen, and I. Shalish, *J. Appl. Phys.* **115**, 033701 (2014).